
Unterschrift BetreuerIn



TECHNISCHE
UNIVERSITÄT
WIEN
Vienna University of Technology

DIPLOMARBEIT

Monte Carlo based Dose Calculation for an X-Irradiator in pre-clinical Research

Ausgeführt am

Atominstitut

der Technischen Universität Wien

unter der Anleitung von

Univ.-Prof. DI Dr. Dietmar Georg

Mag. Peter Kuess, PhD

DI Hermann Fuchs, PhD

durch

Lukas Gnam, BSc

Nr. 206

2822 Walpersbach

10. Dezember 2015

Unterschrift StudentIn

Contents

1	Motivation and Objectives	3
2	Introduction	5
2.1	Basic Physics	5
2.1.1	Interactions of Photons with Matter	5
2.1.2	Radiation Attenuation	12
2.2	X-Rays	13
2.2.1	Production	13
2.2.2	Spectrum	16
2.2.3	Filtering	18
2.2.4	Beam Quality	21
2.3	Ionization Chambers	22
2.3.1	Principle of Operation	22
2.4	Monte Carlo Method	23
3	Materials	27
3.1	X-Ray Tube - YXLON Maxishot	27
3.2	Scintillator based Sensor - LYNX	28
3.3	Water Phantom - Perspex Tank	29
3.4	Ionization Chamber	30
3.5	NOMEX Multimeter	31
3.6	X-Ray Spectra Software SpekCalc	32
3.7	Monte Carlo Toolkit GATE	33
3.8	Data Analysis Framework ROOT	35

4	Methods	37
4.1	Experiments on Beam Characteristics	37
4.1.1	Measurements with Ionization Chamber and Perspex Tank .	37
4.1.2	Half Value Layers in PMMA	39
4.1.3	Nomex Measurements	40
4.1.4	LYNX Measurements	40
4.2	Simulations	40
4.2.1	Parameters for SpekCalc	40
4.2.2	GATE Simulations	41
5	Beam Characteristics	51
5.1	Half Value Layers	51
5.1.1	Measurements with Ionization Chamber and Perspex Tank .	51
5.1.2	Nomex Measurements	51
5.2	Beam Profiles	52
5.2.1	Measurements with Ionization Chamber and Perspex Tank .	52
5.2.2	LYNX Measurements	56
5.3	Half Value Layers in PMMA	58
6	Simulations	59
6.1	SpekCalc	59
6.2	Half Value Layers in mm Al	64
6.2.1	Al-Filter	64
6.2.2	Al-Cu-Filter	64
6.2.3	Single Al-Filter	66
6.2.4	Filtration in SpekCalc	66
6.3	Beam Profile	67
6.3.1	Al-Filter	67
6.3.2	Al- and Cu-Filter	69
6.3.3	Single Al-Filter	70
6.3.4	Filtration in SpekCalc	71
6.4	Half Value Layers in PMMA	72
6.5	Lead Collimator Setup	74

6.6	Cell Irradiation Setup	76
7	Analysis and Discussion	83
7.1	Half Value Layers	83
7.1.1	Half Value Layers in Aluminium	83
7.1.2	Intensity Variation in Air	91
7.1.3	Half Value Layers in PMMA	97
7.2	Cross- and Inplane Profiles	101
7.3	Spot Size in Lead Collimator Setup	113
7.4	Dose Distributions in Cell Irradiation Setup	113
8	Conclusion and Outlook	117
	Bibliography	121

Acknowledgements

First of all I would like to thank my supervisor Prof. Dr. Dietmar Georg for giving me the chance to work on my Master thesis in the Department of Radiotherapy at the Medical University of Vienna and providing me with the opportunity to conduct my studies at MedAustron in Wiener Neustadt. He helped me through all the organizational work and supported me with useful advices whenever possible.

I owe my deepest gratitude to my co-supervisors Mag. Peter Kuess, PhD, and DI Hermann Fuchs, PhD. Their support throughout all phases of this thesis reached from introducing me to the laboratory and computer equipment to providing me always with highly useful comments and interesting discussions on every matter, that were essential for the improvement and progress of my work.

In addition, I wish to thank DI Dr. Albert Hirtl from the Radiation Physics Department at the Technical University of Vienna, who gave me always handy comments on all my troubles I came across using the GATE and ROOT framework and was also responsibly for many thought-provoking lunch debates, covering a lot of different topics besides our work.

I would also like to thank my officemate at MedAustron, Merim Cato, BSc., for welcoming me as a colleague and friend and for all the cheering up during our coffee breaks in the office when times were stressful.

Without the support and dedication of my parents, who made it possible for me to study in the first place, I would not have been able to focus all my energy and effort on my course of studies.

Finally, I cannot find words to express my gratitude to my beloved girlfriend Tini for all her love, support and encouragement. Thank you for always making me laugh and calming me down whenever I was frustrated. Without you I would not have come this far!

1 Motivation and Objectives

Pre-clinical research based on animal models and cell cultures allows to study normal tissue and tumour behavior. This is an important research field for the development of new therapeutic concepts and a more in depth understanding of radiation effects on tissues. Pre-clinical research is also a highly relevant research field in ion beam therapy to overcome the current uncertainties with respect to the radiobiological knowledge. State of the art is to perform cell culture and animal studies with X-ray units. However, the complexity of the X-ray unit varies in great extend making accurate dose calculations challenging. At the Medical University of Vienna an X-ray unit with variable energy up to 200 kV is used for irradiation of small animals and cell experiments. An identical device was recently installed at MedAustron for radiobiological experiments. Dose deposition can be controlled by individually designed lead collimators. Thus every experimental setup requires detailed individual dosimetric measurements and verification. To characterize the beam properties the half-value layers (HVL) are determined. Hence, the unpractical (and expensive) direct measurement of the X-ray spectra using spectrometers can be bypassed.

Since all these measurements are very time consuming, computational methods for dose calculation, like Monte Carlo simulations, gain more and more popularity. This development goes hand in hand with the increase in computing power. One popular framework for medical applications is the simulation environment GATE (Geant4 Application for Tomographic Emissions). It evolved from a small specialized application used to simulate imaging systems, like PET and SPECT, to a more and more applicable tool for a wide variety of medical systems, including radiotherapy devices [1].

The aim of this master project was to model the X-ray unit YXLON Maxishot with the Monte Carlo toolkit GATE and to verify the simulation outcomes with dosimetric measurements.

2 Introduction

2.1 Basic Physics

This section provides an introduction to X-ray physics and dosimetry. All theoretical descriptions are based on the book series by Hanno Krieger [2–4].

2.1.1 Interactions of Photons with Matter

The photon energies typically applied in medical applications range from some keV in mammography up to 25 MeV in radiation therapy. While interacting with matter, photons can be scattered and it is possible that their energy is absorbed, either partially or totally. Interactions with matter usually produce electrons or other secondary particles which can excite or ionize surrounding matter. Therefore, photon radiation is considered as indirect ionizing radiation.

Photons can interact either with the atomic shell or the nucleus itself. Coherent scattering, photoelectric effect and incoherent scattering are interactions between shell and photons. Pair production and photonuclear effects occur between nucleus and photons.

The interaction probability of photons is very low compared to charged particles. Therefore photon beams have a deep penetration range and can be used for diagnostic purposes as well as for the therapy of tumours inside the body [2, 4].

2.1.1.1 Coherent Scattering

Coherent scattering describes the interaction of an incident photon with the electronic shell of the atom. The absorbed photon energy induces a collective electron oscillation, with the oscillation frequency being the same as the photon frequency. During this oscillation the absorbed energy is emitted via a photon. Thus, the

absorbed and the emitted photon have the same frequency and no energy transfer to the atom or ionization occurs. The process is visualized in figure 2.1.

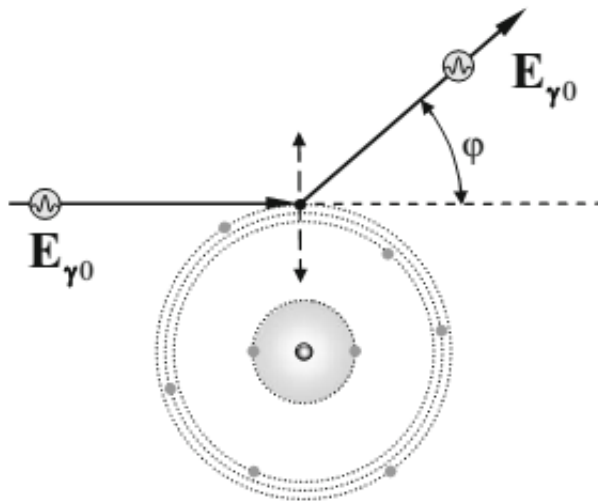


Figure 2.1: Coherent scattering on bounded electron (from [2], p185).

For the cross section σ_{kl} above 10 the following approximation holds

$$\sigma_{kl} \propto \rho \frac{Z^{2.5}}{A \cdot E_\gamma^2} \approx \rho \frac{Z^{1.5}}{E_\gamma^2}, \quad (2.1)$$

where ρ denotes the density, Z the atomic number, A the mass number and E_γ the photon energy. Therefore coherent scattering is only important at low energies below approximately 20 keV and for materials with low atomic number Z , like human tissue or water.

2.1.1.2 Photoelectric Effect

If a photon hits an electron and is fully absorbed, it is possible that this electron gains enough energy to leave the atomic shell (see figure 2.2). The difference between photon energy E_γ and electron binding energy E_b is converted into the electron's kinetic energy E_{kin} .

$$E_{kin} = E_\gamma - E_b \quad (2.2)$$

This leads to the fact, that the photon energy must be greater than the binding energy of the electron.

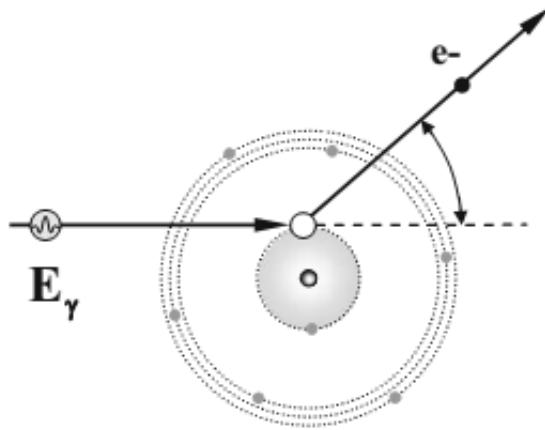


Figure 2.2: Photoelectric effect (from [2], p160).

The probability for the photoelectric effect is specified by the so called photoabsorption coefficient τ . It strongly depends on the density ρ and the atomic number Z . For heavy elements τ reaches its maximum values of about

$$\tau \propto \rho Z^3. \quad (2.3)$$

τ decreases with increasing photon energies above the K-shell-energy.

$$\tau \propto \frac{1}{E_\gamma^3} \quad (2.4)$$

If photon energy and electron binding energy are exactly the same, the interaction probability reaches a maximum. This absorption edges can be seen in figure 2.3.

The released electrons have an energy-dependent angular distribution relative to the incident angle of the photons. With increasing photon energy, more and more secondary electrons are emitted in forward direction, in contrast to the almost perpendicular or even backward directed emission at low energies [2].

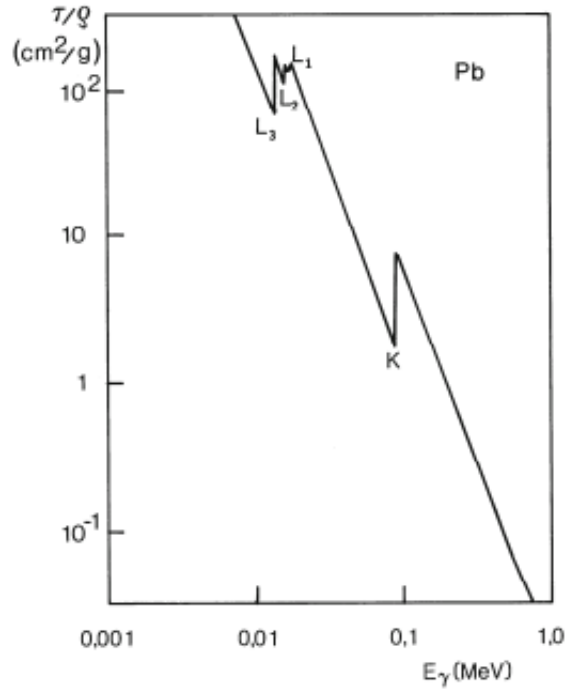


Figure 2.3: Energy dependance of the mass-photoabsorption coefficient τ/ρ for lead with the absorption edges L_1 - L_3 and K (from [2], p162).

2.1.1.3 Compton Effect

The Compton effect describes the incoherent scattering of a photon with a weakly-bound electron from an outer shell. Some of the photon's energy and momentum are transferred to the electron during this process and the path of the photon is scattered at an angle φ . Hence, the electron is able to leave the atomic shell at an angle θ (see figure 2.4).

Using the Compton attenuation coefficient, it is possible to describe the probability of occurrence for this effect. It is split up into two parts, σ_{sc} for the incoherent photon scattering and σ_{tr} for the energy and momentum transfer from the photon to the electron:

$$\sigma_c = \sigma_{sc} + \sigma_{tr}. \quad (2.5)$$

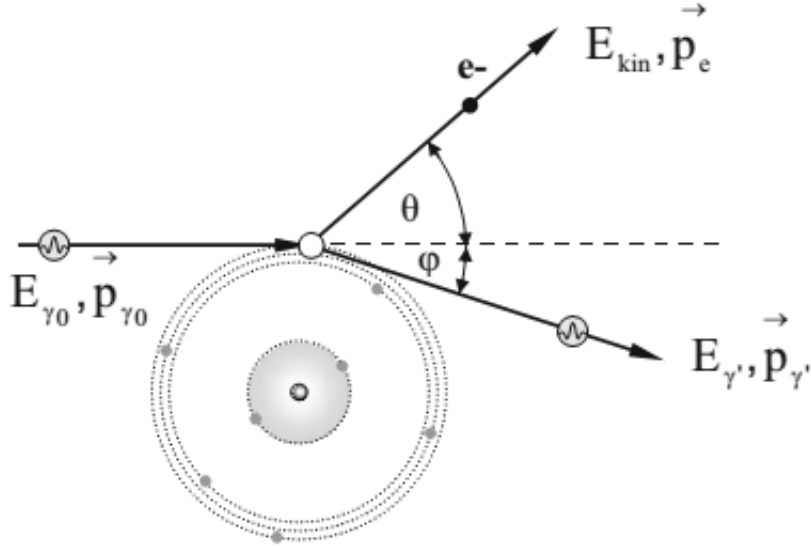


Figure 2.4: Compton effect (from [2], p165).

The Compton effect is almost independent of the atomic number Z , since

$$\frac{Z}{A} \approx \frac{1}{2}, \quad (2.6)$$

and with the effect being nearly proportional to the ratio $\frac{Z}{A}$. An explanation can be found by looking at the atomic shell. The outer electrons see only a shielded nucleus and are therefore found to be weaker bounded than the inner ones, leading to the fact that the atomic number has little impact on their behaviour. σ_c is, like in all other photon interactions, proportional to the density ρ of the absorber material.

A big challenge when using the Compton attenuation coefficient lies in its complicated mathematical description. Hence, it is common practice to work with tables or diagrams summarizing the respective values. For the energy range between 0.2 and 10 MeV an approximation for σ_c can be used:

$$\sigma_c \propto \rho \frac{Z}{A} \frac{1}{E_\gamma^n}, \quad (2.7)$$

where E_γ is the photon energy and the exponent n ranges from 0.5 to 1.

If the scattering is seen as an elastic collision between the photon and the electron, where latter is assumed to be stationary before the collision, energy and momentum conservation yield for the energy E'_γ of the scattered photon

$$E'_\gamma = \frac{E_\gamma}{1 + \frac{E_\gamma}{m_0c^2}(1 - \cos(\varphi))}, \quad (2.8)$$

where E_γ denotes the energy before the interaction, m_0c^2 the rest energy of the electron and φ the scatter angle of the photon. The energy is therefore divided up between the electron and the photon. Angular and energy distribution for both, photons and electrons, are depending on the energy of the incident photon. Unfortunately equation 2.8 is useless for calculating the frequency of occurrence for certain scattering angles. Relativistic quantum theory is needed for a derivation. However, this equation can be used to estimate the energy loss of the photon. If the rest energy m_0c^2 of the electron is much greater than the photon energy E_γ , the photon loses almost no energy and only little energy is transferred to the electron, leading to no dose accumulation. This is particularly important for diagnostic X-rays, where low energies are used. In contrast to that, high energy photons ($E_\gamma \gg 511$ keV) have an energy-dependent denominator greater than 1, yielding both, more energy being transferred to the electron and a dependency on the scattering angle. Additionally, this causes dose accumulation occurring on material borders [2].

2.1.1.4 Pair Production

If a photon with an energy above 1022 keV interacts with a strong Coulomb field, its energy can be used for the spontaneous production of an electron-positron-pair. The photon energy is then transformed into the rest masses of both particles (511 keV each), with the remaining energy being divided up arbitrarily as kinetic energy. The total kinetic energy available is

$$E_{kin} = E_\gamma - 2 \cdot m_0c^2 = E_\gamma - 2 \cdot 511 \text{ keV}. \quad (2.9)$$

After their production, the electron and positron travel through the absorber material and continuously lose energy due to multiple scattering. When the positron has lost its kinetic energy, it recombines with an electron, producing two photons 511 keV which are emitted in opposed direction. The left part in figure 2.5 shows this process. These two photons only slightly contribute to absorbed dose. At high energies pair production becomes the most dominant effect in photon-matter-interactions.

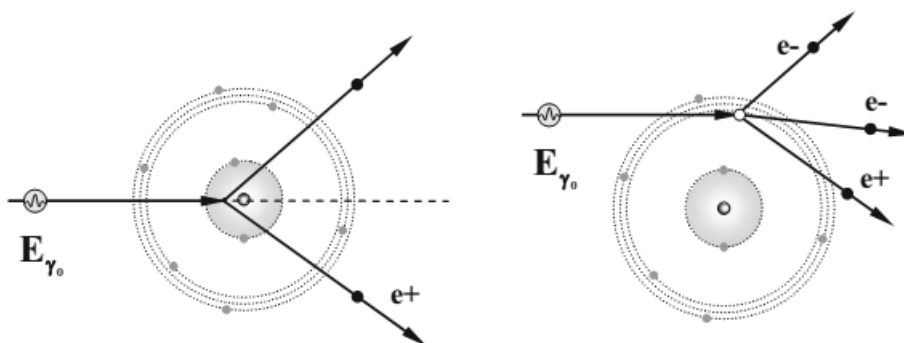


Figure 2.5: Left: Pair production in atomic Coulomb field. Right: Triplet production in electronic Coulomb field (from [2], p182).

Rather rare is the case, where pair production takes place in the Coulomb field of a shell electron. Due to its lighter mass, the absorbed energy can lead to emission of the electron from the atomic shell. It then propagates with the electron-positron-pair through the material and again multiple scattering events take place. Because of the three participating particles, the effect shown in the right part of figure 2.5 is called triplet production. Triplet production needs at least photon energies greater than $4 \cdot 511$ keV, due to energy and momentum conservation [2].

2.1.1.5 Photonuclear Interactions

The electromagnetic field of the nucleus can also interact with a photon by absorbing it. This leaves the nucleus in an excited state. If the absorbed energy is above a certain threshold (6 to 20 MeV, depending on the nucleus) neutrons or protons can be emitted (see figure 2.6). The cross section σ_{pn} for light atoms has its maximum at 20 – 25 MeV, for medium-weight ones it is about 10 – 15 MeV. At high

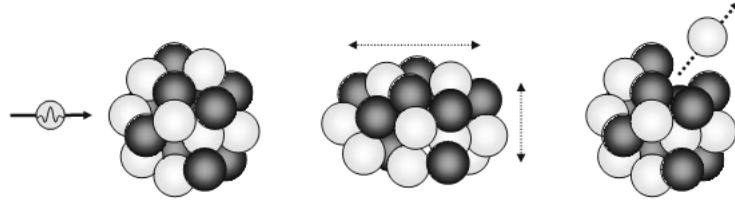


Figure 2.6: Photonuclear interaction: A photon excites the nucleus resulting in emission of a nucleon (from [2], p186).

photon energies σ_{pn} decreases rapidly. Mostly (γ, n) -, $(\gamma, 2n)$ - and (γ, p) -reactions take place, but due to the little cross section this effect is negligible. However, photonuclear reactions can lead to activation of absorbing material or air, which is of critical importance in radiation protection [2].

2.1.2 Radiation Attenuation

Photon interactions in matter cause a decrease in intensity, where dI denotes this change. With x being the thickness, it is given by

$$dI = -I\mu dx. \quad (2.10)$$

μ denotes the linear attenuation coefficient, describing the weakening of a photon beam propagating through matter. Integration of equation 2.10 yields

$$I = I_0 e^{-\mu x}, \quad (2.11)$$

with I_0 as the initial value of the intensity. Equation 2.11 is known as Beer-Lambert law, which describes the exponential decrease of a photon beam.

Since different effects contribute to the attenuation, μ is composed from

$$\mu = \tau + \mu_{\text{Compton}} + \mu_{\text{coherent}} + \kappa_{\text{pair}} + \kappa_{\text{triplet}} + \sigma_{\text{photonuclear}}. \quad (2.12)$$

Here τ is the coefficient of the photoelectric effect, μ_{Compton} the Compton effect and μ_{coherent} coherent scattering. κ_{pair} and κ_{triplet} describe the contributions from the pair production effect. Photonuclear interactions, with the coefficient $\sigma_{\text{photonuclear}}$,

are often negligible. As μ is strongly dependent on the specific properties of a material, in particular the density ρ , the quantity $\frac{\mu}{\rho}$, known as mass attenuation coefficient, is often used instead [4, 5].

2.2 X-Rays

In 1895 W.C. Röntgen discovered during experiments with gas discharge lamps, that radiation emitted from this lamps is able to penetrate materials like glass, wood or human tissue. As he did not know anything more about this photon radiation, he called it X-radiation. He was awarded the Nobel Prize in 1901 as the first physicist ever. Since his discovery, X-rays have been under detailed investigation and the object of various experiments. Many modern technologies rely on their properties, like computed tomography, diagnostic imaging, material sciences, sterilizing of food or even radio astronomy [6].

2.2.1 Production

In principle, an X-ray tube consists of a cathode and an anode in high vacuum. Electrons emitted from the cathode are accelerated by an applied high voltage. In the anode they lose energy due to interactions with the target atoms and X-rays are produced. The principle setup is pictured in figure 2.7.

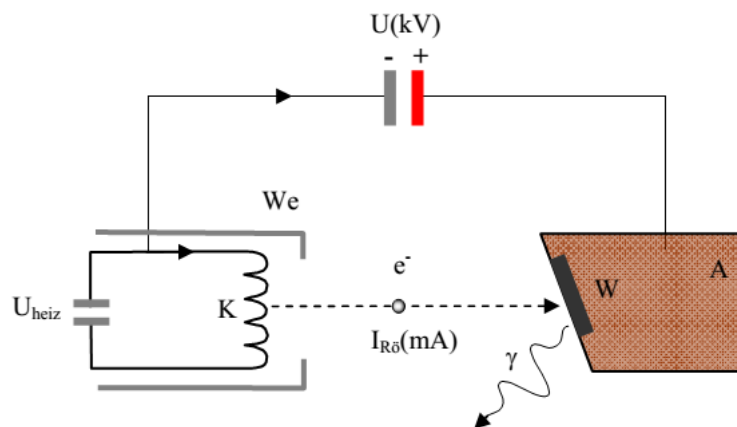


Figure 2.7: X-ray tube: electrons are emitted from the cathode K and interact in the anode A (from [4], p89).

Two different types of X-rays exist: bremsstrahlung and characteristic radiation. Both are produced when hitting an anode, leading to the fact that a continuous X-ray spectrum always contains characteristic peaks. Form of the spectrum and X-ray yield strongly depend on the used material.

The energy of the X-rays is given in electron volts, with

$$1 \text{ eV} = 1.6022 \cdot 10^{-19} \text{ J.} \quad (2.13)$$

Photon energy E_{ph} , photon frequency ν and wave length λ are connected via

$$E_{ph} = h \cdot \nu = h \frac{c}{\lambda}, \quad (2.14)$$

where c is the speed of light in vacuum and h Planck's constant with

$$h = 6.626 \cdot 10^{-34} \text{ J} \cdot \text{s} \approx 4.136 \cdot 10^{-15} \text{ eV} \cdot \text{s}. \quad (2.15)$$

2.2.1.1 Production of Characteristic X-Rays and Auger Electrons

Charged particles propagating through matter interact with the atomic electrons and lose energy. Responsible for the energy loss are the processes of excitation or ionization. The latter can also be the result of interactions such as the photoelectric effect and incoherent scattering. Excitation happens when energy is transferred to a shell electron displacing it further away from the nucleus and creating a hole in the original shell. If the transferred energy is above a specific threshold the electron can gain enough energy to escape the shell, leaving the atom in an ionized state [5].

Every vacancy created in an inner shell is always filled by an electron from an outer shell, which again results in a hole and the filling process in that outer shell starts again. The released energy from the outer electron can be emitted as a photon or by an electron ejected from an outer shell, which is then called Auger electron [5].

Since the binding energies of the electrons differ from shell to shell, and the released energy is the difference of the electron binding energies, this type of radiation is characteristic for each atom. The most important anode materials are

tungsten, rhenium, molybdenum and rhodium [4].

The characteristic X-ray photons are denoted after the shell containing the hole. If the electron fills up a hole in the K shell, the emitted radiation is called K characteristic X-ray, transitions to the L shell yield L characteristic radiation and so on. Numerical indices are used to determine the subshells involved in the process and greek subscripts indicate the origin of the electron. The subscript α stands for an electron from a neighbouring shell, β for a non-neighbouring one. For tungsten, as example, the K_α energy is given by

$$\begin{aligned}
 E(K_{\alpha 1}) &= E_{L1} - E_K = -10.2 - (-69.5) = 59.3 \text{ keV}, \\
 E(K_{\alpha 2}) &= E_{L1} - E_K = -11.5 - (-69.5) = 58.0 \text{ keV}, \\
 E(K_{\beta 1}) &= E_{M3} - E_K = -2.3 - (-69.5) = 67.2 \text{ keV}, \\
 E(K_{\beta 2}) &= E_{N3} - E_K = -0.4 - (-69.5) = 69.1 \text{ keV}.
 \end{aligned}
 \tag{2.16}$$

When looking at Auger electrons carrying away the released energy, we have to take into account that two vacancies are created. Thus, for example, the kinetic energy of the Auger electron emitted from the M shell in tungsten, with the initial transition being from the M to the K shell, is given by

$$E_{kin} = E_K - E_M - E_M = -[(-69.5) - (-2.3) - (2.3)] = 64.9 \text{ keV}. \tag{2.17}$$

The emission of X-rays and the Auger effect are competing processes. The amount of transitions yielding X-radiation is called fluorescence yield. It strongly depends on the atomic number Z . With $Z < 30$, Auger effect is dominating, whereas for $Z > 60$ the fluorescence yield is about 90 % [5, 6].

2.2.1.2 Production of Bremsstrahlung

If the interactions between the accelerated electrons from the cathode occur in the Coulomb field of atoms in the anode material, bremsstrahlung is produced. This happens when the path of the incident electron is deflected and results in emission of a photon. The path of the electron depends on its initial energy, the distance from the nucleus and the charge of the nucleus. The closer the electron gets to the nucleus, the higher the emitted photon energy gets. Both, Compton and

photoelectric effect can account for this process. Since the various dependencies, the photons can take up any energy value ranging from zero up to the energy of the incident electron.

The atomic number Z determines the probability of bremsstrahlung emission. Thus, it is higher for materials with higher Z , like tungsten ($Z = 74$). However, even for tungsten the production yield is less than 1% for energies under 100 keV [5].

2.2.2 Spectrum

As a first step in deriving the form of a typical X-ray spectrum, the interactions and results of photons in a thin target are investigated. The electrons hitting this thin target are assumed to be scattered only once, at randomly distributed distances b from the nucleus. Hence, the energies E_γ of the produced photons can reach from 0 to the upper limit E_g , where E_g represents the kinetic energy of the incident electrons. E_g also defines the maximum energy in the X-ray spectrum.

For describing photon spectra, intensity I or specific intensity I^* are used. The quantities I and I^* are defined as the radiation energy transported per unit area and unit time, and the energy in a small interval dE transferred per unit area and unit time, respectively.

Since the nucleus is rather small compared to the shell of an atom, only a small amount of electrons will come close to the nucleus and produce high energy photons. With increasing impact parameter b , which describes the distance between electron and nucleus, the number N_γ of photons produced is increasing proportionally to b . Simultaneously, the energy of the produced photons E_γ is decreasing. Assuming the relation

$$E_\gamma \propto \frac{1}{b}, \quad (2.18)$$

the product of E_γ and N_γ is nearly constant.

$$E_\gamma \cdot N_\gamma \approx \text{const.} \quad (2.19)$$

Equation 2.19 yields a rectangular spectrum as shown in figure 2.8.

The distribution of the specific intensity I^* is constant for a given electron energy

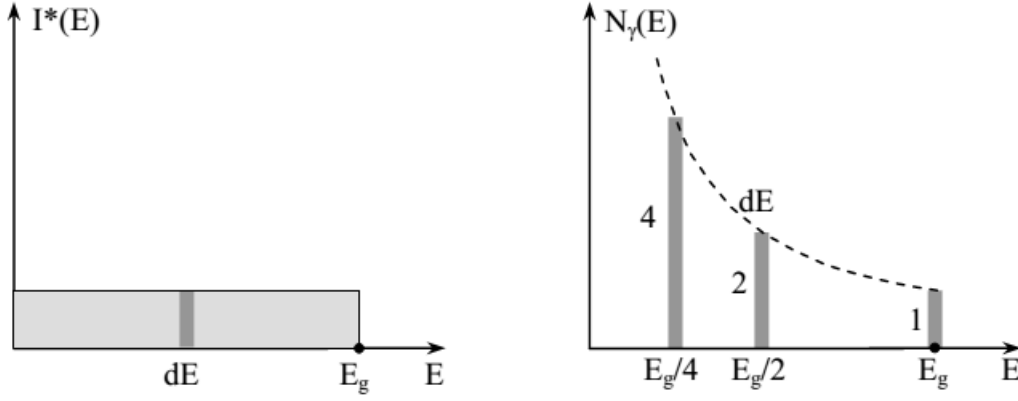


Figure 2.8: Left: Rectangular distribution from electrons with kinetic energy E_g . Right: Characteristic of N_γ (from [4], p94).

E_g , with the rectangular area corresponding to the intensity I . On the contrary, the number of photons decreases exponentially with increasing energy.

If the target anode is thicker than the electron range, it is necessary to assume the target being divided into slices with thickness dx . Each slice produces a rectangular spectrum as described above. Due to the energy loss in every slice, the entrance energy of the electrons decreases from slice to slice. For non-relativistic particles we can assume that the total stopping power S_{tot} is inversely proportional to the electron energy E_g

$$S_{\text{tot}} = \frac{1}{E_g}, \quad (2.20)$$

yielding an increased energy loss per slice as well as an increased specific intensity. However, if the thickness dx is assumed in a way that the energy loss is constant in every slice, the intensity spectra differ only in their limiting energy and not anymore in the height of their specific intensity. Summation of all spectra gained from the thin slices yields the total triangular spectrum (see figure 2.9).

For the total intensity the following relation holds

$$I(E_g) = \int_0^{E_g} I^*(E_\gamma) \cdot dE_\gamma = \int_0^{E_g} b \cdot (E_g - E_\gamma) dE_\gamma \propto E_g^2. \quad (2.21)$$

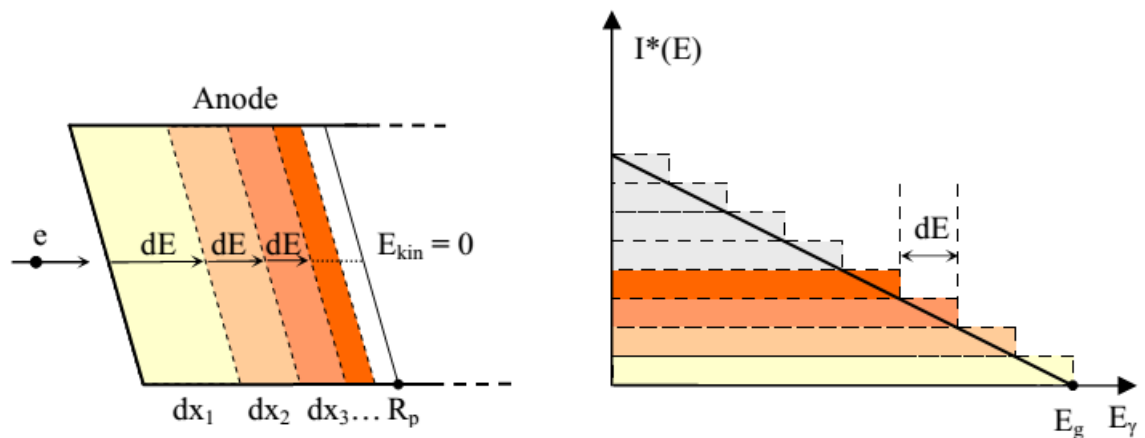


Figure 2.9: Left: Concept of varying slice thickness. Right: Typical triangular spectrum (from [4], p96).

That is the reason why the intensity changes quadratically with the electron energy, which is controlled via the applied tube current.

For medium sized targets the spectrum is a mixture of the thin and the thick target approximation.

2.2.3 Filtering

The output spectrum from an anode consists of the continuous triangular spectrum and its specific characteristic lines, which is shown in figure 2.10.

Depending on the medical field of use, different parts of the spectrum need to be filtered to gain specific beam properties. In mammography, for example, different characteristics are needed, in contrast to a thorax X-ray image. Since low energy photons have a low penetration depth, they only contribute to absorbed dose and therefore need to be removed from a spectrum. The first filtration effects occur in the anode itself. Together with the filtration from the exit window, in most cases consisting of beryllium, this is called inherent filtration.

The before mentioned self-filtration inside the anode is called Heel effect (see figure 2.11). Here, the photons produced inside the anode lose energy while propagating through the anode material. For photons being produced near the anode side, the loss is higher than for the ones coming from the cathode side, resulting

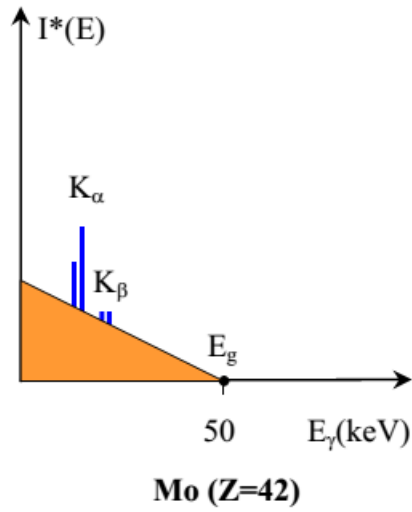


Figure 2.10: Left: Unfiltered molybdenum spectrum (from [4], p105).

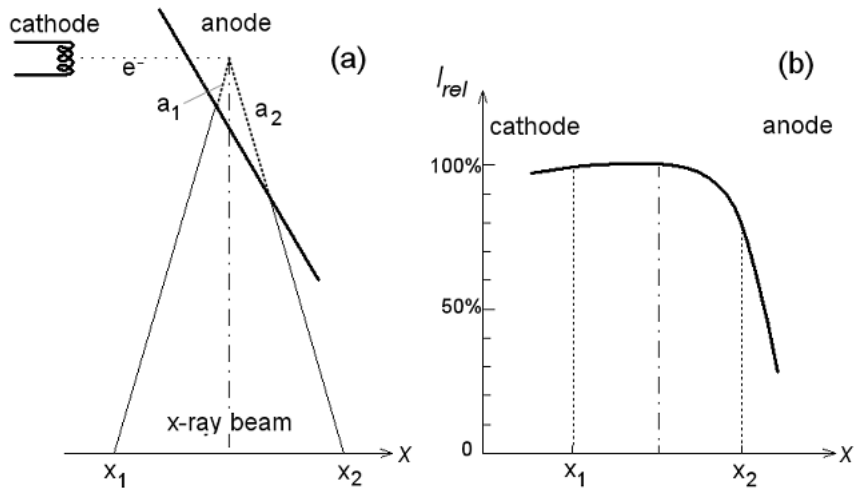


Figure 2.11: a) Photons from the anode side (a2) undergo more interactions inside the anode than the ones from the cathode side (a1). b) Intensity drop on the anode side resulting from the increased absorption. This is called Heel effect (from [5], p97).

in an inhomogeneous intensity of the X-ray beam.

Increasing μ at low energies leads to beam hardening, which is just a decrease in the number of low energy photons. Using filtration, in addition to the self filtration of the anode, an X-ray beam can be modified for specific purposes. Mostly

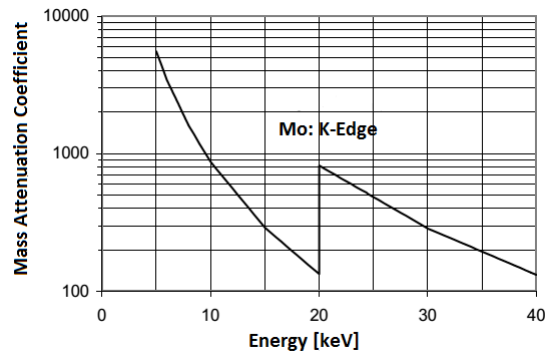


Figure 2.12: Linear mass attenuation coefficient for molybdenum (from [4], p107).

molybdenum, rhenium, rhodium, aluminium, palladium and copper are used. In these materials the photoelectric effect dominates in the energy range used for typical X-ray applications. Additionally, at the K- and L-binding energies these materials, except Al, show a steep increase in their mass attenuation curve (see figure 2.12), yielding a high increase in absorption and thus, producing cuts in the spectrum (see figure 2.13).

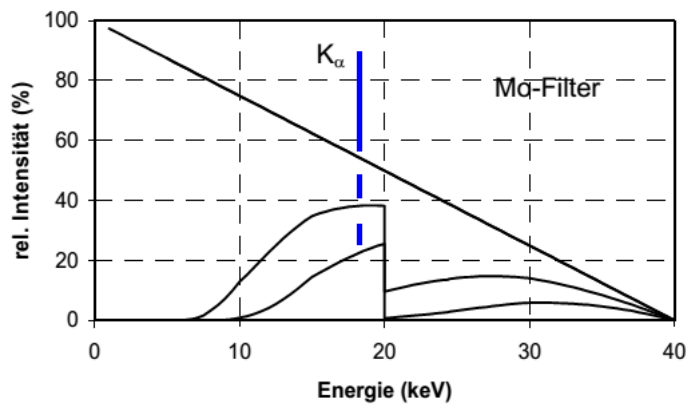


Figure 2.13: Cut off resulting from the K-edge of molybdenum (from [4], p107).

These cuts do not occur when using Al as filter material, since the K-binding energy is about 1.56 keV and the L-binding energy about 0.07–0.1 keV. Al-filtered spectra therefore show only a decrease in the low energy region, due to its mass attenuation coefficient (see figure 2.14).

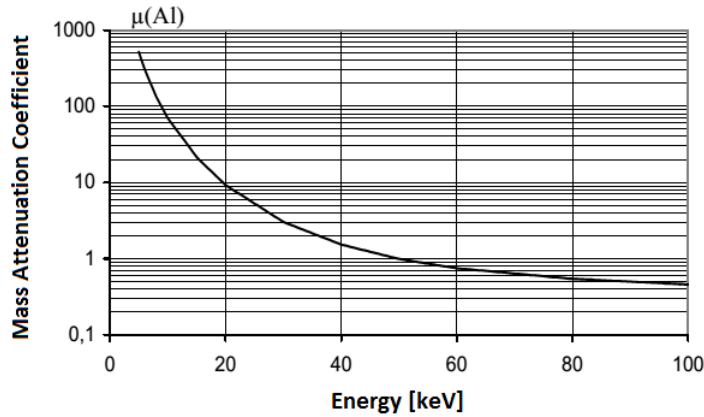


Figure 2.14: Mass attenuation coefficient of Al (from [4], p109).

2.2.4 Beam Quality

Specifying the quality of an X-ray beam is a rather difficult task. Various parameters can be taken into account, for example the half value layer (HVL), the intensity or the whole photon spectrum. Since measuring the latter is very time-consuming and requires expensive equipment, it is rarely used. Very practical for describing beam quality in low to medium energy X-ray beams is the HVL. The HVL describes the thickness of the absorbing material, leading to an intensity decrease of 50 %:

$$d_{\frac{1}{2}} = \frac{\ln(2)}{\mu} = \text{HVL}. \quad (2.22)$$

The distance d where the intensity drops to 50 % is called first HVL (1. HVL), the one where it drops to 25 % second HVL (2. HVL). Using the ratio of the first and second HVL, the so called homogeneity factor (HF) can be defined as in [7]:

$$HF = \frac{1.\text{HVL}}{2.\text{HVL}}. \quad (2.23)$$

Tube voltage (kV) has a strong influence on the HVL, as a change in energy yields a different spectrum. The higher the energy, the more high energy photons are produced, increasing the HVL. Maximum and mean photon energy depend on the kV, whereas it has no influence on the photon distribution. However, tube current (in mAs) is only responsible for changes in photon intensities.

2.3 Ionization Chambers

Ionization chambers are most commonly used in radiation measurement and clinical dosimetry. Here air or other gaseous media are being ionized by incident radiation, producing electrons and positively charged ions. Air is mostly used as filling gas, since it is freely available and has similar dosimetric properties compared to human tissue. For particular tasks, as for example measuring of environmental radiation, inert gases, as xenon, may be used instead.

A major problem arising with ionization chambers is the complete collection of the produced charges under all possible circumstances. It has to be assured, that all charges produced in a detector are measured or that at least an accurate correction for occurring losses is provided. This leads to the fact that ionization chambers need specific designs and have to be chosen adequately, depending on the properties of the radiation field.

In order to determine the absorbed dose, the mean energy for the production of an ion pair in the detector material has to be known. Precise measurements of this quantity is subject of multiple international projects.

Once the absorbed dose is known, the next step is to get the absorbed dose in the phantom volume. Here new potential uncertainties have to be taken into account, for example differences in the detector and the phantom material [3].

2.3.1 Principle of Operation

An electrically charged plate capacitor connected to a direct current is the simplest type of ionization chamber. In between is a gas, where electron-ion-pairs are produced by ionizing radiation. The applied voltage has the task of separating this charges to detect the produced current or voltage. This setup principle is shown in figure 2.15.

If the applied voltage is too low, the produced particles can recombine before being detected, thus, leading to measurement errors. On the other hand, if the voltage is too high, the electrons and ions gain so much energy that they can produce secondary electrons themselves, yielding measurement errors too. Therefore ionization chambers have to be used in the so called ion-chamber-operating-

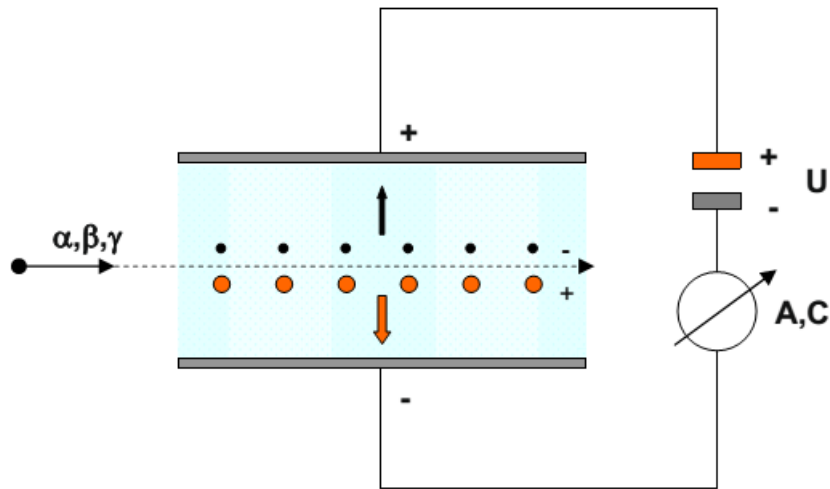


Figure 2.15: Principle of an ionization chamber (from [3], p28).

region, where the collection of ion pairs is nearly constant over a limited range of voltage [3].

2.4 Monte Carlo Method

Using randomly happening events for simulating actual experiments traces back to the 18th century, where a French scientist called Georges Louis Clerc, Comte de Buffon, used such a method to calculate the value of π . His ansatz followed the idea, that tossed needles thrown onto a board separated with parallel lines, can be used to estimate π . He conducted his experiments by throwing baguettes - the French tool of choice for everything - over his shoulder onto a tile floor.

Today's form of simulation was first used during the Second World War, when several problems developing the nuclear bomb occurred. John von Neumann and Stanislaw Ulam proposed a method, named after the Monte Carlo Casino in Monaco, to investigate the propagation of neutrons through matter. Nowadays a lot of different simulation techniques build on this first efforts, ranging from weather forecasting to medical physics [8, 9].

Monte Carlo calculations became a very popular tool for investigating complex problems, which can not be solved by analytical methods. In particular proba-

bilistic interactions between two objects are simulated by determining a random sample of the possible interactions, until the result converges. Since most of these interactions can be described mathematically to a certain extent, the repeated calculations necessary are predestined for the execution on computers [10].

A simple pattern uses three steps to build a simulation. First, a model of a system of interest has to be build consisting of probability density functions. As second step, the density functions are used for sampling. Finally, the statistically interesting outputs are computed. Here several problems occur concerning the accuracy of the model, generating random numbers for the probability density functions or picking the correct density function [8].

In radiation physics, the pattern mentioned above works by describing each particle individually. Depending on the applied physics model the interaction probabilities for every single particle are calculated in each step. Possible interactions are energy loss, ionizing, change of direction or even dose deposition. The algorithm repeats this procedure until the energy of a particle equals zero or a predefined cut-off value is reached. Again, the limiting factors for this simulations are the precision and reliability of the physics models and probability functions [11].

Covering tasks like treatment planning or diagnostic imaging, Monte Carlo methods evolved to a standard tool in the field of nuclear medicine, radiation therapy and radiology. Recently, it became more and more important to assess questions of dosimetry and radiation transport in matter. In treatment planning systems (TPS), for example, Monte Carlo tools are implemented to calculate the dose delivered to specific regions in the patient's tissue [12]. As described in the presented thesis Monte Carlo algorithms can also be utilized to calculate the dose deposition of kV X-ray tubes as an alternative method to model based algorithms [13–15]. Fuchs et al. have recently shown that TPS using Monte carlo algoritms can be used to study novel ions for their potential use in radiation therapy [16, 17].

Another example where these simulation tools are used, is the earlier mentioned field of imaging. In some imaging systems, like in positron emission tomography (PET), tracers (e.g. ^{18}F FDG) are applied in which radioactive decays produce the particles used to reconstruct an image of the region of interest [18]. Since

radioactive decay is a statistical effect, these systems are well suited for the use of Monte Carlo based calculation methods [1].

GATE, the GEANT4 Application for Tomographic Emission, is at present one of the few applications providing an easy-to-use framework for Monte Carlo simulations concerning all the topics of imaging, radiation therapy and dosimetry at once. It is based on the GEANT4 toolkit. GEANT4 handles the kernel which simulates and calculates the physics processes, whereas GATE takes care of the features to design a GEANT4-based simulation (see section 3.7). GATE is an open source software presenting every single user with the opportunity to participate in its development [13]. Besides GATE some other tools are freely available, covering different fields of research. FLUKA for example, is a Fortran based tool for modeling and simulating particle transport and interactions ranging from neutrino physics to radiotherapy [19, 20].

3 Materials

3.1 X-Ray Tube - YXLON Maxishot

The oil-cooled YXLON Maxishot produced by YXLON International GmbH, Hamburg, as shown in figure 3.1, is a commercially available X-ray unit. Its dimensions are 1374 x 663 x 2040 mm³. Radiation protection is achieved by a 10 mm lead layer on each side of the inner cabin, whereas the left side has a 12 mm thick layer. Thus, the YXLON Maxishot is a full protection device and no other radiation protection, as for example room shielding, is needed for the user. The X-ray tube, which is placed on the right side of the device, is capable of producing an accelerating voltage from 10 to 320 kV. However, it is limited to 200 kV maximum voltage and a maximum anode current of 20 mA. Normally, for the YXLON device the X-ray tube is placed on top, which makes the YXLON Maxishot used in this study a special construction for MedAustron and provides a horizontal reference beam, which makes it directly comparable to beams from the available synchrotron.

In figure 3.1 the X-ray tube is located on the right side where the cathode anode direction is top to bottom. The X-ray unit can be used for a wide variety of experiments, ranging from dosimetric investigations to biological studies [21–23]. The main focus of the device modeled during this thesis is to provide a reference situation for cell experiments performed in the horizontal proton beamline available at MedAustron [24, 25].

The target consists of tungsten and has a target angle of 20°. Furthermore, the user can choose a focus size of 3 or 5.5 mm. 3 mm Be is used as inherent filtration in the beam exit window, with the option to apply additional filtering of 3 mm Al and 0.5 mm Cu [26].

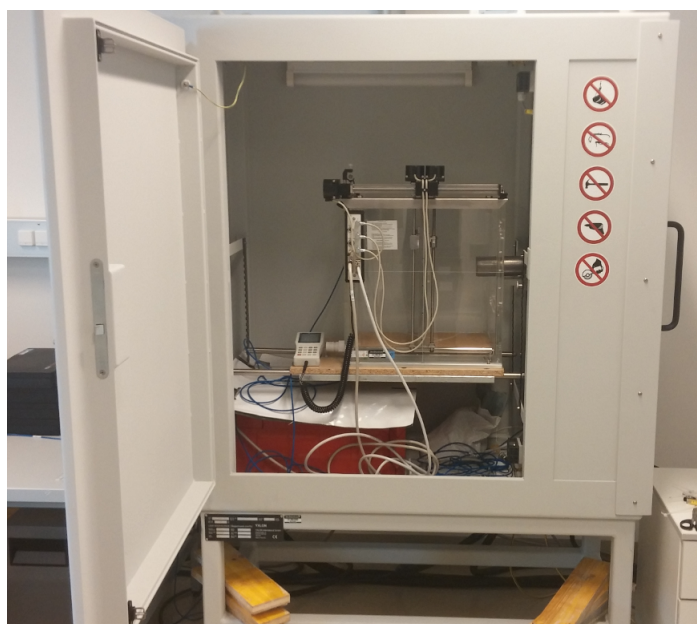


Figure 3.1: YXLON Maxishot at MedAustron

3.2 Scintillator based Sensor - LYNX

The LYNX device (figure 3.2) produced by Fimel in France, is a combination of a high resolution scintillation screen and a charge coupled device (CCD) detector. In principle it can be used as an alternative to film measurements [27]. It has an analysis area of $300 \times 300 \text{ mm}^2$ with an analysis resolution of 0.5 mm. With this type of detector it is possible to detect and investigate size and shape of a particle or photon beam. The scintillator converts the incoming particles into photons which are then detected by the CCD camera. The camera has a resolution of 1024×1768 pixels and the analog to digital converter delivers its data in a 12-bit format. Data transfer to an attached computer is achieved via an Ethernet cable. Using the supplied IBA software different acquisition and correction procedures, as for example exposure time, can be chosen. After the picture is taken, several analysis options provided by the software can also be applied [28].

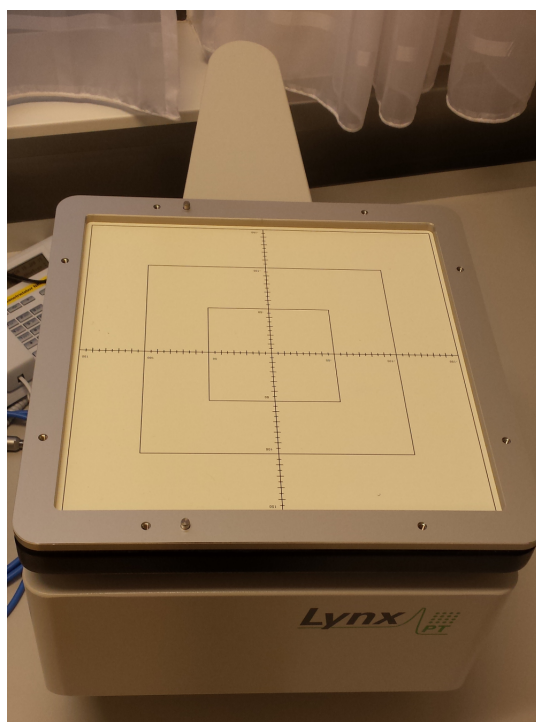


Figure 3.2: The LYNX device

3.3 Water Phantom - Perspex Tank

Figure 3.3 shows the Perspex Tank, which is included in the MP3-P Therapy Beam Analyzer L981403 system, produced by PTW in Freiburg. This tank consists of several PMMA plates which are glued together. The wall thickness is 18 mm with a removable window of 250 x 250 mm² and 5 mm thickness. Its outside dimensions are 484 x 498 x 386 mm³ and it can hold approximately 72 l of water. A moving system made of stainless steel is attached to the tank. Different detectors can be mounted and moved in three independent directions. Moving range limits are 350 mm for the A-axis, 380 mm for the B-axis and 250 mm for the C-axis, where A is a moving horizontal arm, B a moving vertical arm and C a moving horizontal arm with a slider. Movement is controlled by stepper motors with a step size of 0.1 mm and a positioning accuracy of 0.5 mm. With the provided software MEPHYSTO measurement properties can be adjusted, as for example step size, moving ranges and measurement time. Geometrical positions are reproducible with an error of about 0.1 mm. Additionally, moving range limits can be adjusted

manually, ensuring that the detector does not move out of range and for example hit a wall or any other obstacle inside the tank [29].

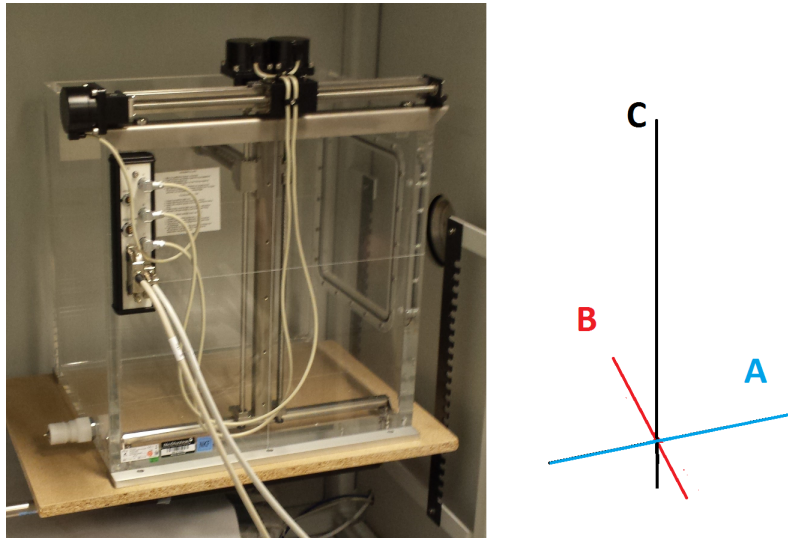


Figure 3.3: Perspex tank and orientation of the axes

3.4 Ionization Chamber

The ionization chamber type 31010 produced by PTW in Freiburg, Germany, (as seen in figure 3.4) is one potential detector in radiation therapy for dose and dose rate measurements. Its measuring volume of 0.125 mm^3 is shielded by a watertight outer shell. The measuring range for dose measurements ranges from 0.6 mGy to 6.6 Gy, and for dose rate measurements from 3.6 mGy/min up to 18,000 mGy/min. For both, dose and dose rate, the reference point is situated 4.5 mm behind the chamber tip. The chamber works in a voltage range from 100 to 400 V, with the latter being the nominal voltage. At this nominal voltage a maximum dose rate of 6 Gy/s at continuous radiation or 0.5 mGy maximum dose per irradiation pulse are detectable. The rated energy range of use is specified from 66 keV to 50 MeV [30].

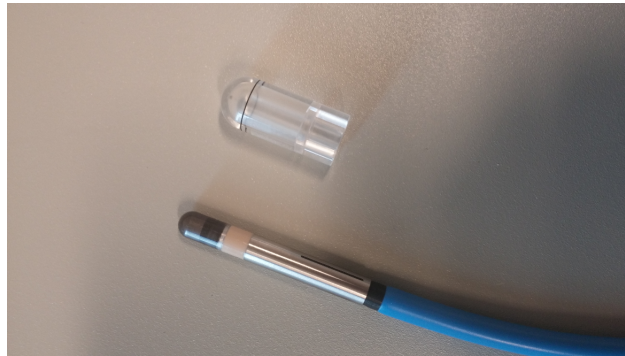


Figure 3.4: The semi-flexible chamber type 31010

3.5 NOMEX Multimeter

The NOMEX Multimeter T11049, as shown in figure 3.5, is a dosimetry system designed for absolute dosimetric measurements and quality assurance in X-ray diagnostics [31, 32]. It includes a software for controlling the device and its properties, as well as displaying the measured results. Along with the detector itself comes a multimeter, which can alternatively be connected to the detection device. Via this multimeter nearly the same control options are available as via the external software. Therefore, it is not absolutely necessary to connect the device to a computer.

The multi-channel semiconductor detector measures dose, dose rate, dose per pulse, number of pulses, puls frequency, radiation time, tube voltage, total filtering in mm Al, HVL thickness and ripple of tube voltage and dose rate. Dose can be measured from 50 nGy up to 500 μ Gy and dose rate from 0.1 to 500 mGy. The HVL thickness ranges from 1.5 to 40 mm and the total filtering in mm Al from 0.25 to 13.5 mm Al. Two different measurement modes are available, with the voltage limits in the mammography mode ranging from 23 to 35 kV and in the conventional diagnostic mode from 40 to 150 kV. Measurement and error ranges depend on the actual settings applied to the device and have to be looked up in the manual for each specific measurement [33].



Figure 3.5: The NOMEX Multimeter system (from [33], p1).

3.6 X-Ray Spectra Software SpekCalc

To simulate the output spectrum produced by the YXLON Maxishot X-ray tube, the software *SpekCalc*, developed by Poludniowski et al., was used [34–36]. It is a commercially available program designed to simulate the photon spectra produced in a tungsten anode. The algorithm uses data sets of electron penetration depths and electron energy distributions gained by Monte Carlo simulations. Bremsstrahlung cross sections are calculated with analytical methods and the self-filtration is described semi-empirically. Combining these elements of two different approaches, from true Monte Carlo simulations and semi-empirical models, *SpekCalc* delivers results without any notable delay on a standard computer. Additionally both, program and output data, are very small concerning their file size (below 10 MB). Another advantage of *SpekCalc* is, that it provides the user with information about HVLs and mean energy (see figure 3.6). However, one major disadvantage is its restriction to a Windows or Mac operating system [34].

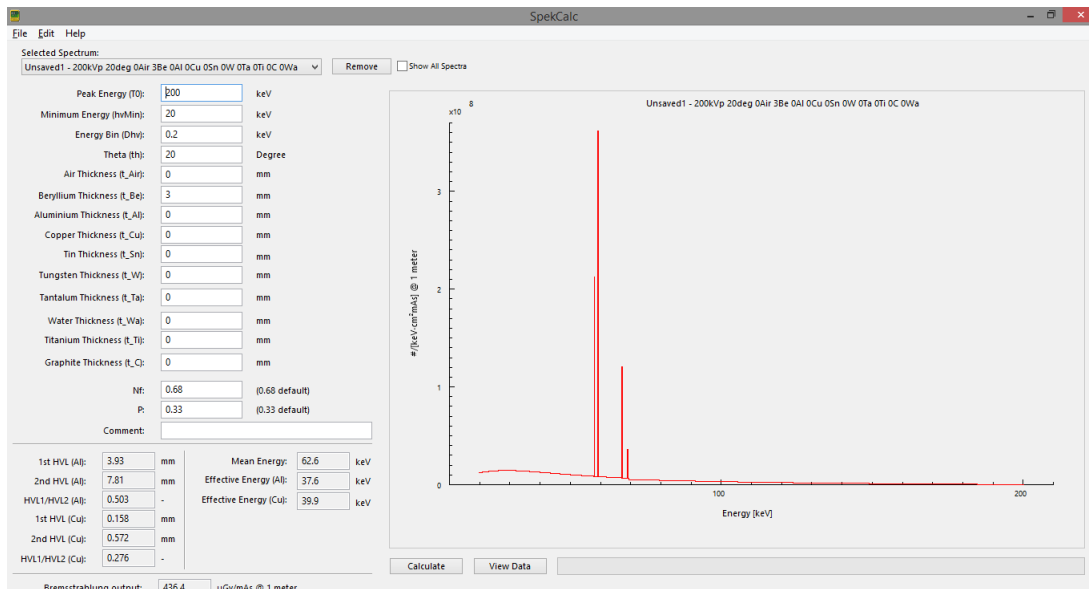


Figure 3.6: *SpekCalc* graphical user interface showing all input parameters

3.7 Monte Carlo Toolkit GATE

One common framework used for Monte Carlo simulations in modern physics today is the GEANT4 simulation toolkit. GEANT4 covers a wide variety of physics processes, from electromagnetic interactions in the eV-regime to processes occurring at some TeV. It is a result of a worldwide collaboration of scientists and includes several user-friendly functions to build, simulate and evaluate an actual experiment or system. Built using the C++ programming language and following object-orientated technologies, it can be easily adapted and evaluated by users, which mostly come from the field of nuclear and particle physics [37].

The earlier mentioned framework GATE is based on the provided GEANT4 functions and classes and provides the user with features to simplify the development of simulations. The design of GATE consists of the *core layer*, the *application layer* and the *user layer*. As indicated in figure 3.7, these three layers are based on GEANT4, with the first two building the so called *developer layer*. All classes define interfaces usable for developing new features. Classes which are required in GEANT4, such as geometry or physics, are situated in the *core layer*. In addition,

GATE specific classes like its virtual clock are included as well. The *application layer* contains all derived classes to build specific geometries or adapt physical processes. Developments concerning new features for the GATE framework are done in this specific layer, leaving the inner core untouched. The real powerful advantage is implemented in the *user layer* providing the user with a command interpreter and the option to work interactively or by using pre-defined scripts. Therefore no C++ coding is necessary [1].

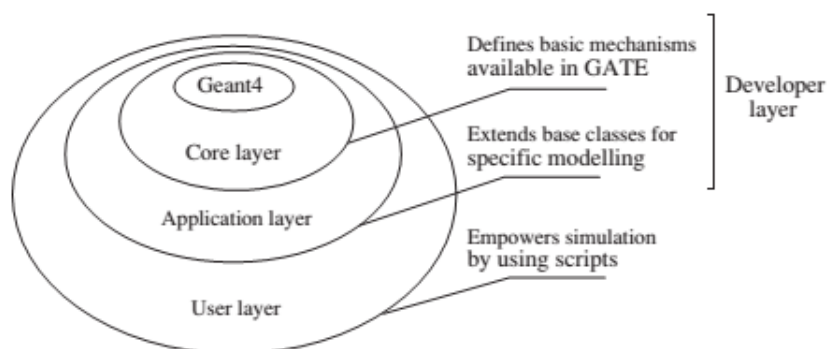


Figure 3.7: Layered architecture of GATE (from [1], p4).

One major part of the simulation's architecture is the applied physics model to compute the occurring interactions. Here, several lists are available with different parameters and settings for the implemented models. For modeling electromagnetic interactions, for example *emstandard*, *emlivermore* and *empenelope*. Each list is designed for a specific energy range. The names of the lists indicate the implemented mathematical models. For the simulation of hadronic interactions, as an example, the list *QGSP_BERT_EMZ* is available. This list applies a quark gluon string model for high energy interactions [37–39]. In the present study, the *emlivermore* list, designed for electromagnetic interactions, was investigated and its simulation results were compared to the outcome of the *QGSP_BERT_EMZ* list to analyze the influence of taking hadronic processes into account.

3.8 Data Analysis Framework ROOT

To handle the enormous data amounts produced by the LHC experiments at CERN (around 10 Terabytes), a new data analysis tool had to be developed, since the old ones could not fulfill the requirements of modern high energy physics experiments anymore. At CERN the NA49 experiment provided a suitable environment for testing new tools, which resulted in the development of ROOT. Nowadays, the fact that GATE takes into account a lot of different particles and interactions between them producing large amounts of data, together with the advantage of being thoroughly tested in such an environment, plays to ROOT's strength and makes it a favorable choice as storing and analysis tool. In this study ROOT is used as analysis tool, since a high number of particle interactions were investigated in each simulation.

ROOT is built in a hierarchical structure, consisting of about 250 classes organized in about 20 frameworks which are divided in 9 categories. The classes contain features as 1D, 2D and 3D histograms, Trees and NTuples and many more. This structure provides the user with a big variety of options to store and process data.

One major advantage of ROOT is its object database, which is also built in a hierarchical way. This database is especially designed to handle a lot of manipulations of its entries in a highly efficient and fast way. Since the database has to store a big amount of all kinds of data, ROOT uses a compression algorithm based on the well known gzip algorithm. It provides the user with 9 different levels of compression with 1 being the default one.

The framework also comes with a C/C++ interpreter called CINT, providing the user with the possibility to use self-developed scripts or work interactively with ROOT using CINT as a command line interpreter. Since its beginning a lot of very useful functions and features have been implemented, extremely simplifying the development of programs based on ROOT [40].

4 Methods

4.1 Experiments on Beam Characteristics

To characterize the beam quality provided by the YXLON Maxishot, experiments were conducted in air to measure HVLs and to determine the shape of the beam. The latter was achieved by measuring beam profiles. After this experiments, the half value layers in PMMA (polymethyl methacrylate, also known as Plexiglas) at different energies with both, Al and Al-Cu filtering, were measured. Finally, using the previously mentioned Nomex Multimeter and the LYNX system, additional information concerning the HVLs and beam profiles were collected.

4.1.1 Measurements with Ionization Chamber and Perspex Tank

To determine the properties of the X-ray beam, dose measurements were conducted inside the Perspex tank. The tank was placed upon a wooden plate, with the plate being mounted in a way, that the upper side was 68 cm above the ground of the YXLON Maxishot's inner cabin. The semi-flexible ionization chamber type 31010 from PTW was mounted inside the tank using the PTW TRUFIX system [41].

4.1.1.1 Depth Dose Profile

The detector's zero point was set to be 73 cm above the base, 14 cm away from the exit window and 29.8 cm from the back wall. At each run 345 data points, using 1 mm step size, were collected, with a measuring time of 2 s for every point. The depth dose profile was measured at two different distances. The first run started at 14 cm and the second one at 39 cm distance from the exit window. The latter

was achieved by simply moving the wooden plate and the water phantom as far away as possible from the tube exit window. The experiments were performed at 50, 100, 150 and 200 kV tube voltage. Measurements were conducted at each of these energies with 3 mm Al filtration and with a combination of 3 mm Al and 0.5 mm Cu.

4.1.1.2 Cross- and Inplane Profile

For the determination of the crossplane and inplane profile, the same setup as in the depth dose profile measurements was used. Again measurements were conducted at 50, 100, 150 and 200 kV tube voltage, with 3 mm Al and 3 mm Al combined with 0.5 mm Cu filtration. 191 data points for inplane and 195 for crossplane measurements were recorded, with a measurement time of 2 s per point. For the crossplane measurements the upper limit was set in the MEPHYSTO software to -65 mm and the lower limit to $+130$ mm. Inplane limits ranged from -120 mm to $+71$ mm. Figure 4.1 shows the limits and orientation as used by the MEPHYSTO software in beam's eye view.

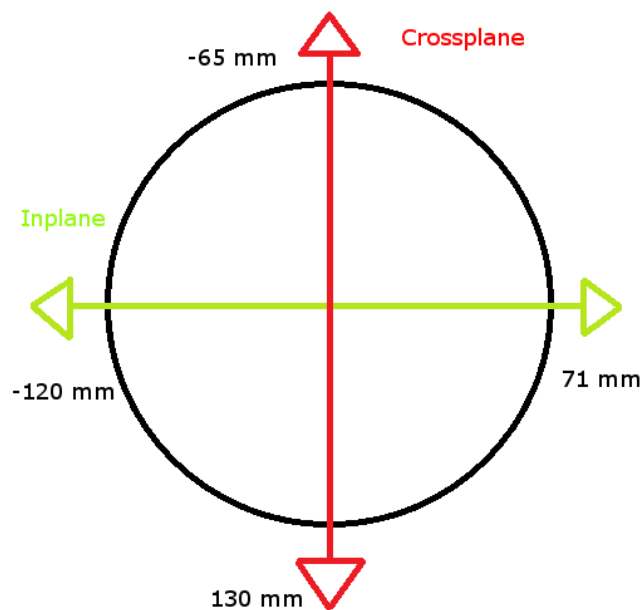


Figure 4.1: Definition of cross- and inplane and measurement ranges in beam's eye view.

4.1.2 Half Value Layers in PMMA

For the determination of HVLs in PMMA an Al box was used. The purpose of this box was to mount the semi-flexible ionization chamber type 31010 from PTW and to conduct the experiments with different thicknesses of PMMA. In total 12 cm of PMMA was available, with plate thicknesses of 10, 5, 2, and 1 mm. A special PMMA plate of 1 x 30 x 30 cm³, where the detector could be inserted from above, was used to mount the ionization chamber right in the center of the Al box (see figure 4.2). The detector's distance from the exit window was set to 32.4 cm. Additionally, the Al box was placed on the wooden plate such that the detector was 29.8 cm away from the back wall and 74 cm above the base.

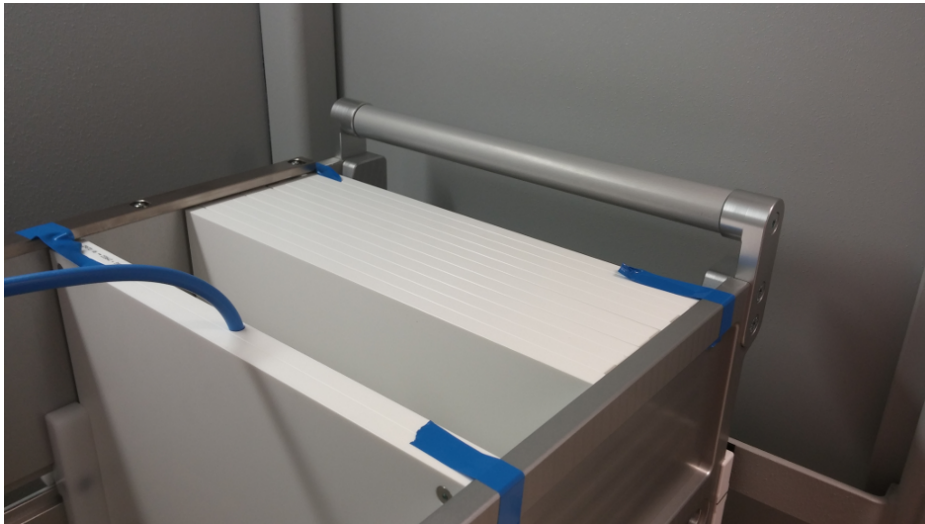


Figure 4.2: Al box filled with PMMA plates

The experiments were conducted at 50, 100, 150 and 200 kV tube voltage, with 3 mm Al and 3 mm Al together with 0.5 mm Cu filtration. To determine the first and second HVL, first measurements were done with only the PMMA plate containing the detector. Afterwards PMMA plates were inserted into the Al box one by one, until the dose dropped to a half and to a quarter of the initial value. The standard PMMA plates used were 30 x 30 cm² with a thickness of 1 cm.

4.1.3 Nomex Measurements

To get additional information about the X-ray output provided by the YXLON Maxishot measurements with the NOMEX Multimeter system were conducted. The detector was placed upon a PMMA box such that it was facing the tube exit window and was in the center of the X-ray beam. Measurements were done using both, 3 mm Al filtering and 3 mm Al together with 0.5 mm Cu filtering. For each different beam filtering, eight different tube voltages were investigated: 25, 50, 75, 100, 125, 150, 175 and 200 kV. The aim of these experiments was the determination of the HVL in mmAl as well as the total filtering in mmAl as provided by the NOMEX system. For energies below 50 kV and above 150 kV the NOMEX system could not provide data for the total filtration in mmAl.

4.1.4 LYNX Measurements

The LYNX system was used to take pictures of the beam produced by the X-ray unit. It was placed inside the YXLON upon the wooden plate with its sensitive area facing the tube exit window such that the full focal spot could be detected by the CCD. This was achieved by placing it closely to the exit window.

Main purpose of these measurements was the determination of the beam shape, in order to simulate the correct shape in the GATE simulations afterwards. Furthermore, these images can also be used to depict the inplane and crossplane profiles of the beam.

4.2 Simulations

4.2.1 Parameters for SpekCalc

The X-ray spectra used as input for the GATE simulations were obtained using the software *SpekCalc*. The parameters shown in table (4.1) were the input parameters to calculate the spectrum. By choosing the *Peak Energy* and the *Minimum Energy*, a specific energy range is available for the spectrum, but the *Minimum Energy* is restricted to be at least 10 % of the *Peak Energy*. The parameter *Energy Bin* adjusts the bin size in the calculated spectrum and was chosen to be 0.2 keV

for all simulations. This bin size was necessary, since GATE allowed only 1024 histogram points in a user defined spectrum. *Theta* refers to the angle between the tungsten target and the electron beam in the X-ray tube and was set to 20° [26]. Additional beam filtration can be applied using the *Thickness* parameter for the different materials. *SpekCalc* uses two model parameters, *Nf* and *P*, which were both set to their default values. Details on these parameters can be found in Poludniowski et al. [34].

Peak Energy [keV]	50	100	150	200
Minimum Energy [keV]	5	10	15	20
Energy Bin [keV]	0.2	0.2	0.2	0.2
Theta [°]	20	20	20	20
Nf	0.68	0.68	0.68	0.68
P	0.33	0.33	0.33	0.33

Table 4.1: Initial parameters to generate the input X-ray spectrum using *SpekCalc*

Spectra were simulated at 50, 100, 150 and 200 keV *Peak Energy*. For each energy no filtration, 3 mm Be, 3 mm Be and 3 mm Al and finally 3 mm Be, 3 mm Al and 0.5 mm Cu were applied as filtration. Thus, in total 16 different spectra were obtained.

4.2.2 GATE Simulations

To simplify the development and debugging of the simulation, it was split up into several files shown in figure 4.3. Each part fulfilled a specific task needed for the simulation to work correctly.

The file *main.mac* connected all parts of the simulation and provided the main simulation parameters, as for example the number of particles or which material database was used. Additionally, in this file it was possible to conduct a geometry check, that detected possible overlaps of objects, which could result in simulation errors. Inside *visualize.mac* options concerning the visual output could be controlled. This mac file was not used in the actual simulations, but was of big help during the development phase concerning consistency checks of the geometry. *geometry.mac* contained all information about the YXLON Maxishot device.

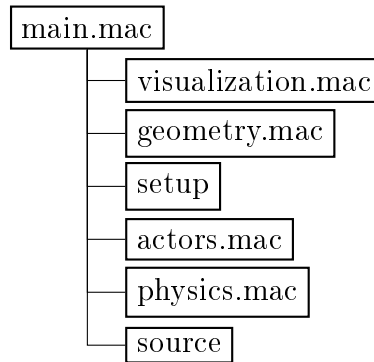


Figure 4.3: Architecture of the GATE simulation

Since five different setups were simulated, one had to choose the desired setup in *main.mac* by simply removing the comment operator `#` in the corresponding line. Every setup used was stored in the *mac* folder along with the other mac files. Inside *actors.mac* the three actors used in every simulation were defined: a statistics actor for counting the number of particles and measuring the simulation time, an energy spectrum actor for storing the energy spectrum and an actor counting the number of particles destroyed in the kill actor. The applied physics model and its parameters were set in *physics.mac*. All different sources used were stored in the folder *data* along with the database *GateMaterials.db* containing all information about the defined materials. The folder *output* contained the collected data stored by the different actors.

Since the particle number in GATE is stored in a 32-bit unsigned integer variable and is thus limited to 4.294.967.295, each simulation was performed 5 times with $4 \cdot 10^9$ particles to increase the statistic. Afterwards the output files were merged using the *hadd* function provided by ROOT.

4.2.2.1 Sources

The spectra generated by *SpekCalc* were used in GATE by defining a so called histogram, with respect to the fact that *SpekCalc* uses keV, whereas a GATE histogram reads the energy in MeV. The angular distribution was defined using two angles, θ and ϕ . Table 4.2 shows the applied values.

Angle	Minimum [°]	Maximum [°]
θ	67	113
ϕ	-23	23

Table 4.2: Limits for the angular distribution of the X-ray source

4.2.2.2 Setups

As mentioned above, five setups were simulated in this study, investigating different properties of the X-ray beam provided by the YXLON Maxishot device. The computed results were then compared to available experimental data to verify the accuracy of the simulations.

alu_block.mac In this setup a simple Al block of 3 cm thickness and a surface size of 50 x 50 mm² was inserted into the YXLON Maxishot geometry. The block was positioned such that it was completely inside the X-ray beam. The purpose of this simulation was to investigate the HVL in mmAl using different beam filtrations and compare it to the results gained with the NOMEX Multimeter system. Simulation data was collected using a *TLEDoseActor* with a voxel size of 0.1 x 50 x 50 mm³, which was attached to the Al block and saved using the ROOT data format.

Simulations were done at four different tube voltages and with different filtration thicknesses and combination as depicted in tables 4.3 and 4.4.

A simulation series with four energies was then performed where the combination of Be, Al and Cu filtration was replaced by a single Al filter. The thickness of this filter was set accordingly to the value of the total mmAl filtration detected by the NOMEX system at the specific energy, which can be found in table 5.2.

Finally, the beam filters were removed from the GATE geometry and the filtered spectra simulated using *SpekCalc* were used to investigate possible differences in the filtering process between GATE and SpekCalc.

Each simulation was performed on the basis of two different physics lists, *emlivermore* and *QGSP_BERT_EMZ*, to investigate possible differences and get the best suiting parameters for simulating the experimentally measured setups.

Physics List	emlivermore			QGSP_BERT_EMZ		
Al-Filter [mm]	2.5	3.0	3.5	2.5	3.0	3.5
Energy [keV]	50	50	50	50	50	50
	100	100	100	100	100	100
	150	150	150	150	150	150
	200	200	200	200	200	200

Table 4.3: Energies and filter thicknesses used to simulate *alu_block.mac* with an applied Al-filter of varying thickness.

Physics List	emlivermore								
Al-Filter [mm]	2.5			3.0			3.5		
Cu-Filter [mm]	0.4	0.5	0.6	0.4	0.5	0.6	0.4	0.5	0.6
Energy [keV]	50	50	50	50	50	50	50	50	50
	100	100	100	100	100	100	100	100	100
	150	150	150	150	150	150	150	150	150
	200	200	200	200	200	200	200	200	200

Physics List	QGSP_BERT_EMZ								
Al-Filter [mm]	2.5			3.0			3.5		
Cu-Filter [mm]	0.4	0.5	0.6	0.4	0.5	0.6	0.4	0.5	0.6
Energy [keV]	50	50	50	50	50	50	50	50	50
	100	100	100	100	100	100	100	100	100
	150	150	150	150	150	150	150	150	150
	200	200	200	200	200	200	200	200	200

Table 4.4: Energies and filter thicknesses used to simulate *alu_block.mac* with an applied Al-Cu-filter of varying thickness.

aluminium_PMMA_phantom.mac The Al box with the inserted PMMA plates was modeled to compare the quality of the simulation to the experimental data. In order to account for occurring scatter effects, the mounting elements inside the YXLON Maxishot, the four metal struts and the two pipes upon which the wooden plate was placed, were modeled too. Placed upon the wooden plate was the Al box, consisting of the two side walls, four posts and the two handles. A simple box of $30 \times 30 \times 30 \text{ cm}^3$ was placed inside the box and its material set to *PMMA* to simulate the PMMA plates used in the experiment (see figure 4.4). To attach a *TLEDoseActor*, the PMMA box contained a daughter object called *phantomPDD* with a cross section of $1 \times 1 \text{ cm}^2$ and 30 cm length. Data was stored in voxels of $1 \times 10 \times 10 \text{ mm}^3$ in the *output* folder in ROOT files. Therefore, the depth dose profile could be determined with a resolution of 1 mm.

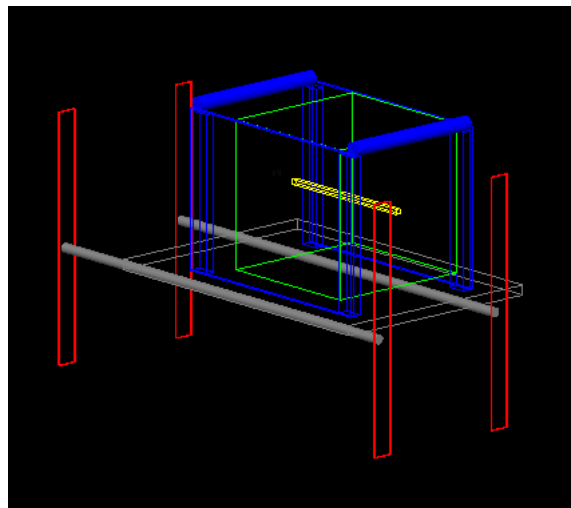


Figure 4.4: GATE model of the Al box (blue) containing the PMMA box (green cube), with the actor (yellow) placed inside.

The simulations were done using the *emlivermore* physics list and with the spectra for 50, 100, 150 and 200 kV, where the Be filtration was already considered in *SpekCalc*. Two different filtrations, namely 3 mm Al and a combination of 3 mm Al and 0.5 mm Cu, were used.

One simulation at each of the four energies was conducted with an unfiltered initial spectrum. Here the filtration was done directly in GATE by an Al filter with

a thickness corresponding to the value of total mm Al measured with the NOMEX multimeter (see table 5.2). This Al-filter replaced the Be-Al-Cu combination.

water_phantom.mac In this setup the Perspex tank used in the measurements for the determination of the beam characteristics in air was modeled. To account for possible scattering effects the mounting of the tank, consisting of the four metal struts where the two metal pipes holding the wooden plate was placed, was also included in the corresponding mac file *water_phantom.mac*. The tank itself consisted of a back and two side walls, which were 18 mm thick and made of PMMA. At the front side, closer to the tube exit window, four parts were used to model the tank's entry window. An extra part was included in the mac file, describing the window, which was only of 1 mm thickness. It was possible to exclude it in a simulation by simply using the comment operator `#`. The model can be seen in figure 4.5.

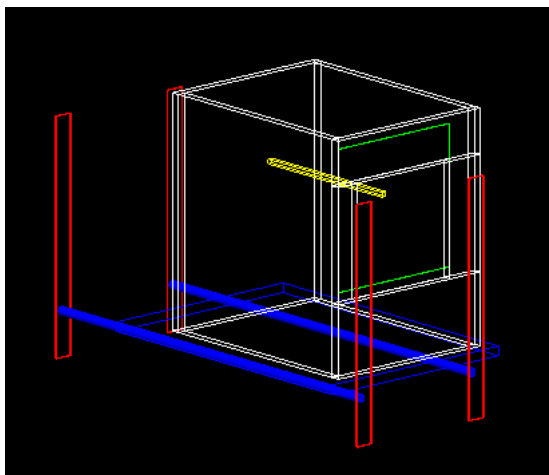


Figure 4.5: GATE model of the Perspex tank (white), with the actor *phantomPDD*(yellow) and the actor *phantomCrossAndInplane* (green).

Additionally, two objects called *phantomCrossAndInplane* and *phantomPDD* were inserted into the tank. Two actors of the type *TLEDoseActor* were used in the simulation. The *phantomPDD* actor had a voxel size of $1 \times 10 \times 10 \text{ mm}^3$, whereas *phantomCrossAndInplane* stored its data in voxels of $1 \times 1 \times 1 \text{ mm}^3$. These actors were attached to their corresponding phantoms. The data collected in each

actor was saved in the *output* folder using ROOT files. As physics list *emlivermore* was chosen.

cell_irradiation.mac To model biological cell irradiation setups, the same mounting as previously described for the water phantom was included, but the wooden plate being substituted by an object named *plasticfloor*. This object was made of PMMA and its dimensions were 402 x 20 x 400 mm³. On top of it another PMMA box was placed, which worked as the platform for the actual flask. In the simulated biological experiments a T75 cell flask was used. The flask was modeled using a simple box of 182 x 223 x 30 mm³ and functioned as the mother object for the actual flask, where two daughter objects were inserted. One daughter object modeled the flask's neck and was a trapezoidal object, where the *X-*, *Y-* and *ZBoxLength* parameters were set to 0.1 mm and positioned on the upper edge of the structure. This extruded box was required by GATE, but was of no use in this specific simulation and therefore its parameters were set such that it had minimal effect on the outcome of the simulations. The second object was a simple box of 86 x 74 x 28 mm³ for the bottom structure of the flask. Both objects inserted had dimensions such that a 1 mm thick outer shell was created. Again a *TLEDoseActor* was used to save data in ROOT files and attached to the mother object of the flask. Figure 4.6 shows the setup as it was build in GATE.

Simulations were done with three different predefined filling materials for the flask. The first was *Air*, the second one *Water* and the third material was *Air2*, which had twice the density of *Air*. All materials were defined in *GateMaterials.db*. A combination of 3 mm Al und 0.5 mm Cu was applied as filtration. The chosen physics list was *emlivermore*. As source, the Be-filtered spectra of 50, 100, 150 and 200 keV were used.

lead_collimator.mac This setup was build to simulate a collimated photon pencil beam. Furthermore, this setup enables to investigate on the influence of PMMA on the beam shape and size. The computed results were compared to previously conducted measurements, where the collimated beam was recorded with the LYNX camera.

The geometry was made of the mounting, again consisting of the four metal

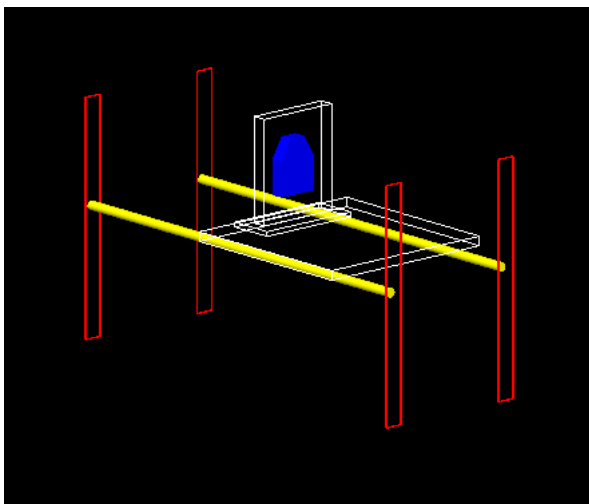


Figure 4.6: GATE model of the cell irradiation setup. The flask (blue) is inserted into the holder (white).

struts and two metal pipes upon which a wooden plate was placed. To mount the PMMA plates the Perspex tank was used in the experiments, and therefore the model described in the previous section was inserted into this geometry setup, but without the window. This was achieved by using the comment operator `#` in the mac file on all commands regarding the window. The lead collimator was modeled using a cylinder of 160 mm length and by setting R_{min} to 50 mm and R_{max} to 60 mm. A second cylinder described the small exit window of the collimator with R_{min} being 1.5 mm and R_{max} 60 mm. Its height was set to 20 mm. Thus, a collimator with a round opening ($r = 1.5$ mm) was simulated. Finally, a PMMA object with a cross section of 30×30 cm² was included between the collimator's exit window and the phantom used to attach the actor. The mentioned phantom was a simple air box of 1 mm thickness in x direction, had a cross section of 15×15 cm² and was placed directly behind the PMMA object. Again a *TLEDoseActor*, with a voxel size of $1 \times 0.5 \times 0.5$ mm³, was used to store the collected data in the ROOT data format. These files were written into the *output* folder. In figure 4.7 the modeled geometry is shown.

One simulation was done with no PMMA box, and five with a varying PMMA thickness of 1, 2, 3, and 5 mm. The beam energies used were 150 and 200 kV. These setups were simulated for three different filtration types. One

type consisted of the Be pre-filtered spectrum, with the 3 mm Al and 0.5 mm Cu filter simulated separately in GATE. Secondly, the NOMEX values for the total filtration in mm Al were used, as listed in table 5.2, to replace the Be-Al-Cu-filter modeled in GATE with a filter consisting only of Al. The third one used the pre-filtered spectra obtained with *SpekCalc*, where Be, Al and Cu have been included. *emlivermore* was the applied physics list.

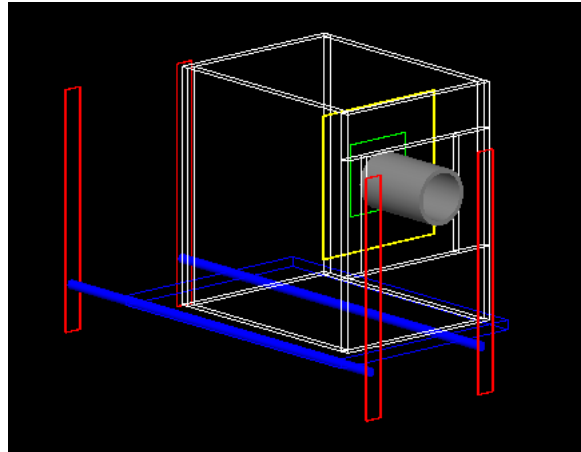


Figure 4.7: GATE model of the Perspex tank (white) with the lead collimator (grey). The PMMA plate (yellow square) was placed between the collimator and the actor (green square).

5 Beam Characteristics

5.1 Half Value Layers

5.1.1 Measurements with Ionization Chamber and Perspex Tank

The first and second HVL were measured inside the Perspex tank with the semi-flexible ionization chamber type 31010 from PTW (see section 3.4). Using these values the HF was calculated according to equation 2.23 and is shown in table 5.1 along with the values for the 1. and 2. HVL. The applied filtration was 3 mm Al and 3 mm Al combined with 0.5 mm Cu, respectively.

	Al-Filter				Al-Cu-Filter			
	50	100	150	200	50	100	150	200
Energy [kV]	50	100	150	200	50	100	150	200
1. HVL [mm]	88	90	90	90	78	93.5	91	92
2. HVL [mm]	214	224	226	225	173	235	228	231
HF	0.41	0.40	0.40	0.40	0.45	0.40	0.40	0.40

Table 5.1: HVLs and HFs measured inside the Perspex tank.

5.1.2 Nomex Measurements

The NOMEX Multimeter system was used to determine the half value layers in Al as an alternative measurement technique; the respective results are shown in table 5.2. Additionally, the device detected the applied pre-filtration of the X-ray beam in the unit mm Al. These results are shown in the column *Filtration* in table 5.2. Measurements were conducted in an energy range from 50 to 200 kV with a step

size of 25 kV. At energies below 50 kV the dose produced by the YXLON Maxishot was too low and the HVL as well as the total filtration in mm Al could not be detected with the Nomex Multimeter. A similar problem arose at energies above 150 kV, where it was impossible to determine the HVL due to the specification of the device. Filtration materials used were 3 mm Al and 0.5 mm Cu.

Energy [kV]	Al-Filter		Al-Cu-Filter	
	HVL [mmAl]	Filtration [mmAl]	HVL [mmAl]	Filtration [mmAl]
50	1.84	2.67	4.36	20.47
75	2.62	2.27	6.99	21.80
100	3.62	2.30	8.95	22.30
125	4.78	2.40	10.24	22.53
150	5.86	2.40	11.26	22.30
175	—	2.67	—	22.00
200	—	2.63	—	21.97

Table 5.2: HVLs and total filtration in mm Al measured with the NOMEX Multimeter system at different energies and filter combinations. Deviations for the HVLs are ± 0.25 mm and for the total Filtration in mm Al ± 0.5 mm.

5.2 Beam Profiles

5.2.1 Measurements with Ionization Chamber and Perspex Tank

For the crossplane dosimetric measurements inside the Perspex tank, where the semi-flexible ionization chamber type 31010 from PTW was used, the results in table 5.3 were collected. The filtration materials were 3 mm Al and 0.5 mm Cu. In this table the maximum dose is shown together with the position of 60 % of the maximum on the left and right side. These positions are given in reference to the measurement limits shown in figure 4.1. The difference between these two was calculated to get the dimensions of the beam shape. In table 5.4 the values for the

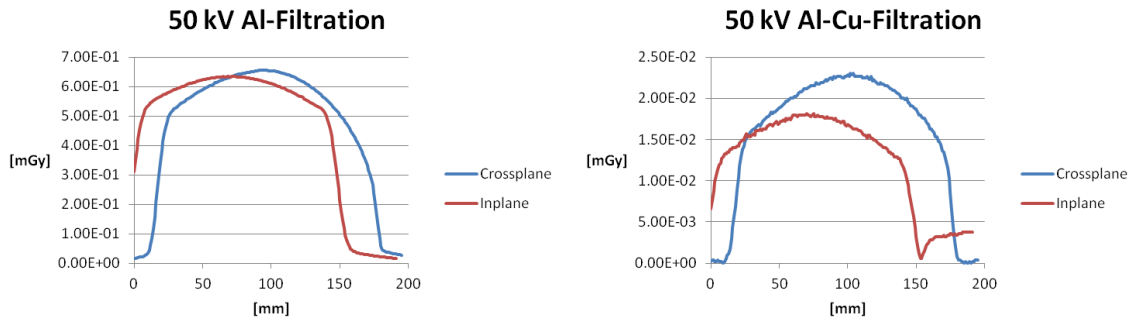
inplane dosimetric measurements are shown. Figures 5.1 - 5.4 show the various profiles from the cathode to the anode side. The intensity drop on the anode side due to the Heel effect can be observed in the crossplane profiles, where only Al was applied as filtration (see figure 5.4a). Additional Cu filtration leads to more absorption of low energy photons resulting in a more homogeneous intensity of the X-ray beam and removal of the Heel effect.

	Al-Filter				Al-Cu-Filter			
	50	100	150	200	50	100	150	200
Energy [kV]	50	100	150	200	50	100	150	200
Max. [Gy/min]	0.66	2.87	5.94	9.75	0.02	0.63	2.15	4.52
60% [Gy/min]	0.39	1.72	3.57	5.85	0.01	0.38	1.29	2.71
Pos. 60% left [mm]	-44.5	-46.0	-46.5	-47.0	-42.0	-45.0	-46.0	-46.5
Pos. 60% right [mm]	100.0	98.0	96.0	95.0	104.0	106.0	103.0	103.0
Distance [mm]	144.5	144.0	142.5	142.0	146.0	151.0	149.0	149.5

Table 5.3: Results from the crossplane dosimetric measurements.

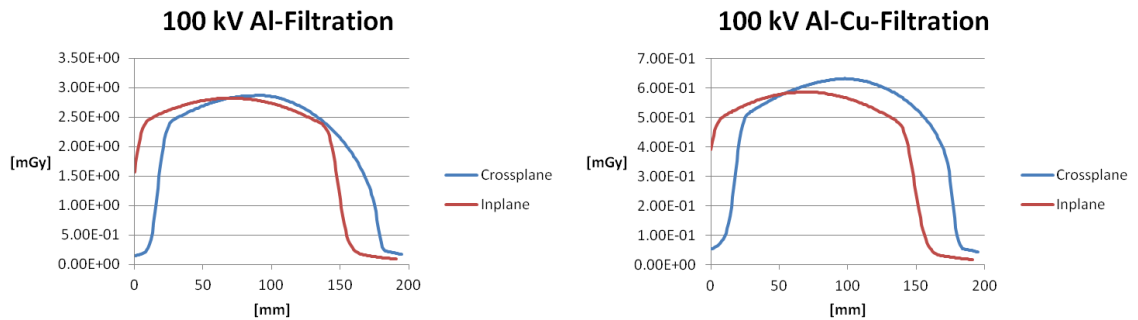
	Al-Filter				Al-Cu-Filter			
	50	100	150	200	50	100	150	200
Energy [kV]	50	100	150	200	50	100	150	200
Max. [Gy/min]	0.64	2.82	5.90	9.69	0.01	0.59	2.06	4.37
60% [Gy/min]	0.38	1.69	3.54	5.81	0.007	0.35	1.24	2.62
Pos. 60% left [mm]	-69.0	-70.0	-71.0	-71.0	-57.0	-71.0	-71.0	-71.0
Pos. 60% right [mm]	74.5	75.0	76.0	76.0	67.0	75.0	76.0	76.0
Distance [mm]	143.5	145.0	147.0	147.0	124.0	146.0	147.0	147.0

Table 5.4: Results from the inplane dosimetric measurements.



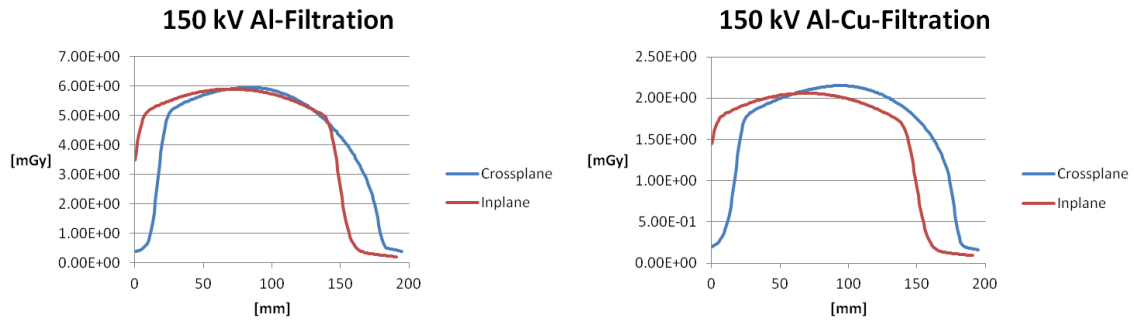
- (a) Cross- and inplane profiles obtained at 50 kV tube voltage with 3 mm Al filtration.
- (b) Cross- and inplane profiles obtained at 50 kV tube voltage with 3 mm Al and 0.5 mm Cu filtration. The peak shortly after 150 mm results from scattering strongly influencing the low dose measurements.

Figure 5.1: Measured profiles inside the Perspex tank at 50 kV with different filtrations.



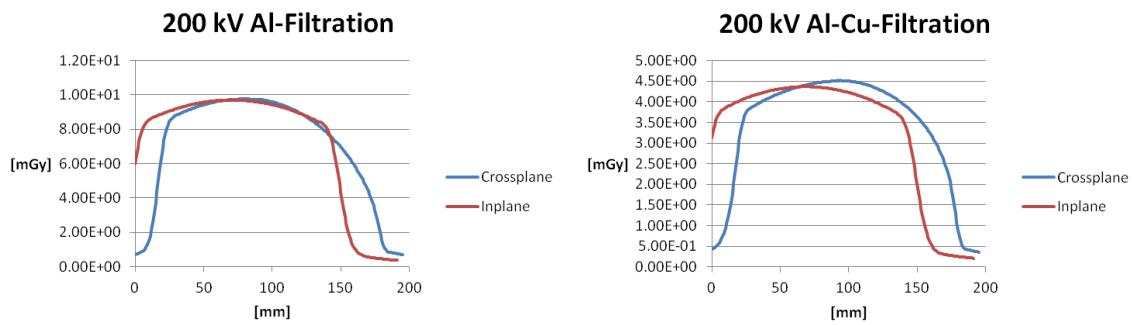
- (a) Cross- and inplane profiles obtained at 100 kV tube voltage with 3 mm Al filtration.
- (b) Cross- and inplane profiles obtained at 100 kV tube voltage with 3 mm Al and 0.5 mm Cu filtration.

Figure 5.2: Measured profiles inside the Perspex tank at 100 kV with different filtrations.



(a) Cross- and inplane profiles obtained at 150 kV tube voltage with 3 mm Al filtration. (b) Cross- and inplane profiles obtained at 150 kV tube voltage with 3 mm Al and 0.5 mm Cu filtration.

Figure 5.3: Measured profiles inside the Perspex tank at 150 kV with different filtrations.



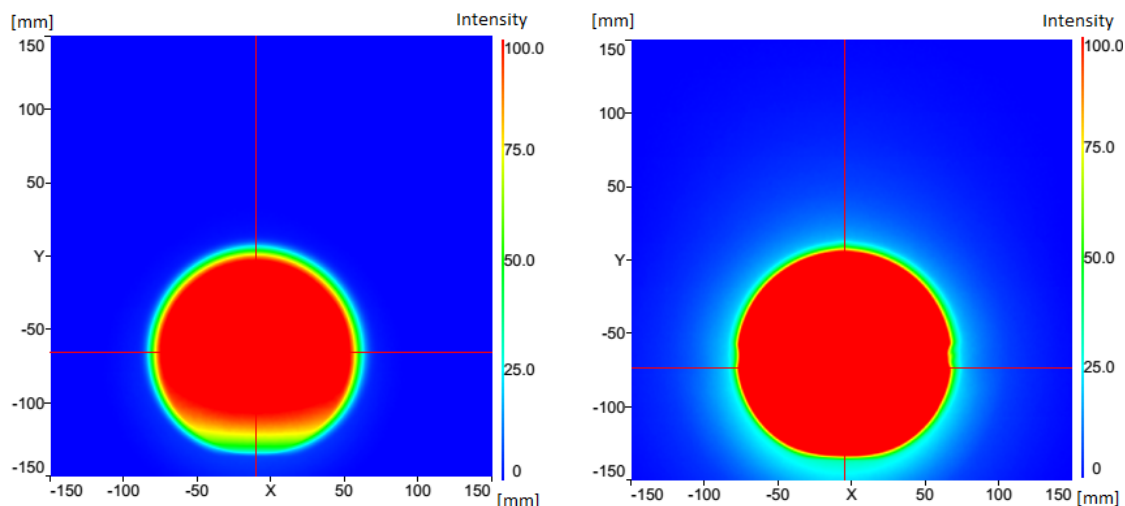
(a) Cross- and inplane profiles obtained at 200 kV tube voltage with 3 mm Al filtration. (b) Cross- and inplane profiles obtained at 200 kV tube voltage with 3 mm Al and 0.5 mm Cu filtration.

Figure 5.4: Measured profiles inside the Perspex tank at 200 kV with different filtrations.

5.2.2 LYNX Measurements

With the LYNX system the dose distributions shown in picture 5.5 were recorded. The first one was obtained with no additional filtration in the tube exit window and the second one with additional 3 mm Al and 0.5 mm Cu filtration.

The cross- and inplane profiles are shown in figures 5.6 and 5.7, for no additional filtration and 3 mm Al with 0.5 mm Cu filter thickness, respectively.



(a) Unfiltered beam isodose. The red lines indicate the position of the profiles shown in figure 5.6. (b) Beam isodose filtered with 3 mm Al and 0.5 mm Cu. The red lines indicate the position of the profiles shown in figure 5.7.

Figure 5.5: Beam isodoses at 200 kV for an unfiltered and a Al-Cu-filtered beam.

For both, the unfiltered and the filtered beam, the corresponding profiles in the center of the X-ray beam are indicated in figure 5.5 by red lines and are shown in figures 5.6 and 5.7. Due to saturation effects which occurred in the LYNX, the profiles are cut off in the high dose region. The crossplane profile for the unfiltered beam shows an intensity decrease, which can be seen on the left side of figure 5.6, caused by the Heel effect. This decrease is not occurring when applying an additional Al-Cu-filtration.

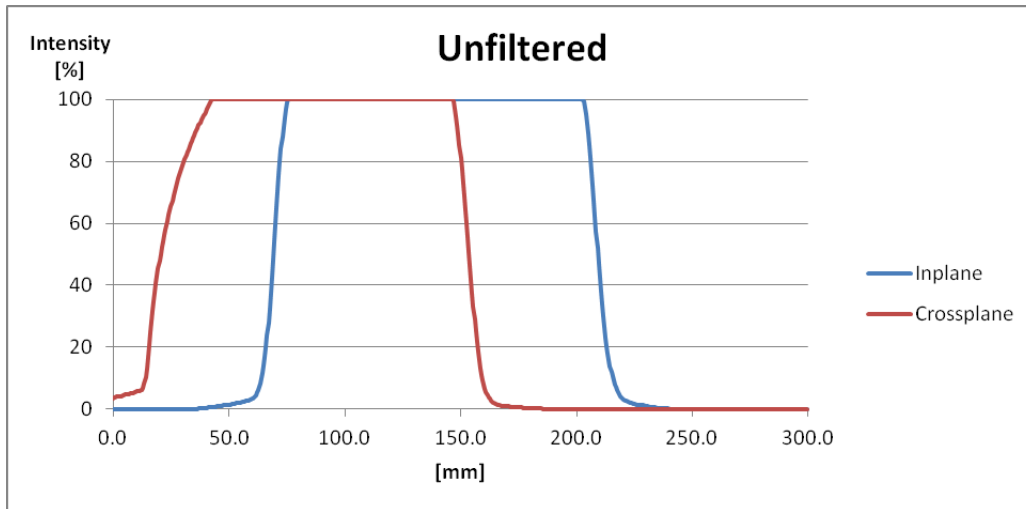


Figure 5.6: Cross- and Inplane profiles with no additional filtration determined using the LYNX system. Saturation of the CCD causes the cut off in the high dose region. On the left side of the crossplane profile the intensity decrease caused by the Heel effect can be observed.

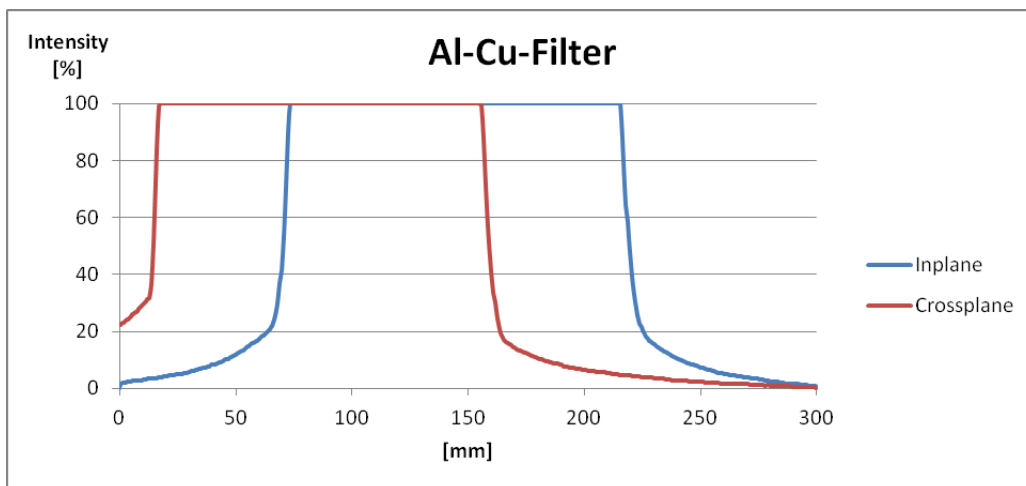


Figure 5.7: Cross- and Inplane profiles with 3 mm Al and 0.5 mm Cu filtration determined using the LYNX system. Saturation of the CCD causes the cut off in the high dose region.

5.3 Half Value Layers in PMMA

The dosimetric measurements performed at four different energies in the Al box and with a different number of PMMA plates, yielded the results shown in table 5.5. All data were collected using the semi-flexible ionization chamber type 31010 from PTW. As filtration materials 3 mm Al and 0.5 mm Cu were used. For the Al-Cu combination the second HVL could not be measured, since the dose drop was not steep enough to be measurable with the available number of PMMA plates (in total 120 mm PMMA). However, since the intensity drop follows equation 2.11, the interpolated values for the 2. HVL are shown in table 5.5 using an asterisks.

	Al-Filter				Al-Cu-Filter			
	50	100	150	200	50	100	150	200
Energy [kV]	50	100	150	200	50	100	150	200
1.HVL [mm]	23	33	41	45	30	61	62	65
2.HVL [mm]	50	80	81	120	56*	130*	143*	150*
HF	0.46	0.41	0.51	0.38	0.54	0.47	0.43	0.43

Table 5.5: 1. and 2. HVLs and HF in PMMA for different beam energies and filter combinations. Values with a * are interpolated using equation 2.11, since they were not measurable for the Al-Cu filter combination.

6 Simulations

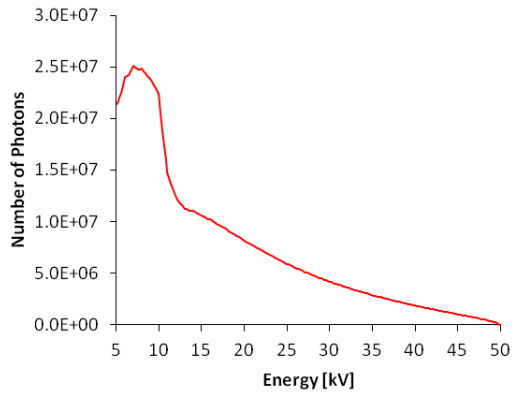
6.1 SpekCalc

The spectra simulated with the software *SpekCalc* are displayed in figures 6.1 - 6.4 and show the influence of different filtrations at different energies. As the figures clearly demonstrate the prominent characteristic x-ray peaks (see equation 2.16) become more dominate for larger energies.

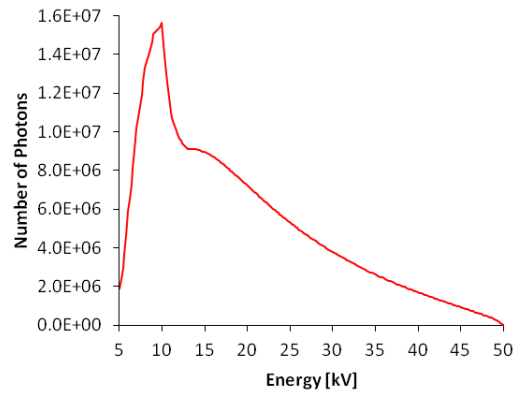
In addition to the spectrum, *SpekCalc* also provided values for the 1. and 2. HVL in mm Al and mm Cu together with the HF. The computed results at energies ranging from 25 to 200 kV, using steps of 25 kV, are listed in table 6.1. As filtration the 3 mm inherent Be was used in combination with 3 mm Al as well as additional 0.5 mm Cu.

Energy [kV]	Al-Filter			Al-Cu-Filter		
	1. HVL [mm]	2. HVL [mm]	HF	1. HVL [mm]	2. HVL [mm]	HF
25	0.77	0.84	0.92	1.21	1.21	1.00
50	1.87	2.44	0.77	4.47	4.72	0.95
75	2.66	3.86	0.69	7.00	7.65	0.92
100	3.50	5.45	0.64	8.83	9.70	0.91
125	4.37	6.96	0.63	10.10	11.10	0.91
150	5.25	8.32	0.63	11.10	12.20	0.91
175	6.15	9.53	0.65	11.90	13.10	0.91
200	7.09	10.60	0.67	12.70	14.00	0.91

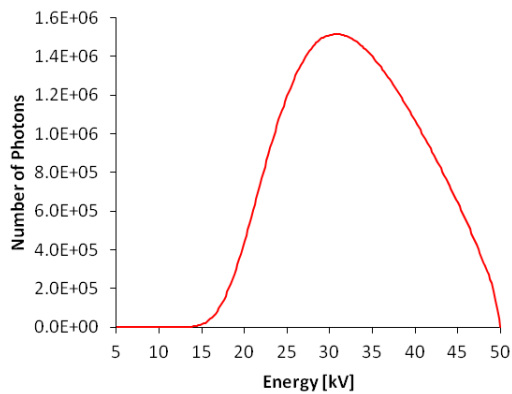
Table 6.1: HVLs and HFs calculated with *SpekCalc*. Filtration parameters were 3 mm Be and 3 mm Al and additional 0.5 mm Cu for Al-Cu-filtering.



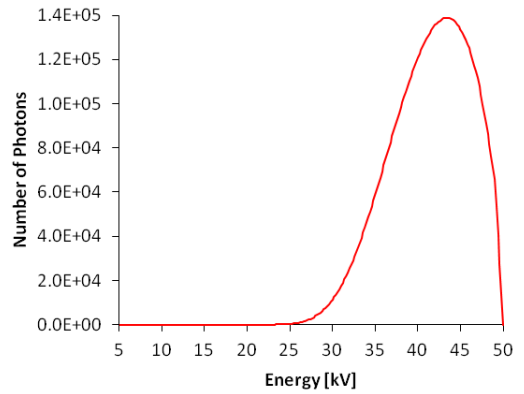
(a) Unfiltered 50 kV spectrum.



(b) 50 kV spectrum with 3 mm Be-filter in the tube exit window.

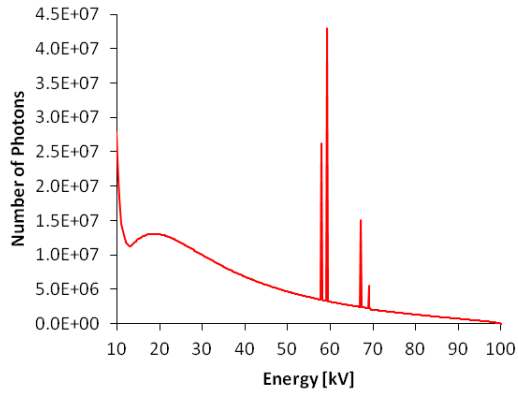


(c) 50 kV spectrum with 3 mm Be in the tube exit window and additional 3 mm Al filtration.

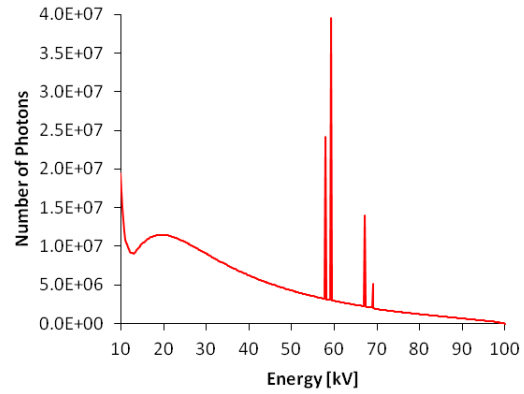


(d) 50 kV spectrum with 3 mm Be in the tube exit window and additional 3 mm Al and 0.5 mm Cu filtration.

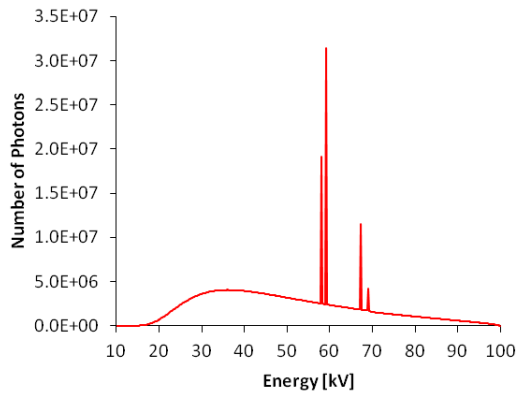
Figure 6.1: Spectra at 50 kV with different filtrations.



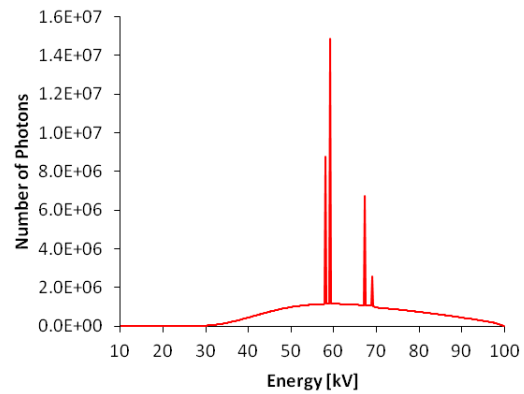
(a) Unfiltered 100 kV spectrum.



(b) 100 kV spectrum with 3 mm Be-filter in the tube exit window.

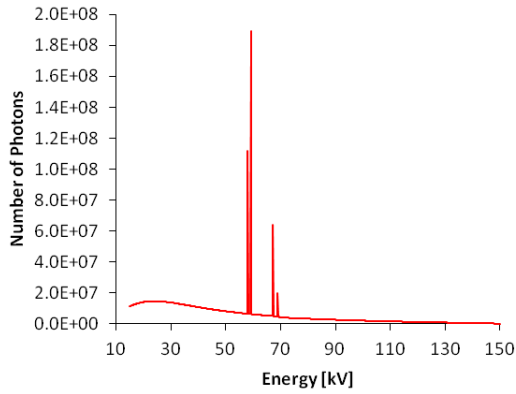


(c) 100 kV spectrum with 3 mm Be in the tube exit window and additional 3 mm Al filtration.

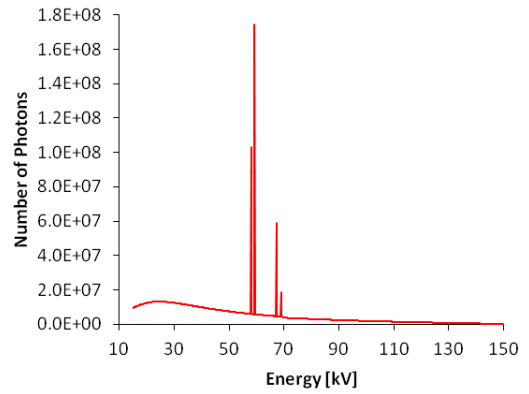


(d) 100 kV spectrum with 3 mm Be in the tube exit window and additional 3 mm Al and 0.5 mm Cu filtration.

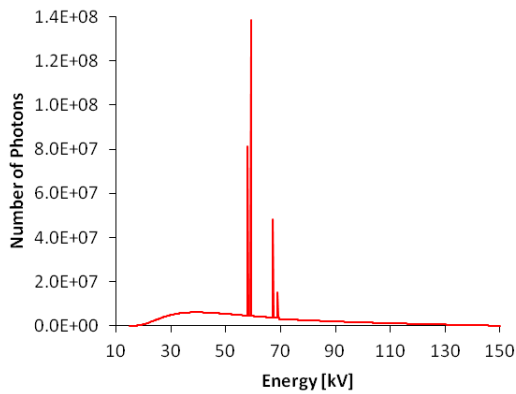
Figure 6.2: Spectra at 100 kV with different filtrations.



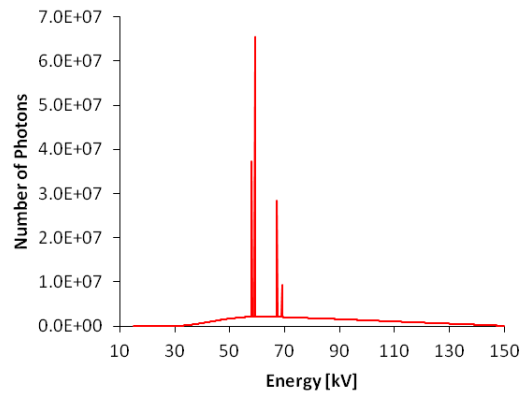
(a) Unfiltered 150 kV spectrum.



(b) 150 kV spectrum with 3 mm Be-filter in the tube exit window.

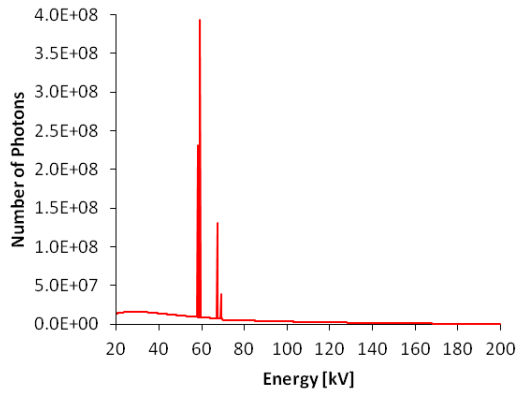


(c) 150 kV spectrum with 3 mm Be in the tube exit window and additional 3 mm Al filtration.

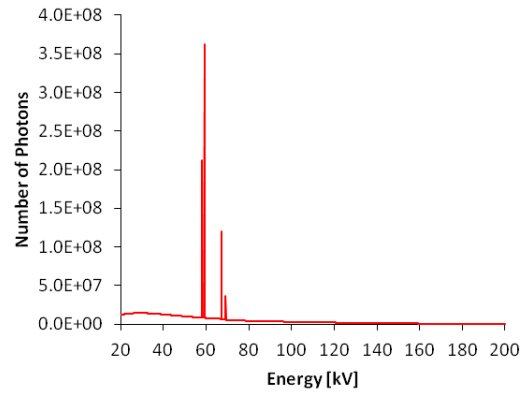


(d) 150 kV spectrum with 3 mm Be in the tube exit window and additional 3 mm Al and 0.5 mm Cu filtration.

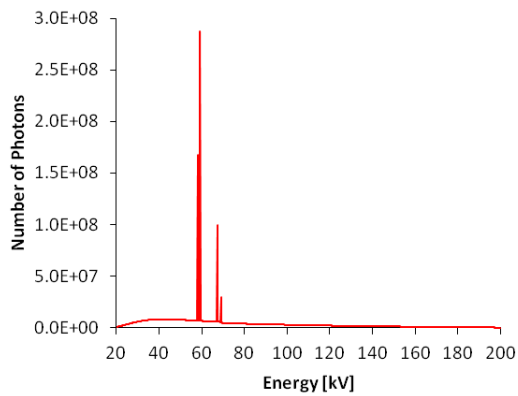
Figure 6.3: Spectra at 150 kV with different filtrations.



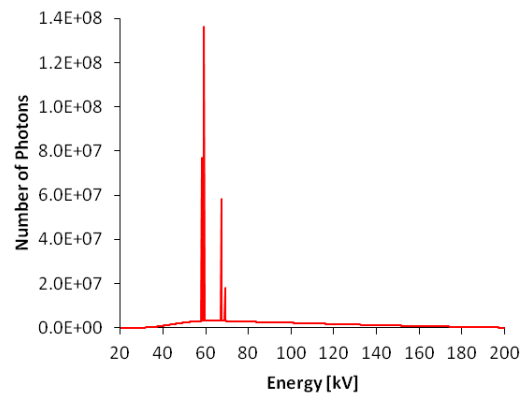
(a) Unfiltered 200 kV spectrum.



(b) 200 kV spectrum with 3 mm Be-filter in the tube exit window.



(c) 200 kV spectrum with 3 mm Be in the tube exit window and additional 3 mm Al filtration.



(d) 200 kV spectrum with 3 mm Be in the tube exit window and additional 3 mm Al and 0.5 mm Cu filtration.

Figure 6.4: Spectra at 200 kV with different filtrations.

6.2 Half Value Layers in mm Al

6.2.1 Al-Filter

GATE simulations using two different physics lists, *emlivermore* and *QGSP_BERT_EMZ* (as described in section 3.7), and 3 thicknesses of Al as additional filtration were conducted. All spectra loaded in GATE already contained an inherent filtration of 3 mm Be as applied in *SpekCalc*. For comparison between the two physics lists the HVLs for different energies are listed in table 6.2, where the values obtained with the *QGSP_BERT_EMZ* list are given in brackets.

Al-Filter in GATE				
Al-Filter [mm]	2.5	3.0	3.5	
Energy [kV]	HVL [mm]			
50	1.9 (1.9)	2.2 (2.2)	2.4 (2.4)	
100	3.5 (3.5)	3.9 (3.9)	4.3 (4.3)	
150	4.9 (4.9)	5.5 (5.5)	5.9 (6.0)	
200	6.4 (6.5)	6.9 (6.9)	7.4 (7.4)	

Table 6.2: GATE simulations of HVLs in Al with with different filter thicknesses at four energies. The applied physics lists were *emlivermore* and *QGSP_BERT_EMZ*. Results for the latter are shown in brackets.

6.2.2 Al-Cu-Filter

Simulations were conducted for 9 different thickness combinations of additional Al-Cu-filtering at four different energies. For comparison, two physics lists, as mentioned before were applied. The results for the HVLs in mm Al are listed in table 6.3, where the ones for the *QGSP_BERT_EMZ* physics list are shown in brackets. Besides evaluating two potential physics lists for the simulation, investigating different filter thicknesses can show general offset values between simulation and measurement.

Al-Cu-Filter in GATE				
Energy [kV]	50	100	150	200
Al-Filter [mm]	2.5			
Cu-Filter [mm]	HVL [mm]			
0.4	5.1 (5.0)	10.2 (10.1)	12.3 (12.3)	13.5 (13.5)
0.5	5.4 (5.4)	11.1 (11.1)	13.1 (13.4)	14.3 (14.3)
0.6	5.7 (5.7)	11.6 (11.6)	13.8 (13.8)	14.8 (14.8)
Al-Filter [mm]	3.0			
Cu-Filter [mm]	HVL [mm]			
0.4	5.1 (5.1)	10.4 (10.4)	12.5 (12.8)	13.6 (13.7)
0.5	5.5 (5.4)	11.2 (11.1)	13.2 (13.2)	14.4 (14.4)
0.6	5.8 (5.7)	11.7 (11.7)	13.8 (13.8)	14.9 (15.0)
Al-Filter [mm]	3.5			
Cu-Filter [mm]	HVL [mm]			
0.4	5.2 (5.2)	10.5 (10.5)	12.5 (12.5)	13.7 (13.7)
0.5	5.5 (5.5)	11.2 (11.2)	13.2 (13.2)	14.4 (14.3)
0.6	5.7 (5.7)	11.4 (11.5)	13.6 (13.6)	14.7 (14.7)

Table 6.3: GATE simulations of HVLs at four energies with different Al-Cu-filter thicknesses. The applied physics lists were *emlivermore* and *QGSP_BERT_EMZ*. Results for the latter are shown in brackets.

6.2.3 Single Al-Filter

Based on the results acquired with the Nomex Multimeter, the three different filters were replaced with a single Al filter. Its thickness was set according to the values presented in table 5.2. *emlivermore* and *QGSP_BERT_EMZ* were used as physics list at four different energies. The HVLs in mm Al gained from the calculations are presented in table 6.4. For the sake of comparison the results obtained with *QGSP_BERT_EMZ* are shown using brackets.

Single Al-Filter in GATE		
Energy [kV]	Al-Filter [mm]	HVL [mmAl]
50	20.47	5.3 (5.3)
100	22.30	10.8 (10.8)
150	22.30	12.9 (12.9)
200	21.97	13.9 (13.9)

Table 6.4: Single Al-Filter at different energies and filtrations using two different physics lists, *emlivermore* and *QGSP_BERT_EMZ*. Results for the latter are shown in brackets. The Al-filter thickness was set according to table 5.2.

6.2.4 Filtration in SpekCalc

Additionally to the implementation of the filtering effects in the GATE framework, the software *SpekCalc* was used to compute pre-filtered spectra which were then used as input for the actual simulations. In addition to the inherent 3 mm Be the filtration thicknesses applied in the software were 3 mm Al and 0.5 mm Cu, respectively. Simulations were conducted at four different energies and with *emlivermore* as well as *QGSP_BERT_EMZ* as physics list. The HVLs for both lists are shown in table 6.5, with the values for the *QGSP_BERT_EMZ* list shown in brackets.

	Al-Filter in <i>SpekCalc</i>	Al-Cu-Filter in <i>SpekCalc</i>
Energy [kV]	HVL [mmAl]	
50	2.1 (2.1)	5.4 (5.4)
100	3.9 (3.9)	11.0 (11.0)
150	5.5 (5.5)	13.2 (13.2)
200	7.0 (7.0)	14.3 (14.3)

Table 6.5: HVLs simulated in GATE with Al- and Al-Cu-filtration done in *SpekCalc*. The filter thicknesses set were 3 mm Be, 3 mm Al and 0.5 mm Cu. As physics list *emlivermore* and *QGSP_BERT_EMZ* were used, with the results of the latter shown in brackets.

6.3 Beam Profile

The model for the Perspex tank, as described in the mac file *water_phantom.mac* in section 4.2.2, was used to simulate the HVLs and the beam profile. Two different predefined GATE materials, namely *Air* and *Air2*, were used to model the air inside the YXLON's cabin.

The energy ranged from 50 to 200 kV. In addition to the HVLs the beam profiles in cross- and inplane directions were simulated. As cut-off criterium the 60%-value of the dose maximum was used. This value is used to describe the size of the X-ray beam.

6.3.1 Al-Filter

With the 3 mm Al filter applied in the tube exit window, the results for the HVLs and the HF shown in table 6.6 were computed. In table 6.7 the columns *Crossplane* and *Inplane* contain the distance from the 60% value on one side to the 60% value on the other side of the maximum for the cross- and inplane data. An example of the cross- and inplane profiles, which have the same shape in all simulations due to the beam parameters set in GATE, is shown in figure 6.5.

Al-Filter in GATE			
Energy [kV]	1. HVL [mm]	2. HVL [mm]	HF
50	76 (76)	187 (186)	0.41 (0.41)
100	75 (76)	186 (185)	0.40 (0.41)
150	76 (75)	186 (186)	0.41 (0.40)
200	76 (76)	187 (186)	0.41 (0.41)

Table 6.6: HVLs and HFs simulated for Al-filtration with two different air models. The results for *Air2* are given in brackets.

Al-Filter in GATE		
Energy [kV]	Crossplane [mm]	Inplane [mm]
50	145 (145)	145 (145)
100	145 (145)	145 (145)
150	145 (145)	145 (145)
200	145 (145)	145 (145)

Table 6.7: Cross- and inplane distances at different energies using Al-filtration simulated with GATE. Two different materials, *Air* and *Air2*, were used to model the air. Results for the latter are shown in brackets.

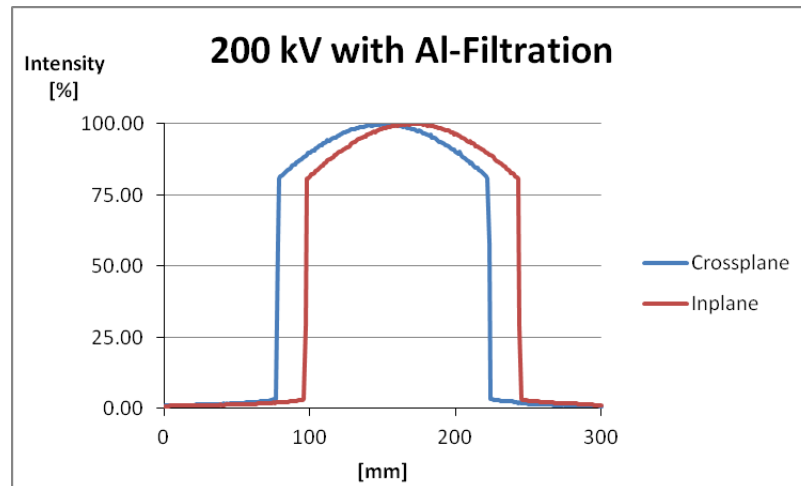


Figure 6.5: Simulation results for cross- and inplane profiles at 200 kV with additional 3 mm Al filtering.

6.3.2 Al- and Cu-Filter

At the same energies as before, simulations were done with 3 mm Al and 0.5 mm Cu as additional filtration. The 1. and 2. HVLs and the corresponding HFs are listed in table 6.8. For 50 kV the obtained dose was too low to get proper results. As filling material for the YXLON's inner cabin the GATE materials *Air* and *Air2* were used.

Al-Cu-Filter in GATE			
Energy [kV]	1. HVL [mm]	2. HVL [mm]	HF
100	77 (76)	189 (188)	0.41 (0.40)
150	76 (76)	187 (186)	0.41 (0.41)
200	76 (76)	186 (186)	0.41 (0.41)

Table 6.8: HVLs and HFs simulated for Al-Cu-filtration in GATE with two different air models, *Air* and *Air2*. Results for *Air2* are shown in brackets.

With the cross- and inplane profiles the size of the X-ray beam could be determined. The results gained for different energies are shown in table 6.9. Note that for the 50 kV simulation the resulting dose was too low to get proper data.

Al-Cu-Filter in GATE		
Energy [kV]	Crossplane [mm]	Inplane [mm]
100	145 (145)	145 (145)
150	145 (145)	145 (144)
200	145 (145)	145 (145)

Table 6.9: Cross- and inplane distances at different energies using Al-Cu-filtration simulated with GATE. Two different materials, *Air* and *Air2*, were used to model the air. Results for the latter are shown in brackets.

6.3.3 Single Al-Filter

Additionally, simulations were done, where the various filters were substituted by a single Al filter. The thickness of this filter was set in accordance to the measurement data achieved with the Nomex Multimeter for each specific setup and can be found in table 5.2. As material inside the YXLON only *Air* was considered. With the single Al filter the 1. and 2. HVL were simulated, as listed in table 6.10, and the corresponding HF calculated with equation 2.23.

Single Al-Filter in GATE			
Energy [kV]	1. HVL [mm]	2. HVL [mm]	HF
50	76	186	0.41
100	77	189	0.41
150	77	187	0.41
200	76	187	0.41

Table 6.10: HVLs and HFs calculated for a single Al-filter in GATE replacing Be-Al-Cu. The thickness of the Al-filter was set accordingly to table 5.2. As material *Air* was used.

In addition to the HVLs the spot size of the X-ray beam was determined (see also sections 6.5). The values calculated for the size in cross- and inplane direction are listed in table 6.11, where the 50 kV simulation yielded no usable results due to too little dose.

Single Al-Filter in GATE		
Energy [kV]	Crossplane [mm]	Inplane [mm]
100	147	146
150	148	148
200	149	149

Table 6.11: Cross- and inplane distances at different energies using a single Al-filter in GATE replacing the Be-Al-Cu combination simulated with GATE. Its thickness was set accordingly to the results from table 5.2. Here only the GATE material *Air* was used to model the air.

6.3.4 Filtration in SpekCalc

Finally, simulations using the Perspex model were conducted, where the filtration was achieved in the *SpekCalc* software, by setting the material parameters for filtration to 3 mm Be, 3 mm Al and 0.5 mm Cu. Subsequently, the pre-filtered spectra were used as GATE input. This was done in contrast to the previous simulations, where the filtration of the X-ray beam was computed separately with the Monte Carlo framework. Again the 1. and 2. HVL with their corresponding HF were simulated at 50, 100, 150 and 200 kV. For modeling the air, the GATE materials *Air* and *Air2* were used. Results can be found in tables 6.12 and 6.13. The cross- and inplane distances were also simulated for all different setups and are listed in table 6.14. These simulations were about 25 % faster compared to the simulations where all filters were modeled separately in GATE.

Al-Filter in <i>SpekCalc</i>			
Energy [kV]	1. HVL [mm]	2. HVL [mm]	HF
50	75 (75)	184 (183)	0.41 (0.41)
100	75 (75)	185 (184)	0.41 (0.41)
150	75 (75)	185 (185)	0.41 (0.41)
200	75 (75)	185 (185)	0.41 (0.41)

Table 6.12: HVLs and HF calculated for Al-filtration using *Air* and *Air2* as materials. Results for the latter are shown in brackets.

Al-Cu-Filter in <i>SpekCalc</i>			
Energy [kV]	1. HVL [mm]	2. HVL [mm]	HF
50	75 (75)	186 (186)	0.40 (0.40)
100	75 (75)	186 (186)	0.40 (0.40)
150	75 (75)	185 (185)	0.40 (0.40)
200	75 (75)	185 (185)	0.40 (0.40)

Table 6.13: HVLs and HF calculated for Al-Cu-filtration applied in *SpekCalc* using *Air* and *Air2* as materials. Results for the latter are shown in brackets.

Energy [kV]	Al-Filter in <i>SpekCalc</i>		Al-Cu-Filter in <i>SpekCalc</i>	
	Crossplane [mm]	Inplane [mm]	Crossplane [mm]	Inplane [mm]
50	145 (145)	145 (145)	145 (145)	145 (145)
100	145 (145)	145 (145)	145 (145)	145 (145)
150	145 (145)	145 (145)	145 (145)	145 (145)
200	145 (145)	145 (145)	145 (145)	145 (145)

Table 6.14: Cross- and inplane distances for Al- and Al-Cu-filtration in *SpekCalc* using *Air* and *Air2* as materials. Results for the latter are given in brackets.

6.4 Half Value Layers in PMMA

With the model of the Al box containing the inserted PMMA plates, simulations were done to calculate the HVLs and HFs for the same two filtration combinations of Al and Cu as described afore. For the HF equation 2.23 was used. Afterwards a single Al filter was used, which replaced the three different filter materials (Be, Al and Cu) similar to the procedure outline in section 6.3.3. Finally, the filtration was done in *SpekCalc* and again the HVLs and the HFs were computed. All results can be found in tables 6.15, 6.16 and 6.17. Each filtration was investigated at four different energies (50, 100, 150 and 200 kV tube voltage). For the 50 kV simulation with the Al-Cu filtration and the single Al filter in GATE no useful results could be determined due to too low dose values stored in the actors.

	Al-Filter				Al-Cu-Filter			
	50	100	150	200	50	100	150	200
Energy [kV]	50	100	150	200	50	100	150	200
1.HVL [mm]	27	39	45	48	42	51	53	55
2.HVL [mm]	51	72	82	87	—	91	95	98
HF	0.53	0.54	0.55	0.55	—	0.56	0.56	0.56

Table 6.15: Simulated HVLs and HF's for Al- and Al-Cu-filtration modeled in GATE.

	Al-Filter in <i>SpekCalc</i>				Al-Cu-Filter in <i>SpekCalc</i>			
	50	100	150	200	50	100	150	200
Energy [kV]	50	100	150	200	50	100	150	200
1.HVL [mm]	28	39	45	48	41	53	58	58
2.HVL [mm]	53	72	84	88	73	93	101	103
HF	0.53	0.54	0.54	0.55	0.56	0.57	0.57	0.56

Table 6.16: Simulated HVLs and HF's for Al- and Al-Cu-filtration modeled in *SpekCalc*. The prefiltered spectra were used as input for GATE.

Single Al-Filter				
	50	100	150	200
Energy [kV]	50	100	150	200
1.HVL [mm]	40	54	55	55
2.HVL [mm]	—	95	97	99
HF	—	0.57	0.57	0.56

Table 6.17: Simulated HVLs and HF's for a single Al-filter modeled in GATE. Its thickness was set accordingly to table 5.2.

6.5 Lead Collimator Setup

The spot size closely after the lead collimator setup explained earlier was simulated at 150 and 200 kV. The full width half maximum (FWHM) values determined in both, horizontal and vertical direction, are shown in table 6.18 for the three different filtration methods applied to the X-ray beam and varying PMMA thickness. Figure 6.6 shows an example of the X-ray spot simulated at 200 kV with 3 mm Al and 0.5 mm Cu filtering implemented in *SpekCalc* behind 1 mm PMMA.

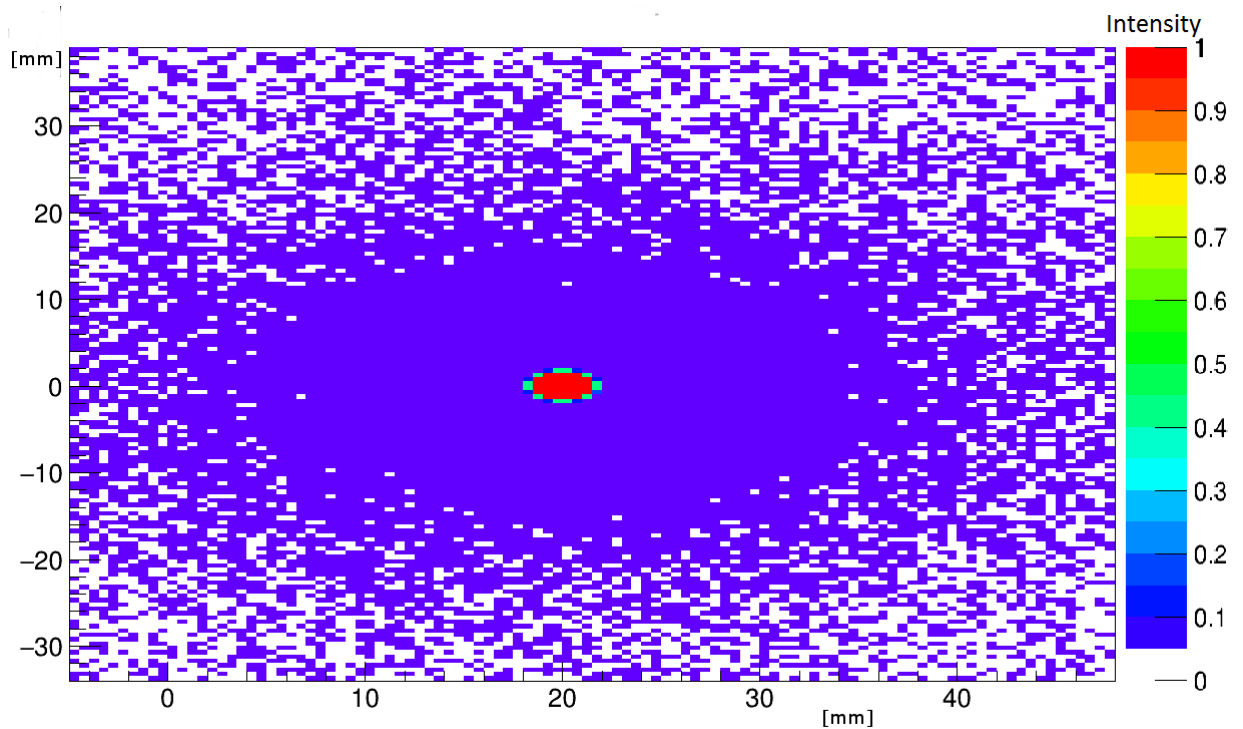


Figure 6.6: Example of the X-ray spot simulated with Al-Cu-filtration in *SpekCalc* at 200 kV tube voltage behind 1 mm PMMA.

		FWHM horizontal					FWHM vertical				
Al-Cu-Filter in GATE											
Energy [kV]	PMMA Thickness [mm]					PMMA Thickness [mm]					
	0	1	2	3	5	0	1	2	3	5	
150	3.5	3.5	4.0	3.5	3.5	3.5	3.5	4.0	3.5	3.5	
200	3.5	3.5	3.5	3.5	3.5	3.5	3.5	3.5	3.5	3.5	
Single Al-Filter in GATE											
		0	1	2	3	5	0	1	2	3	5
150	3.5	3.5	3.5	3.5	3.5	3.5	3.5	3.5	3.5	3.5	3.5
200	3.5	3.5	3.5	3.5	3.5	3.5	3.5	3.5	3.5	3.5	3.5
Al-Cu-Filter in <i>SpekCalc</i>											
		0	1	2	3	5	0	1	2	3	5
150	3.5	3.5	3.5	4.0	3.5	3.5	3.5	3.5	3.5	3.5	3.5
200	3.5	3.5	3.5	3.5	3.5	3.5	3.5	3.5	3.5	3.5	3.5

Table 6.18: FWHM values at different energies and PMMA thicknesses. The filtration thicknesses in GATE and in *SpekCalc* were set to 3 mm Al and 0.5 mm Cu, whereas for the single Al-Filter it was set accordingly to table 5.2.

6.6 Cell Irradiation Setup

For the setup describing the flask used in cell irradiation experiments, the dose distribution was stored in a three dimensional *TLEDoseActor*. Figure 6.7 shows an example of the distribution gained in the PMMA layer of the air filled flask, whereas in figure 6.8 the distribution at the PMMA-air transition. Note that the flask is placed inside a PMMA holder. The distribution in 25 mm depth inside the flask is shown in figure 6.9.

Additionally, the cross- and inplane profiles obtained from the distributions are shown in figures 6.10 and 6.11, respectively. The positions of the cross- and inplane profiles extracted from the distributions are indicated in the subsequent figures with black lines.

Figures 6.12 to 6.16 show the corresponding distributions and profiles for the flask with water filling.

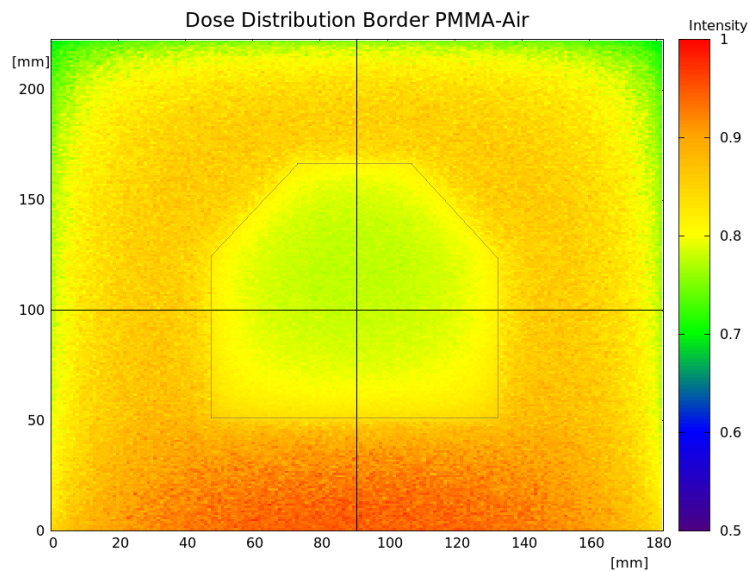


Figure 6.7: Dose distribution in the PMMA border of the flask simulated with air filling at 200 kV. Filtration was 3 mm Al and 0.5 mm Cu. The black lines indicate the positions of the cross- and inplane profiles shown in figures 6.10 and 6.11, and the grey contours outline the actual position of the flask.

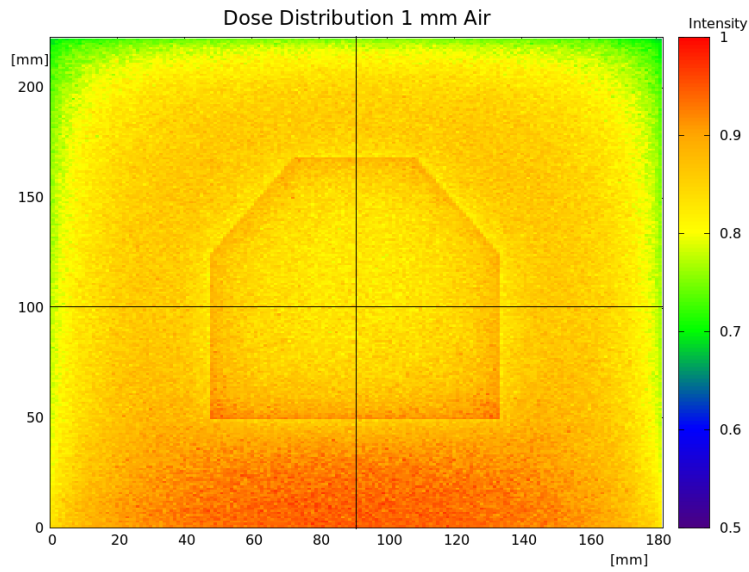


Figure 6.8: Dose distribution in air directly after the PMMA border of the flask simulated at 200 kV tube voltage. The applied filtration was 3 mm Al and 0.5 mm Cu. The black lines indicate the positions of the cross- and inplane profiles shown in figures 6.10 and 6.11.

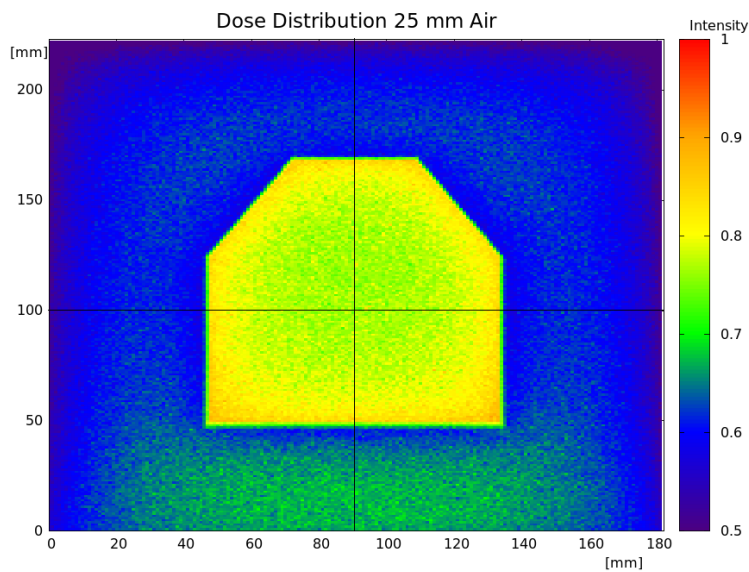


Figure 6.9: Dose distribution in 25 mm air inside the flask simulated at 200 kV tube voltage. The applied filtration was 3 mm Al and 0.5 mm Cu. The black lines indicate the positions of the cross- and inplane profiles shown in figures 6.10 and 6.11.

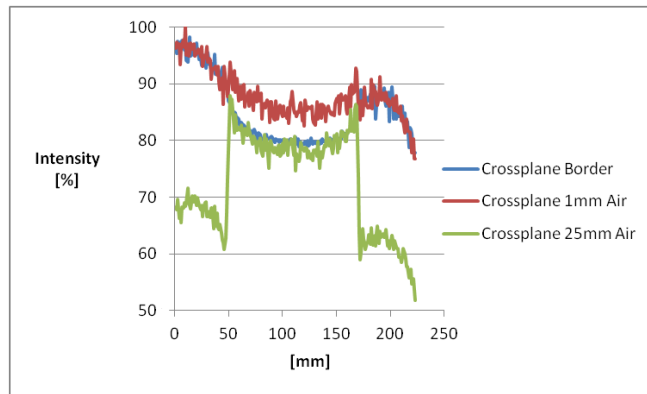


Figure 6.10: Crossplane dose profiles in the PMMA border, in air directly after the border and at 25 mm depth.

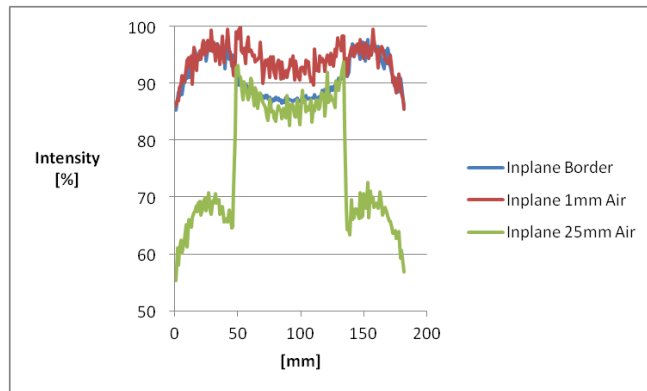


Figure 6.11: Inplane dose profiles in the PMMA border, in air directly after the border and at 25 mm depth.

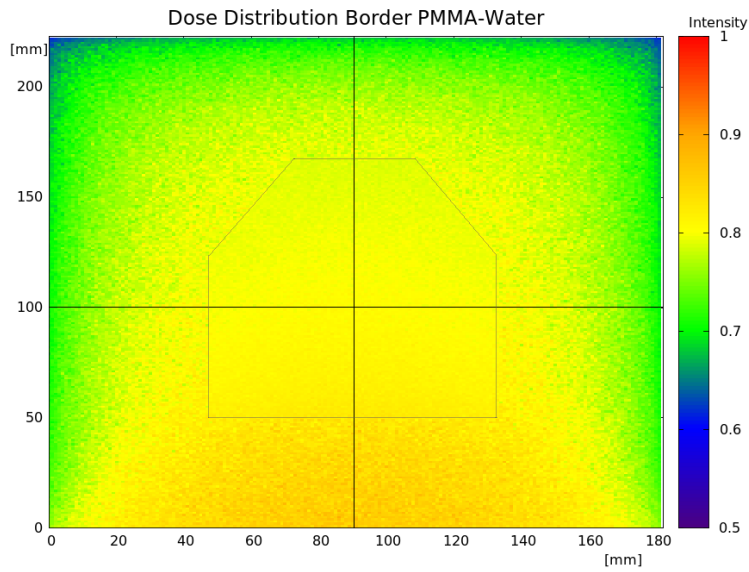


Figure 6.12: Dose distribution in the PMMA border of the flask simulated with water filling at 200 kV. Filtration was 3 mm Al and 0.5 mm Cu. The black lines indicate the positions of the cross- and inplane profiles shown in figures 6.15 and 6.16, and the grey contours outline the actual position of the flask.

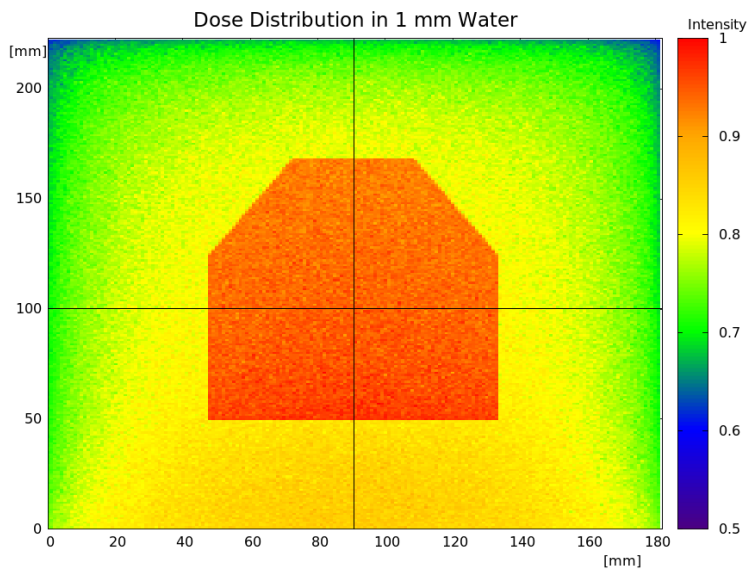


Figure 6.13: Dose distribution in water directly after the PMMA border of the flask simulated at 200 kV tube voltage. The applied filtration was 3mm Al and 0.5 mm Cu. The black lines indicate the positions of the cross- and inplane profiles shown in figures 6.15 and 6.16.

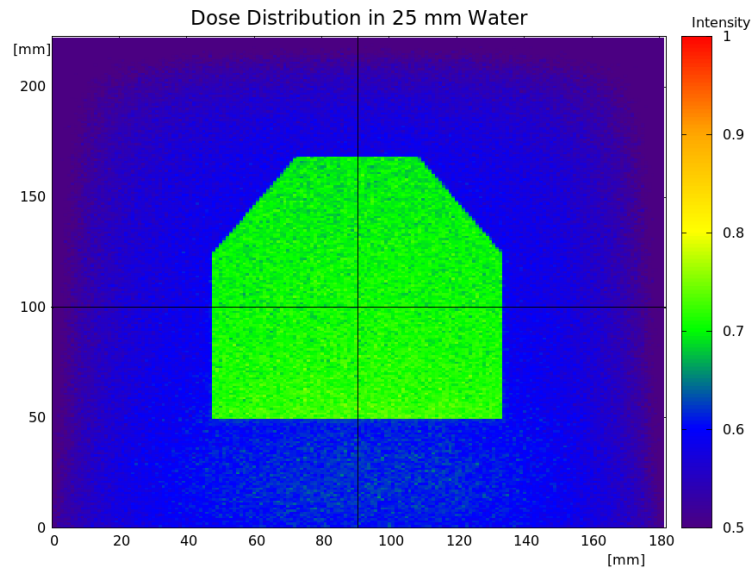


Figure 6.14: Dose distribution in 25 mm water inside the flask simulated at 200 kV tube voltage. The applied filtration was 3 mm Al and 0.5 mm Cu. The black lines indicate the positions of the cross- and inplane profiles shown in figures 6.15 and 6.16.

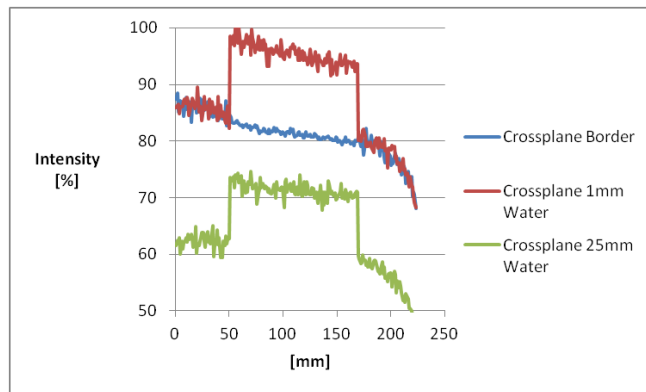


Figure 6.15: Crossplane dose profiles in the PMMA border, in water directly after the border and at 25 mm depth.

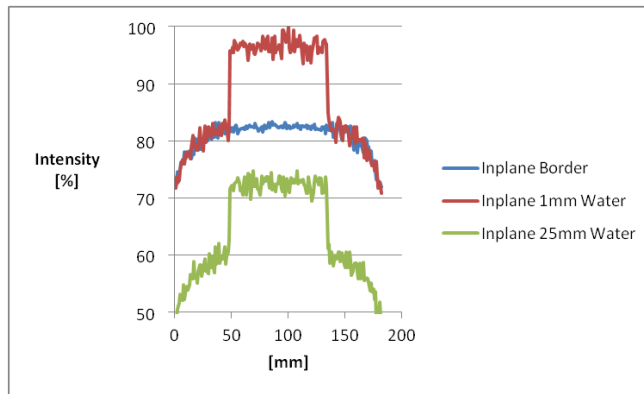


Figure 6.16: Inplane dose profiles in the PMMA border, in water directly after the border and at 25 mm depth.

7 Analysis and Discussion

7.1 Half Value Layers

In the following section the various results derived from GATE simulations are compared to measured data. The main focus is on the different settings applied in the simulations and their influence on the computational outcome. Therefore, the used physics lists and their implemented processes in GATE concerning the low kV range are investigated. Furthermore, a comparison of two different approaches to include additional X-ray beam filtering, namely modeling the filter separately in GATE and the possibility to include the filtration already in the simulation of the spectra with *SpekCalc*, is part of the evaluation and discussion, respectively.

7.1.1 Half Value Layers in Aluminium

Figure 7.1 shows a comparison of the HVLs simulated in GATE and *SpekCalc* with those obtained by measurements with the NOMEX multimeter for Al filtration. Due to the specifications of the detector no HVL could be measured for 200 kV.

The HVLs for Al-filtration computed by *SpekCalc* are in good accordance with the experimental data, though the deviations presented in table 7.1 increase with higher energies and reach up to -11.6% for 150 kV. Since the computation time of *SpekCalc* is in the range of seconds, this software provides a good and quick method to estimate half value layers in Al.

In GATE for 50 and 100 kV tube voltage an Al filter of 2.5 mm thickness yields the best matching of simulation and measurement results. At these two energies the realistic model of the Al filter with 3 mm thickness has deviations of 16.4% and 7.2% , whereas the 2.5 mm filter is below 4% deviation in both cases (see table 7.3).

Additionally, the comparison of the data shown in table 7.3 indicate that the

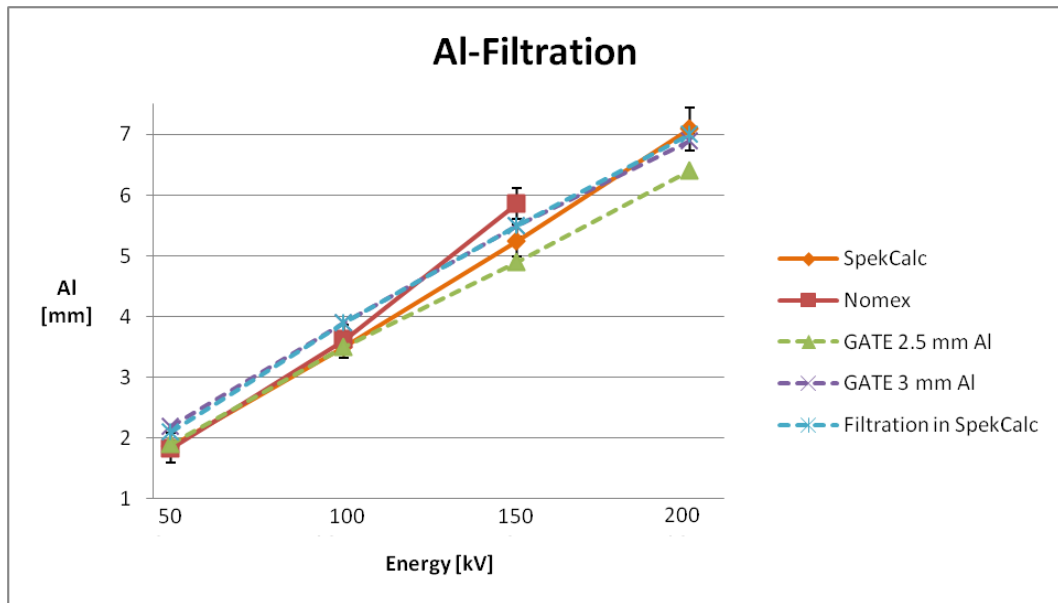


Figure 7.1: HVLs in Al at four energies with Al beam filtration. Two different filter thicknesses have been simulated in GATE. One simulation was done where the 3 mm Al filter was applied in *SpekCalc*.

inclusion of hadronic processes has no influence on the simulation data, since the results are mostly identical within some percent. This confirms the use of the *emlivermore* physics list, which is designed for modeling the electromagnetic interactions of charged particles and photons, for modeling the X-irradiator and was used in similar studies [14, 38, 39, 42].

An important conclusion can be drawn by investigating the data presented in tables 7.3 and 7.2. The simulations where the Al filter was modeled in GATE produced nearly the same results as the simulations where the filtration was done in *SpekCalc* and subsequently the simulations based on these pre-filtered spectra. For the 50 kV region the result with the filter in *SpekCalc* is even closer to the measured value than the one with the filtering in GATE. This leads to the conclusion, that the use of a pre-filtered spectrum needs less computation of interactions. Together with the fact that also less absorption of low energy photons occurs in the filter material, better statistics in the actors used to store the dose are acquired.

Deviations of <i>SpekCalc</i> to Measurements				
Filter	Al-Filter		Al-Cu-Filter	
Energy [kV]	[mm]	[%]	[mm]	[%]
50	0.03	1.6	0.11	2.5
100	-0.12	-3.4	-0.12	-1.4
150	-0.61	-11.6	-0.16	-1.4

Table 7.1: Deviations of HVLs in Al computed for different filtrations with *SpekCalc*.

Deviations of GATE with Al-Filter in <i>SpekCalc</i>				
Physics List	<i>emlivermore</i>		<i>QGSP_BERT_EMZ</i>	
Energy [kV]	[mm]	[%]	[mm]	[%]
50	0.26	12.4	0.26	12.4
100	0.28	7.2	0.28	7.2
150	-0.36	-6.6	-0.36	-6.6

Table 7.2: Deviations of HVLs in Al for simulations with GATE using the pre-filtered spectra provided by *SpekCalc*. The filtration material was 3 mm Be and 3 mm Al.

Deviations of Al-Filter in GATE to Measurements						
Al-Filter [mm]	2.5		3.0		3.5	
Energy [kV]	[mm]	[%]	[mm]	[%]	[mm]	[%]
50	0.06 (0.06)	3.2 (3.2)	0.36 (0.36)	16.4 (16.4)	0.56 (0.56)	23.3 (23.3)
100	-0.12 (-0.12)	-3.4 (-3.4)	0.28 (0.28)	7.2 (7.2)	0.68 (0.68)	15.8 (15.8)
150	-0.96 (-0.96)	-19.6 (-19.6)	-0.36 (-0.36)	-6.6 (-6.6)	0.04 (0.14)	0.7 (2.3)

Table 7.3: Deviations of HVLs in Al for simulations with GATE using different Al-filter thicknesses. The applied physics list were *emlivermore* and *QGSP_BERT_EMZ*. Results for the latter are shown using brackets.

In case of Al and Cu filtration, the measurement and simulation results presented in figure 7.2 were derived. Note that for 200 kV the NOMEX detector could not provide a result for the HVL.

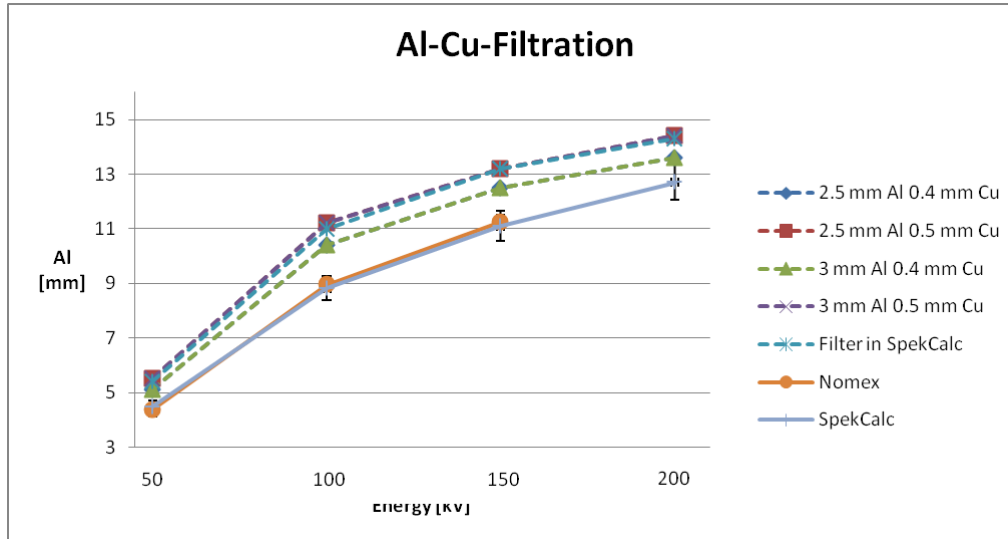


Figure 7.2: HVLs in Al at four energies with Al-Cu beam filtration. Several different filter thicknesses have been simulated in GATE. One simulation was done where the 3 mm Al and 0.5 mm Cu filtration was applied in *SpekCalc*.

Figure 7.2 and table 7.1 indicate that the algorithm for computing the HVL implemented in *SpekCalc* provides a proper estimation for the beam filtration effects of Al and Cu. The deviations for the calculated HVLs are below 3 % for the analyzed energies, except for Al filtration at 150 kV where it is -11.6% . These results confirm the reported accuracy of *SpekCalc* by Suk et al. and Kuess et al., who stated that the HVL estimations of the program show maximum discrepancies of 10 % and 9 %, respectively [43, 44]. Poludniowski et al. reported a difference of 3 % between *SpekCalc* and measurements [34].

For the GATE simulations in figure 7.2, as well as results in table 7.6, show that the thickness of the Al filter has practically no effect on the HVLs. This is in contrast to the influences of the Cu thickness. The filter combinations with 0.4 mm Cu produce HVLs which are closer to the experimental data than the ones with 0.5 mm Cu. Additionally, for 0.4 mm Cu the calculated HVLs for 2.5 mm

Deviations of GATE with Al-Cu-Filter in <i>SpekCalc</i> to Measurements		
Energy [kV]	[mm]	[%]
50	1.04 (1.04)	19.3 (19.3)
100	2.05 (2.05)	18.6 (18.6)
150	1.94 (1.94)	14.7 (14.7)

Table 7.4: Deviations of HVLs in Al for simulations with GATE using two physics lists, *emlivermore* and *QGSP_BERT_EMZ*, with the results for the latter being shown in brackets. The filtration of 3 mm Be, 3 mm Al and 0.5 mm Cu was already included in *SpekCalc*.

and 3 mm Al are virtually identical within some percent. The same holds for the data with 0.5 mm Cu. The reason for these effects are the absorption properties of the materials. Copper absorbs the low energy photons, yielding a harder X-ray beam and also removing the so-called Heel effect. Aluminium also absorbs in the low energy range, but due to its lower density mostly below 20 kV (see figure 2.14), leading to less influence on the beam hardness than Cu.

Furthermore, the application of the filter materials in *SpekCalc* yields HVLs that are close to the ones obtained by simulating the filtration with GATE, as can be seen in figure 7.2. The data presented in tables 7.4 and 7.6 also indicate that the use of *SpekCalc* leads to slightly better results, since there are less deviations. This leads to the conclusion that the implementation of the different beam filters in the software *SpekCalc* improves the computational time needed as well as the resulting statistics obtained in the simulations, since more particles are stored in the dose actors.

Implementation of a single Al filter leads to slightly better matching HVLs than the approach of the pre-filtration in *SpekCalc*, as can be seen by comparing tables 7.4 and 7.5, although even with this setup deviations up to almost 18 % occur. In addition, substituting the three different filters with such a thick, single filter leads to other problems concerning the computational time, since absorption of a lot of photons results in the need to simulate even higher particle numbers than done in this investigation. Besides this, the loss of particles leads to decreased statistics and the results suffer from less significance. Therefore, the use of a single Al filter

is not really an alternative for the implementation of the beam filtration in the GATE simulations.

Deviations of a single Al-Filter in GATE to Measurements		
Energy [kV]	[mm]	[%]
50	0.94 (0.94)	17.7 (17.7)
100	1.85 (1.85)	17.1 (17.1)
150	1.64 (1.64)	12.7 (12.7)

Table 7.5: Deviations of HVLs in Al. As filtration a single Al-filter was applied in GATE with its thickness corresponding to table 5.2. Two physics lists were used, *emlivermore* and *QGSP_BERT_EMZ*. Results for the latter are shown in brackets.

Finally, it can be stated that the deviations shown in table 7.6 suggest that the best results for HVLs in Al can be achieved by reducing the filter thicknesses. This assumption is quite problematic, since a Monte Carlo based simulation is intended to reproduce a realistic behaviour of interactions, and therefore all properties should be modeled as accurate as possible. Following this code of practice when interpreting the results it can be concluded that the interactions at the kV energy range as implemented in the *emlivermore* and *QGSP_BERT_EMZ* physics lists are not very accurate at this energy regime. Most results presented in this thesis prove that the deviations of both physics lists are within the range of some percent. Due to this and the fact that hadronic processes can be omitted at the investigated energies, the choice was made to use the *emlivermore* physics list for simulating the experimental setups. An advantage of this list is that it is especially designed to model electromagnetic interactions yielding better computational performance for simulating an X-ray beam in the low keV range.

Deviations of Al-Cu-Filter in GATE to Measurements						
Al-Filter [mm]			2.5			
Cu-Filter [mm]	0.4		0.5		0.6	
Energy [kV]	[mm]	[%]	[mm]	[%]	[mm]	[%]
50	0.74 (0.64)	14.5 (12.8)	1.04 (1.04)	19.3 (19.3)	1.34 (1.34)	23.5 (23.5)
100	1.25 (1.15)	12.3 (11.4)	2.15 (2.15)	19.4 (19.4)	2.65 (2.65)	22.9 (22.9)
150	1.04 (1.04)	8.5 (8.5)	1.84 (2.14)	14.1 (16.0)	2.54 (2.54)	18.4 (18.4)
Al-Filter [mm]			3.0			
Cu-Filter [mm]	0.4		0.5		0.6	
Energy [kV]	[mm]	[%]	[mm]	[%]	[mm]	[%]
50	0.74 (0.74)	14.5 (14.5)	1.14 (1.04)	20.7 (19.3)	1.44 (1.34)	24.8 (23.5)
100	1.45 (1.45)	13.9 (13.9)	2.25 (2.15)	20.1 (19.4)	2.75 (2.75)	23.5 (23.5)
150	1.24 (1.54)	9.9 (12.0)	1.94 (1.94)	14.7 (14.7)	2.54 (2.54)	18.4 (18.4)
Al-Filter [mm]			3.5			
Cu-Filter [mm]	0.4		0.5		0.6	
Energy [kV]	[mm]	[%]	[mm]	[%]	[mm]	[%]
50	0.84 (0.84)	16.2 (16.2)	1.14 (1.14)	20.7 (20.7)	1.34 (1.34)	23.5 (23.5)
100	1.55 (1.55)	14.8 (14.8)	2.25 (2.15)	20.1 (19.4)	2.45 (2.55)	21.5 (22.2)
150	1.24 (1.34)	9.9 (10.6)	1.94 (1.94)	14.7 (14.7)	2.34 (2.34)	17.2 (17.2)

Table 7.6: Deviations of HVLs in AL with *emlivermore* and *QGSP_BERT_EMZ* physics list at different Al-Cu-filter thicknesses. Results for the *QGSP_BERT_EMZ* physics list are shown in brackets.

7.1.2 Intensity Variation in Air

For the 50 % intensity drop in the Perspex tank the data presented in figure 7.3 were obtained by measurements and simulations. For the measurements an uncertainty of $\pm 5\%$ was observed, resulting in the rather large error bars. The corresponding data for the 75 % drop are shown in figure 7.4.

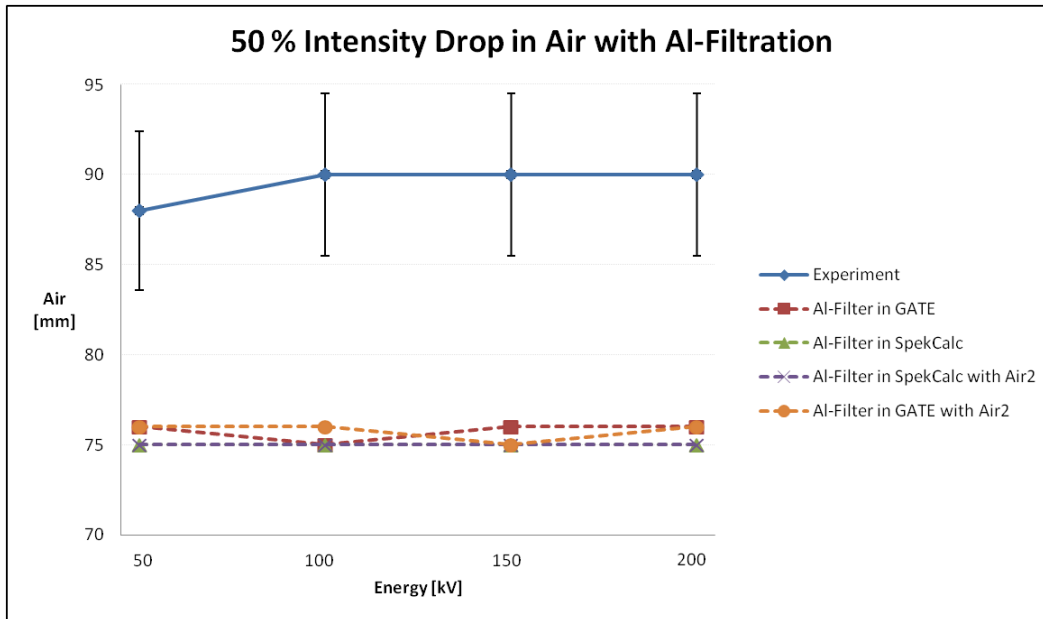


Figure 7.3: 50 % intensity drops for different energies measured inside the Perspex tank compared to simulation data. The applied filtration was 3 mm Al. Simulations were done with realistic filter thicknesses in GATE and *SpekCalc* and two different material models of air were investigated.

The simulation results achieved with the Al filter modeled in GATE show deviations reaching up to -20.0% for the 50 % and -20.9% for the 75 % drop, as shown in table 7.7. Using the GATE material *Air2*, with twice the density of the *Air* material, has nearly no effect on the resulting intensity drops. Applying the filtration in *SpekCalc* and simulating the setup in GATE with the pre-filtered spectra leads to even slightly worse results (see table 7.8). This might be explained by the fact that the interactions of the photons propagating through any of the air materials is not computed in a correct way.

Figure 7.5 shows the 50 % intensity drop in the Perspex tank gained with Al-Cu

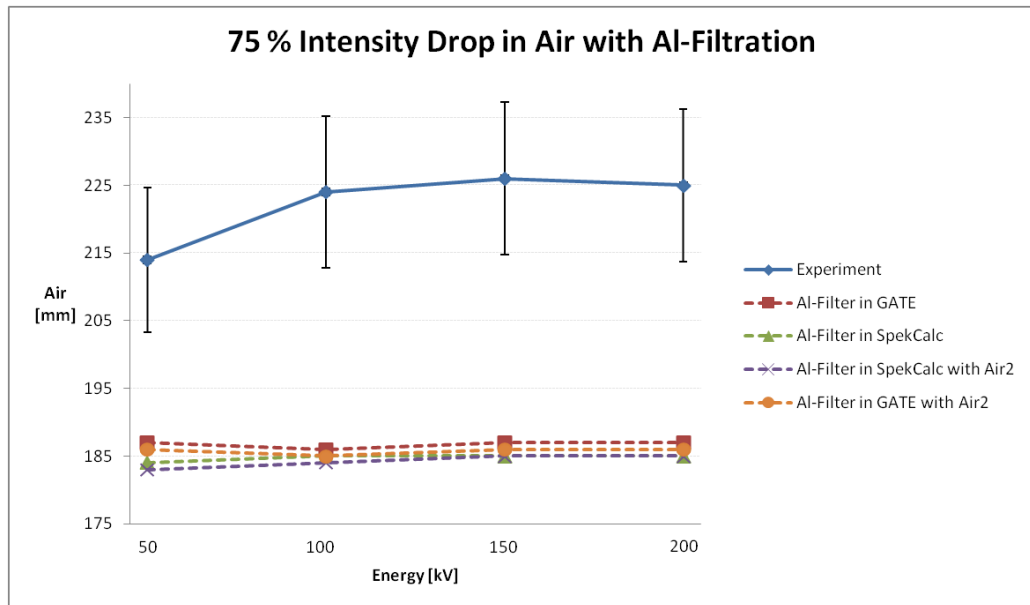


Figure 7.4: 75 % intensity drops for different energies measured inside the Perspex tank compared to simulation data. The applied filtration was 3 mm Al. Simulations were done with realistic filter thicknesses in GATE and *SpekCalc* and two different material models of air were investigated.

filtration of the X-ray beam. The experimental value for 50 kV seems to be not very reliable, due to the low absolute dose produced at 50 kV. Furthermore, the semi-flexible ionization chamber type 31010 from PTW is calibrated for application in an energy range from 66 kV to 50 MeV making a reasonable comparison rather challenging [30]. The data for the 75 % drop are presented in figure 7.6, where the experimental value for the 50 kV measurement is also questionable.

Table 7.9 presents the deviations of the simulated drops with filtration thicknesses of 3 mm Al and 0.5 Cu. At 50 kV the computed doses were too low to determine useful results. Comparison of these two tables yields that for *Air2* the variations computed have slightly increased deviations. Applying the filtration in *SpekCalc* does not improve the quality of the intensity drops simulated with GATE (see table 7.10). On the contrary, the deviations with the pre-filtered spectra reach even up to -27.0% . Replacing the filter combination with a single Al-filter produces the deviations shown in table 7.11, which are of the same order as the deviations gained by the simulations with the realistic filtration thicknesses.

Deviations of Al-Filter in GATE to Measurements				
Energy [kV]	50 % Drop		75 % Drop	
	[mm]	[%]	[mm]	[%]
50	-12 (-12)	-15.8 (-15.8)	-27 (-27)	-14.4 (-14.4)
100	-15 (-14)	-20.0 (-18.4)	-38 (-36)	-20.4 (-19.2)
150	-14 (-15)	-18.4 (-20.0)	-39 (-40)	-20.9 (-21.5)
200	-14 (-14)	-18.4 (-18.4)	-38 (-39)	-20.3 (-21.0)

Table 7.7: Intensity drop deviations for Al filtration at different energies as computed with GATE for *Air* and *Air2*. Results for *Air2* are shown in brackets. The filter thickness was 3 mm Al.

Deviations of GATE with Al-Filter in <i>SpekCalc</i> to Measurements				
Energy [kV]	50 % Drop		75 % Drop	
	[mm]	[%]	[mm]	[%]
50	-13 (-13)	-17.3 (-17.3)	-29 (-31)	-15.7 (-16.9)
100	-15 (-15)	-20.0 (-20.0)	-39 (-40)	-21.1 (-21.7)
150	-15 (-15)	-20.0 (-20.0)	-41 (-41)	-22.2 (-22.2)
200	-15 (-15)	-20.0 (-20.0)	-40 (-40)	-21.6 (-21.6)

Table 7.8: Computed deviations of the intensity drops at different energies with *Air* and *Air2*. Results for *Air2* are shown using brackets. The 3 mm Al filter was included in *SpekCalc*.

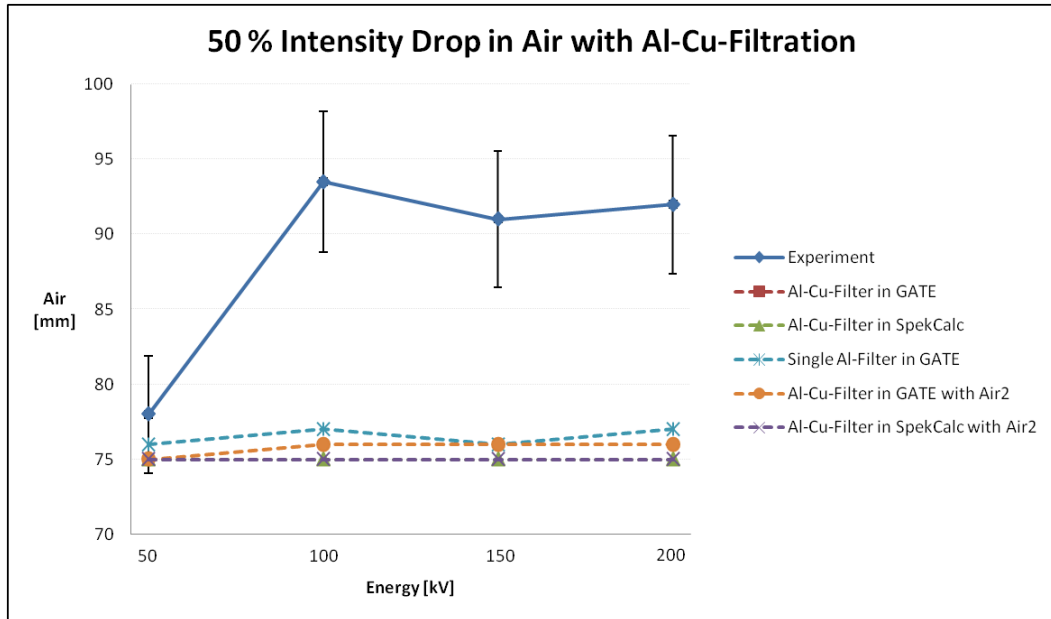


Figure 7.5: 50 % intensity drops for different energies measured inside the Perspex tank compared to simulation data. The applied filtration was 3 mm Al and 0.5 mm Cu. Simulations were done with realistic filter thicknesses in GATE and *SpekCalc*. Also two different material models of air were used.

Deviations of Al-Cu-Filter in GATE to Measurements				
Energy [kV]	50 % Drop		75 % Drop	
	[mm]	[%]	[mm]	[%]
100	-17 (-18)	-22.1 (-23.7)	-46 (-47)	-24.3 (-25.0)
150	-15 (-15)	-19.7 (-19.7)	-41 (-42)	-21.9 (-22.6)
200	-16 (-16)	-21.1 (-21.1)	-45 (-45)	-24.2 (-24.2)

Table 7.9: Intensity drop deviations for Al-Cu-filtration at different energies as computed with GATE. The filter thicknesses were 3 mm Al and 0.5 mm Cu. Simulations were conducted with *Air* and *Air2*, with the results for the latter shown in brackets.

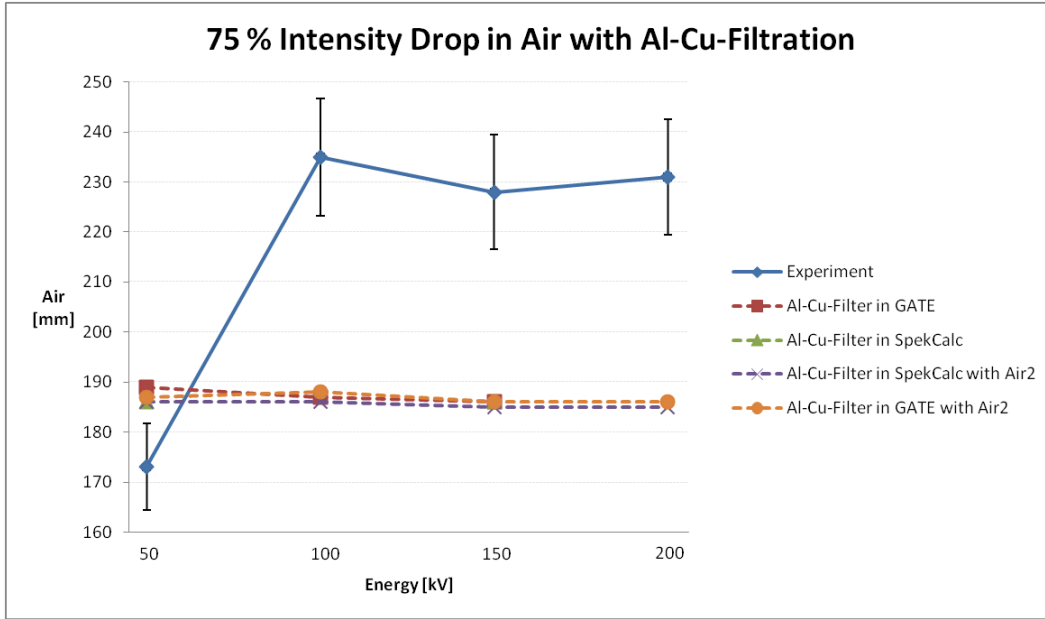


Figure 7.6: 75 % intensity drops for different energies measured inside the Perspex tank compared to simulation data. The applied filtration was 3 mm Al and 0.5 mm Cu. Simulations were done with realistic filter thicknesses in GATE and *SpekCalc*. Also two different material models of air were used.

Deviations of GATE with Al-Cu-Filter in <i>SpekCalc</i> to Measurements				
Energy [kV]	50 % Drop		75 % Drop	
	[mm]	[%]	[mm]	[%]
50	-3 (-3)	-4.0 (-4.0)	12 (13)	6.5 (7.0)
100	-19 (-19)	-25.3 (-25.3)	-50 (-49)	-27.0 (-26.3)
150	-16 (-16)	-21.3 (-21.3)	-43 (-43)	-23.2 (-23.2)
200	-17 (-17)	-22.7 (-22.7)	-46 (-46)	-24.9 (-24.9)

Table 7.10: Computed deviations of the intensity drops at different energies. The 3 mm Al filter and 0.5 mm Cu were included in *SpekCalc*. Simulations were conducted using *Air* and *Air2*, with the results for the latter shown in brackets.

Deviations of a single Al-Filter in GATE to Measurements				
Energy [kV]	50 % Drop		75 % Drop	
	[mm]	[%]	[mm]	[%]
50	-2	-2.6	13	7.0
100	-17	-22.1	-46	-24.3
150	-15	-19.7	-41	-21.9
200	-15	-19.5	-44	-23.5

Table 7.11: Deviations of intensity drops in air at different energies. As filtration a single Al-filter was applied in GATE with its thickness corresponding to table 5.2.

The data shown in this section indicate that it makes no particular difference if the air is modeled using *Air* or *Air2*. In addition, it can be seen that for the case of Al-Cu filtration, the implementation of the filtering in *SpekCalc* yields slightly worse results than the case of filter modeling in GATE. These results are contrary to those obtained for the simulations where only Al was applied as additional filtration. By using a single Al filter replacing the Be-Al-Cu combination the results for the intensity variations are better and within the range of ± 3 %. Due to the reasons also mentioned afore in section 7.1.1, particle loss and increased computational time, the use of this method is a rather unsuitable solution for describing the filtering effects.

Furthermore, it is speculated, that the interaction of photons in the kV range in air, as implemented in the *elivermore* physics list, follows quite inaccurate mathematical models. This is also backed up by the fact, that even for the filtration being considered in *SpekCalc*, the accuracy is decreasing. It is also worth mentioning, that using a detector which is build for this specific low energy range could alter the measurement data, especially for the experiments conducted at 50 kV tube voltage.

7.1.3 Half Value Layers in PMMA

For the experiments and simulations regarding the HVLs in PMMA, the data shown in figures 7.7 and 7.8 were obtained for Al and Al-Cu filtration, respectively. Regarding the experimental data for Al-filtration the second HVL at 200 kV seems to be somewhat out of range. The same holds for the 50 kV measurement with Al-Cu filtration, but here the limited energy range of the semi-flexible ionization chamber has to be taken into account.

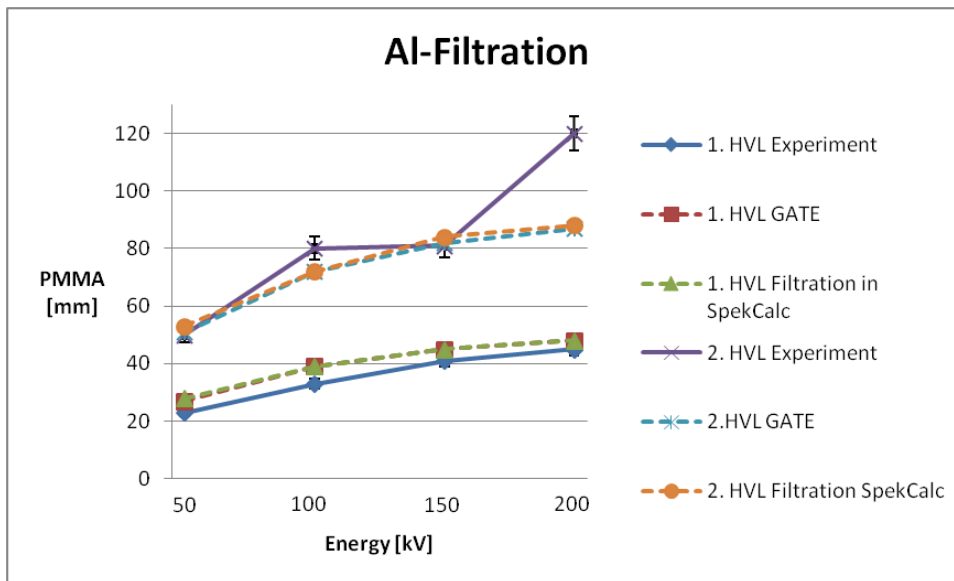


Figure 7.7: Measured HVLs in PMMA for different energies compared to simulation data. The applied filtration was 3 mm Al. Simulations were done with realistic filter thicknesses modeled in GATE and with the filtration already included *SpekCalc*.

Table 7.12 contains the absolute and relative deviations for the filtering simulated in GATE. The accuracy of the 1. HVLs increases with energy and reaches its best of 6.4 % at 200 kV. For the 2. HVLs the results at 50 and 150 kV are very close to the experimental data, whereas the deviation at 100 is 11.1 %. Taking into account that the measurement data for the 2. HVL at 200 kV is rather questionable, the deviation of -37.9% can not be compared reliably.

If the filtration is already applied in *SpekCalc*, the results change only slightly, as shown in table 7.13 and figure 7.7. Again the accuracy for the first HVL

Deviations of Al-Filter in GATE to Measurements				
Energy [kV]	1. HVL		2. HVL	
	[mm]	[%]	[mm]	[%]
50	0.4	14.8	0.1	2.0
100	0.6	15.4	-0.8	-11.1
150	0.4	8.9	0.1	1.2
200	0.3	6.3	-3.3	-37.9

Table 7.12: Deviations for the HVLs in PMMA at different energies. The 3 mm Al filtration was modeled in the GATE simulations.

increases with the applied tube voltage, although the deviation at 50 kV is about 2% higher than for the GATE modeling of the filtration. For the second HVLs the deviation differs about 2.7 and 2.5% at 50 and 150 kV, respectively. For 200 kV tube voltage the results for the second HVL are again questionable, due to inadequate measurement data. This supports the approach of using the beam filtering possibilities provided by *SpekCalc* and the application of the pre-filtered spectra as GATE input, although some deviations for this method are higher. This disadvantages are outweighed by a decrease in computational time and better statistics for the output.

Deviations of GATE with Al-Filter in <i>SpekCalc</i> to Measurements				
Energy [kV]	1. HVL		2. HVL	
	[mm]	[%]	[mm]	[%]
50	0.5	17.9	0.3	5.7
100	0.6	15.4	-0.8	-11.1
150	0.4	8.9	0.3	3.6
200	0.3	6.3	-3.2	-36.4

Table 7.13: Deviations for the HVLs in PMMA at different energies. The 3 mm Al filtration was included in *SpekCalc* and the simulations performed with the pre-filtered spectra.

In figure 7.8 the measured data for the 1. HVLs in PMMA for Al-Cu filtration are shown along with the simulation results. Due to too low dose the second HVL could not be measured. Particularly striking is the experimental value obtained at 50 kV. As mentioned before in section 7.1.2 the used detector (semi-flexible ionization chamber type 31010 from PTW) has its lower energy range limit at 66 kV. Together with the low absolute doses occurring at only 50 kV voltage the rather inadequate result shown is produced.

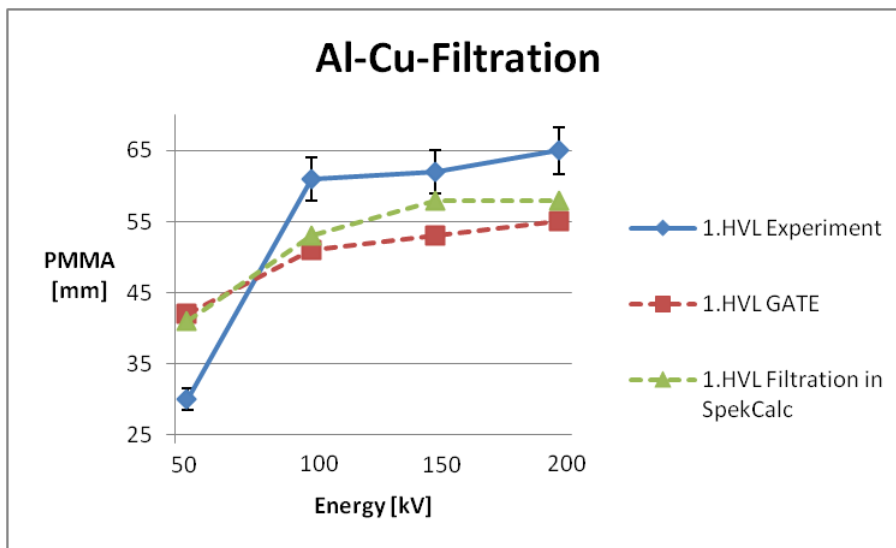


Figure 7.8: Measured HVLs in PMMA for different energies compared to simulation data. The applied filtration was 3 mm Al and 0.5 mm Cu. Simulations were done with realistic filter thicknesses modeled in GATE and with the filtration already included in *SpekCalc*.

The deviations of the simulations are listed in table 7.14. If the 50 kV results are excluded, the remaining deviations are all of the same order, with the maximum being -19.6% .

For the filtration done in *SpekCalc* the resulting HVLs have a better accuracy than the ones with the filtration included in GATE (see table 7.15). If ignoring the incomparable 50 kV data the deviations decrease with higher energy, which is in good accordance to the data for the Al filtration. The maximum deviation for Al-Cu filtration of -15.1% is observed at 100 kV. This supports the earlier mentioned conclusion that the use of *SpekCalc* to include the different filtration materials,

Deviations of Al-Cu-Filter in GATE to Measurements		
Energy [kV]	[mm]	[%]
50	1.2	28.6
100	-1.0	-19.6
150	-0.9	-17.0
200	-1.0	-18.2

Table 7.14: Deviations for the HVLs in PMMA at different energies. The 3 mm Al and 0.5 mm Cu filtration were modeled in the GATE simulations.

Deviations of GATE with Al-Cu-Filter in <i>SpekCalc</i> to Measurements		
Energy [kV]	[mm]	[%]
50	1.1	26.8
100	-0.8	-15.1
150	-0.4	-6.9
200	-0.7	-12.1

Table 7.15: Deviations for the HVLs in PMMA at different energies. The 3 mm Al and 0.5 filtration were included in *SpekCalc* and the simulations performed with the pre-filtered spectra.

yields not only better results, but also increases the statistics in the simulations, since less particles are absorbed in the filters. Additionally, the computation of the interactions between photons and filters can be omitted, resulting in reduced computation time.

By replacing the three different filter materials with a single Al filter the deviations presented in table 7.16 were obtained. Omitting the 50 kV data, the accuracy of the HVLs at 100 and 150 is better than for the other two methods, but the deviation reaches its maximum value of -18.2% at 200 kV. Again, the principle of building an accurate geometrical setup to use in the Monte Carlo calculations and the problems of particle loss and scattering, are arguments which do not support the use of such a thick filter consisting only of one material and omitting Be and Cu.

Deviations of a single Al-Filter in GATE to Measurements		
Energy [kV]	[mm]	[%]
50	1.0	25.0
100	-0.7	-13.0
150	-0.7	-12.7
200	-1.0	-18.2

Table 7.16: Deviations for the HVLs in PMMA at different energies. The filtration was done with a single Al filter replacing the Be-Al-C combination. Its thickness was set following the values from table 5.2.

Interestingly the simulated first HVLs for Al-filtering are all greater than the measured ones. Exactly the opposite is observable for Al-Cu filtering, except at 50 kV, which is explainable with inadequate measurements. This results could lead to the conclusion that the density of the materials has a bigger influence on the implemented interactions between photons and matter than it should have, since Cu has more than three times the density of Al and the photon-matter interactions depend on it (see section 2.1.1). This also proves that the implemented mathematical models in the *emlivermore* physics list have room for improvement regarding the low kV energy range.

7.2 Cross- and Inplane Profiles

In figures 7.9 - 7.24 the measured cross- and inplane profiles at different energies for both, additional Al and Al-Cu filtering, are compared to their corresponding profiles obtained by the simulations. Additional filtration was already included in *SpekCalc* for simulating the input spectra used in GATE. The field size was defined as the area above 60 % intensity. The reason for this definition is, that by using the 60 % limit, the best matching for the beam shape between measurements and simulations could be obtained.

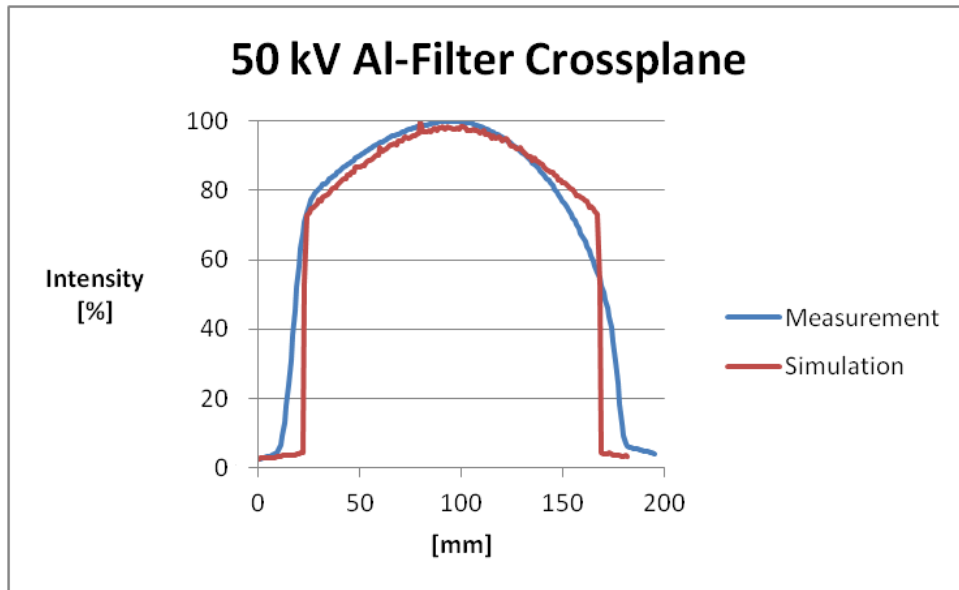


Figure 7.9: Comparison between measured and simulated crossplane profile at 50 kV. Applied filtration was 3 mm Al.

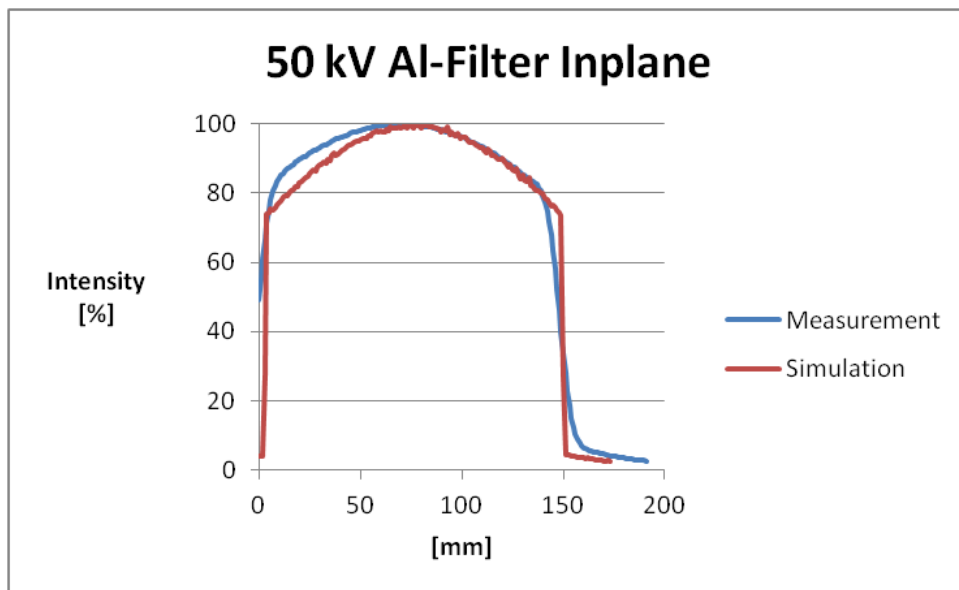


Figure 7.10: Comparison between measured and simulated inplane profile at 50 kV. Applied filtration was 3 mm Al.

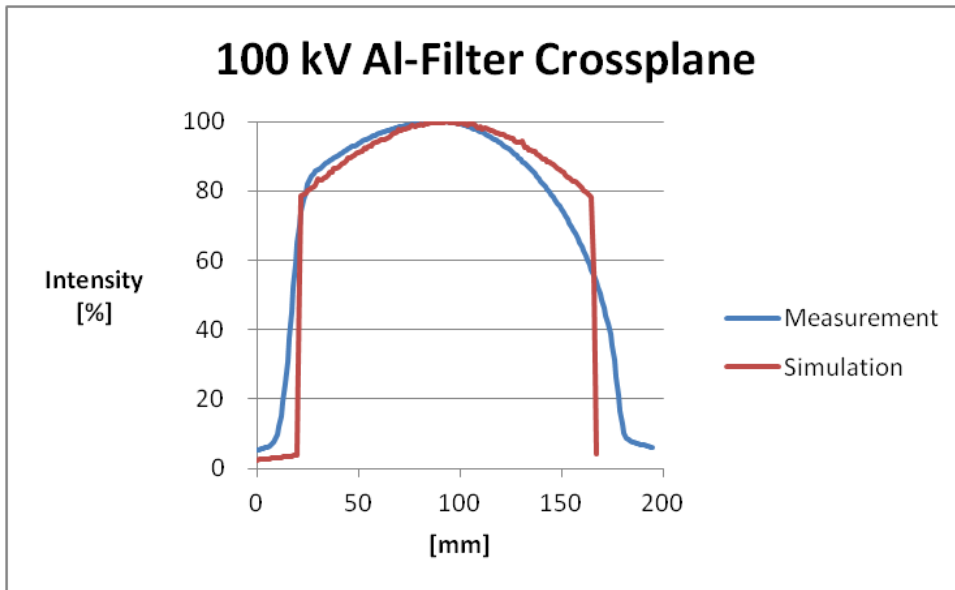


Figure 7.11: Comparison between measured and simulated crossplane profile at 100 kV. Applied filtration was 3 mm Al.

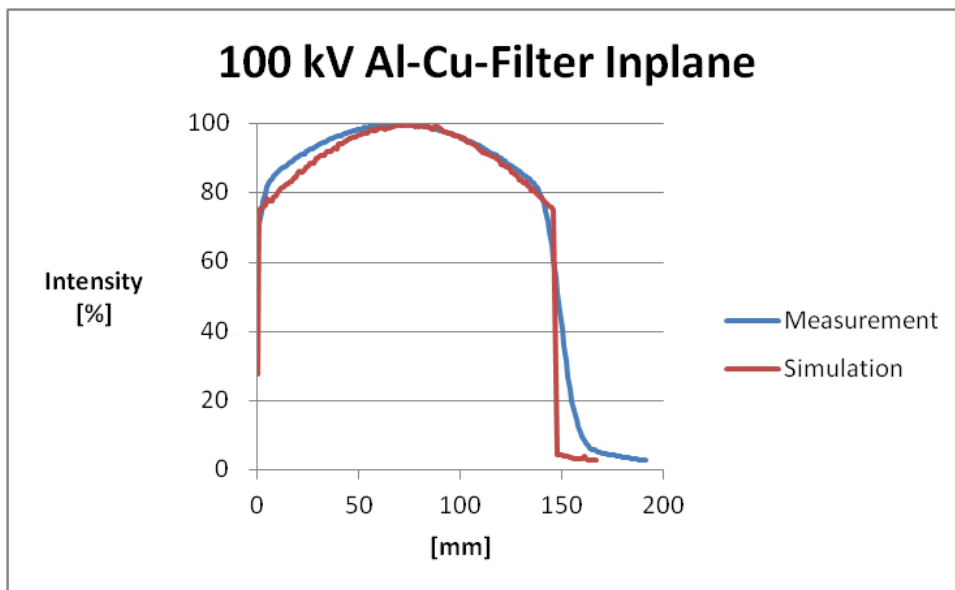


Figure 7.12: Comparison between measured and simulated inplane profile at 100 kV. Applied filtration was 3 mm Al.

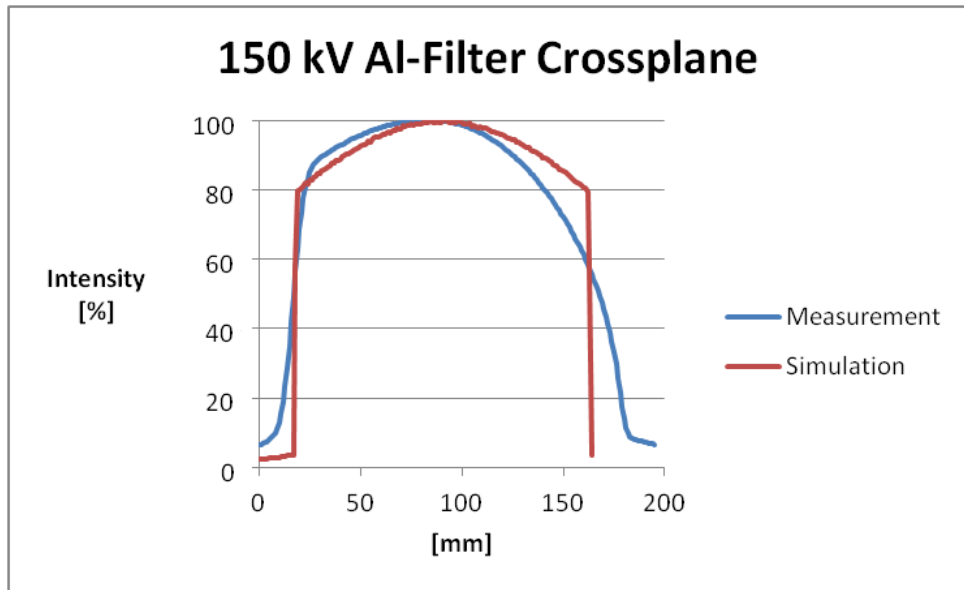


Figure 7.13: Comparison between measured and simulated crossplane profile at 150 kV. Applied filtration was 3 mm Al.

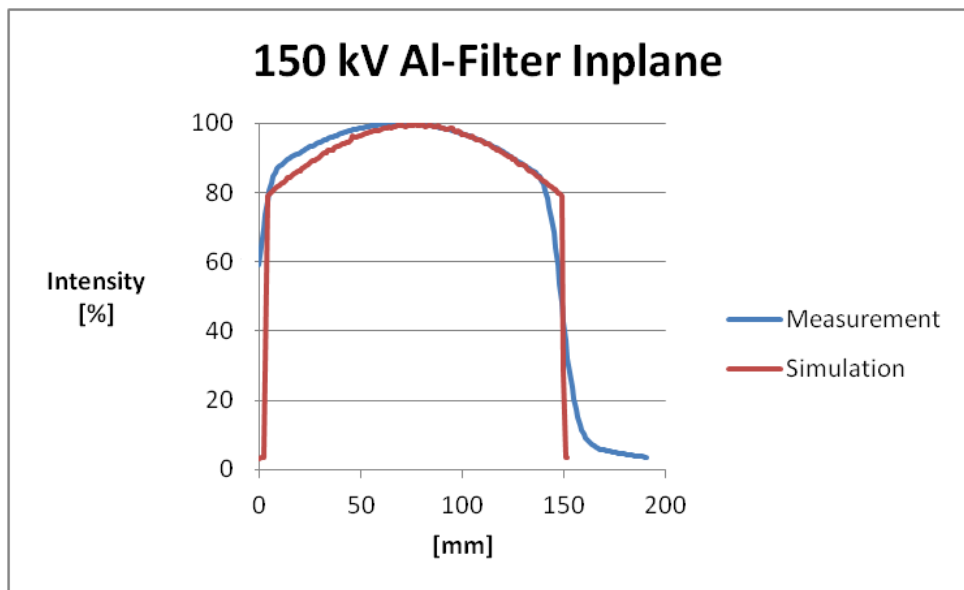


Figure 7.14: Comparison between measured and simulated inplane profile at 150 kV. Applied filtration was 3 mm Al.

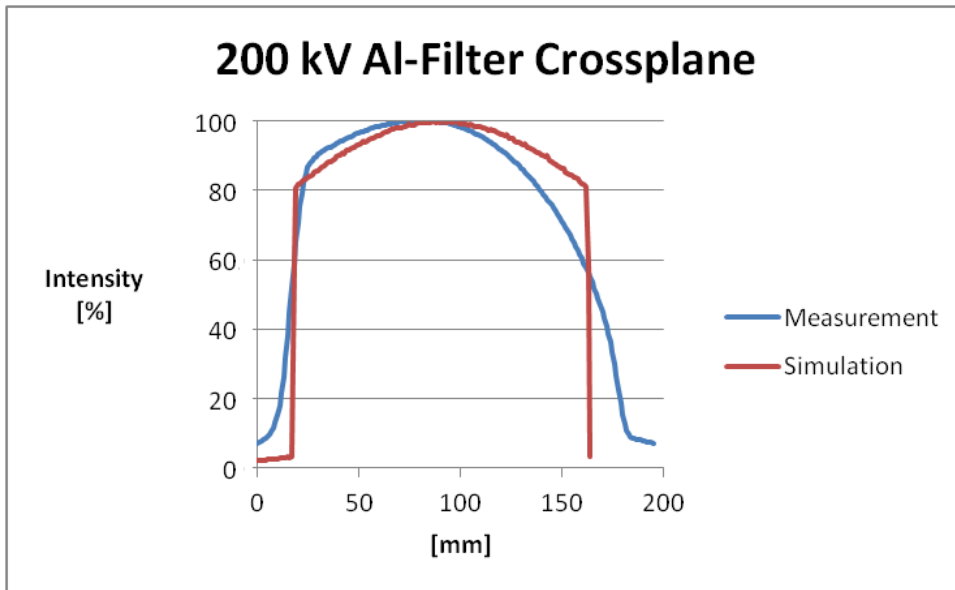


Figure 7.15: Comparison between measured and simulated crossplane profile at 200 kV. Applied filtration was 3 mm Al.

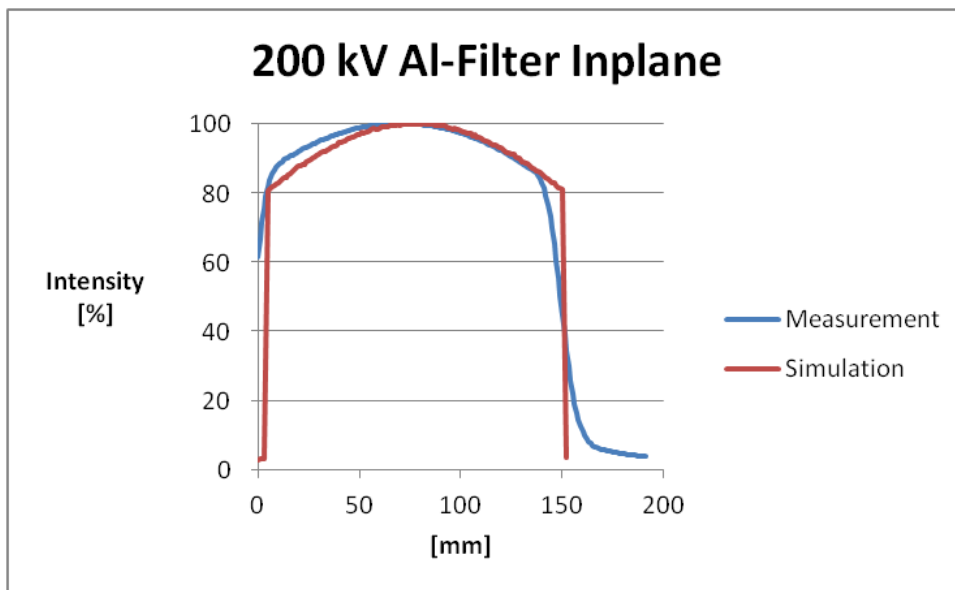


Figure 7.16: Comparison between measured and simulated inplane profile at 200 kV. Applied filtration was 3 mm Al.

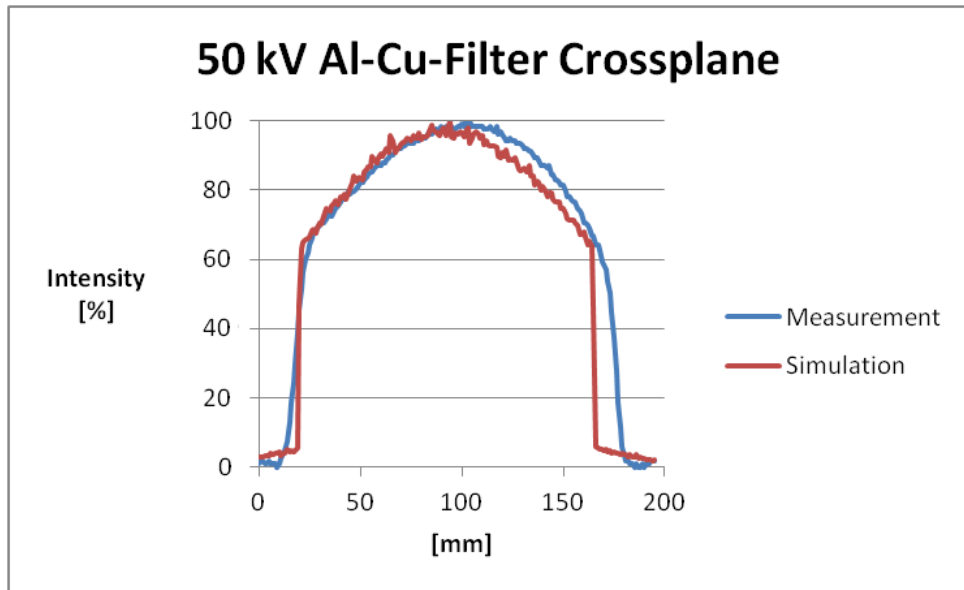


Figure 7.17: Comparison between measured and simulated crossplane profile at 50 kV. Applied filtration was 3 mm Al and 0.5 mm Cu.

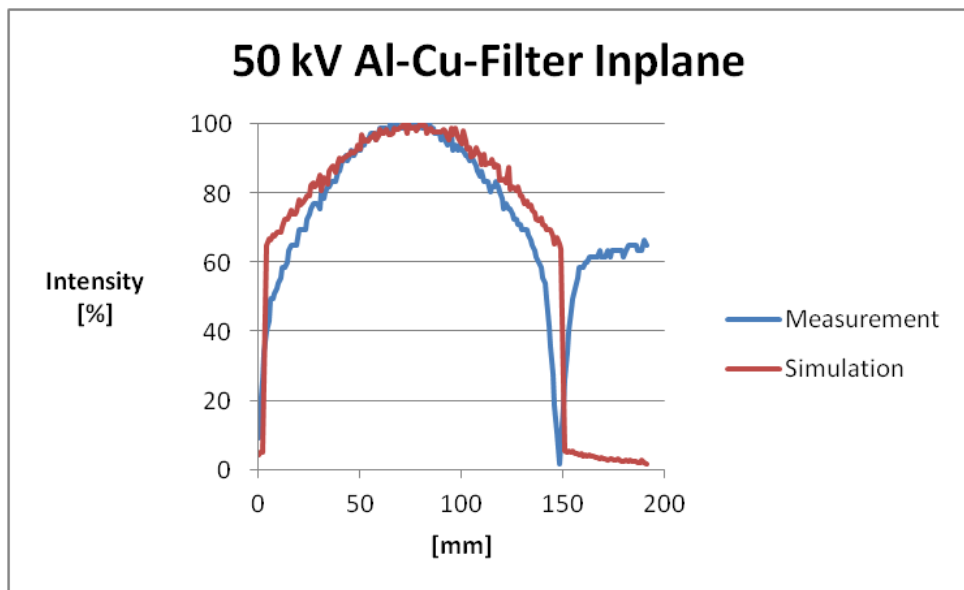


Figure 7.18: Comparison between measured and simulated inplane profile at 50 kV. Applied filtration was 3 mm Al and 0.5 mm Cu. Scattering effects are the reason for the measured dose increase after around 150 mm.

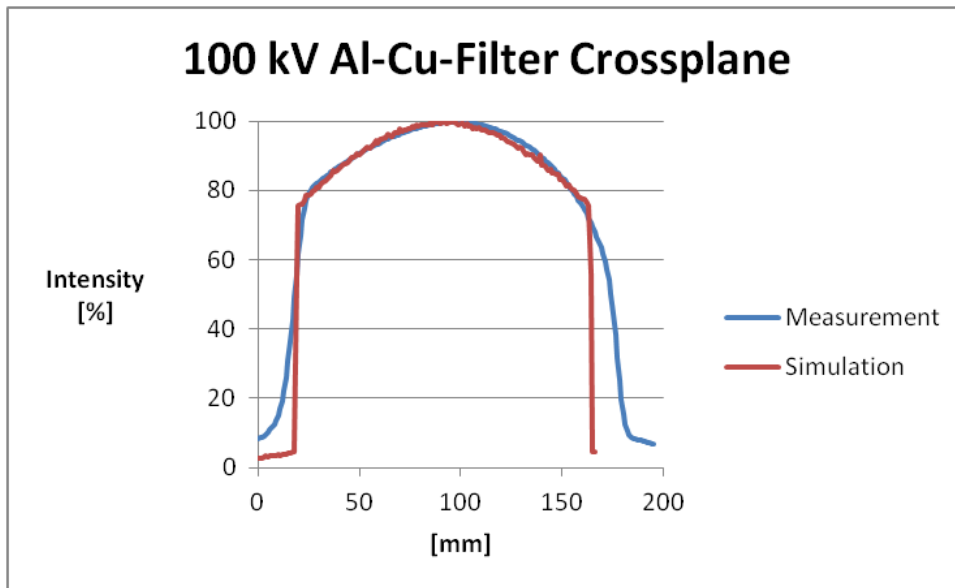


Figure 7.19: Comparison between measured and simulated crossplane profile at 100 kV. Applied filtration was 3 mm Al and 0.5 mm Cu.

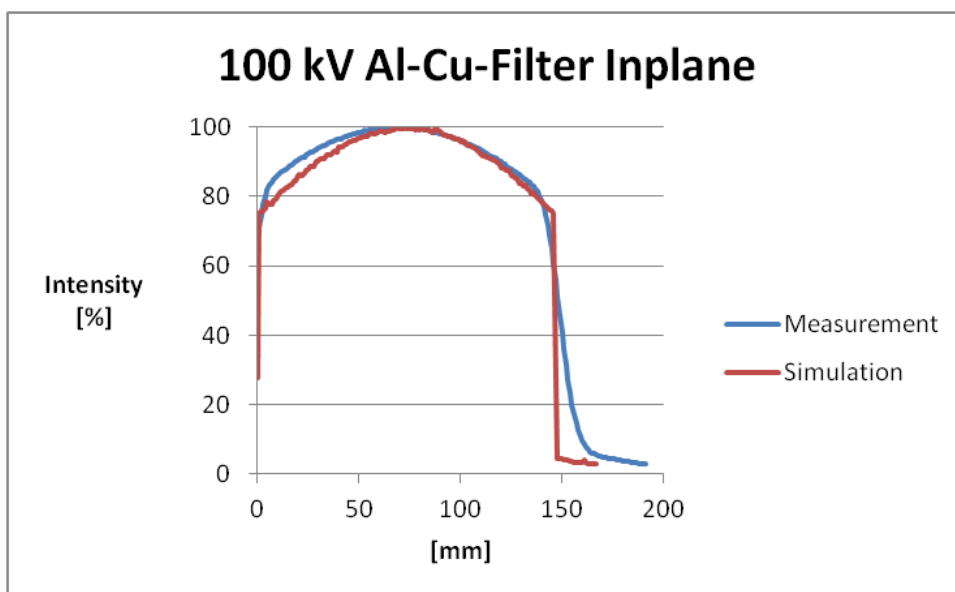


Figure 7.20: Comparison between measured and simulated inplane profile at 100 kV. Applied filtration was 3 mm Al and 0.5 mm Cu.

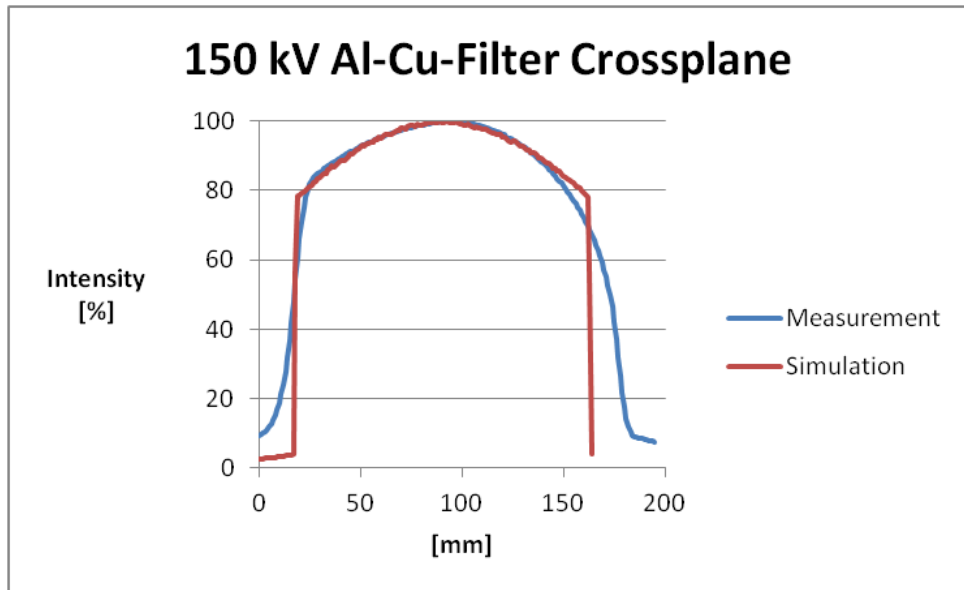


Figure 7.21: Comparison between measured and simulated crossplane profile at 150 kV. Applied filtration was 3 mm Al and 0.5 mm Cu.

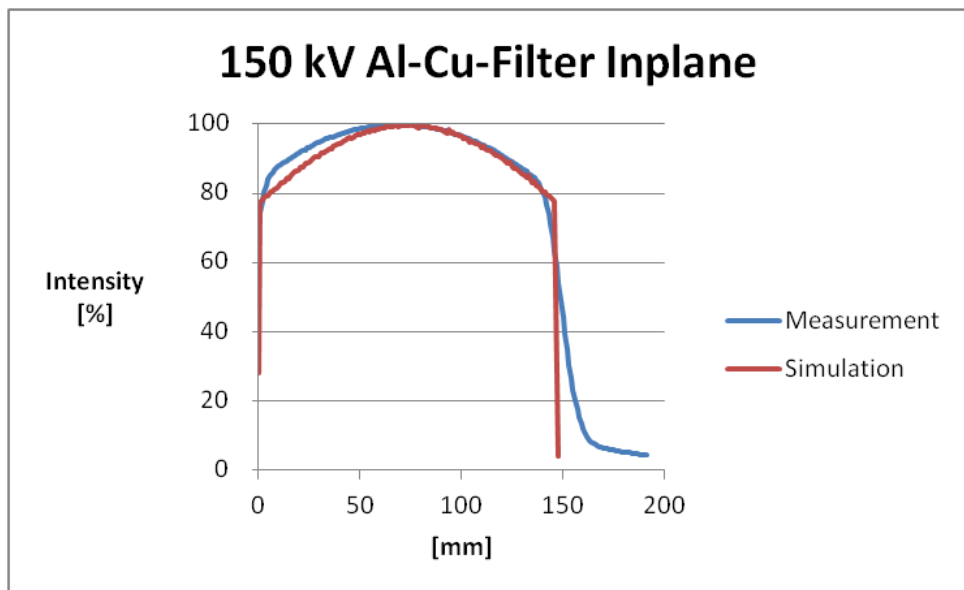


Figure 7.22: Comparison between measured and simulated inplane profile at 150 kV. Applied filtration was 3 mm Al and 0.5 mm Cu.

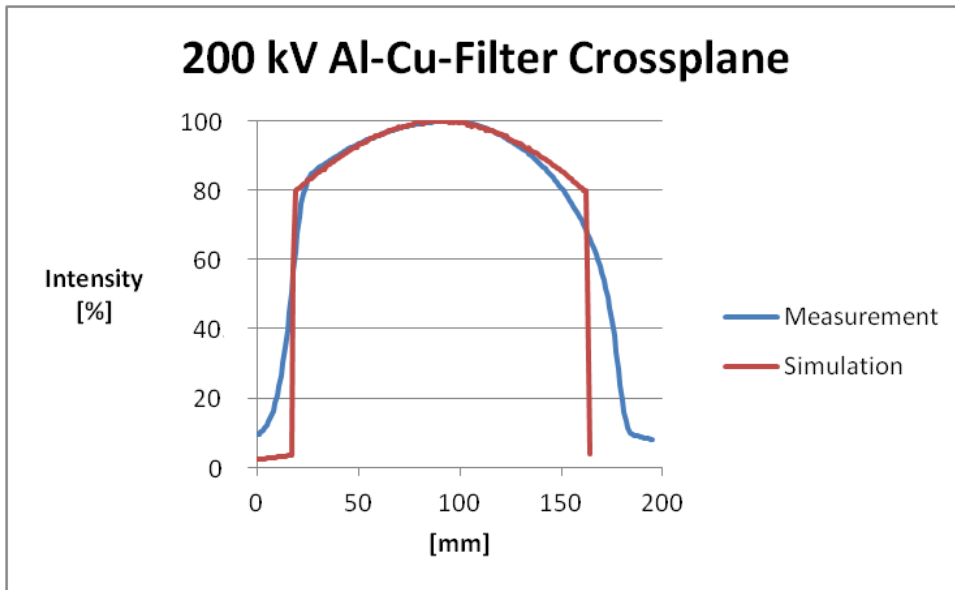


Figure 7.23: Comparison between measured and simulated crossplane profile at 200 kV. Applied filtration was 3 mm Al and 0.5 mm Cu.

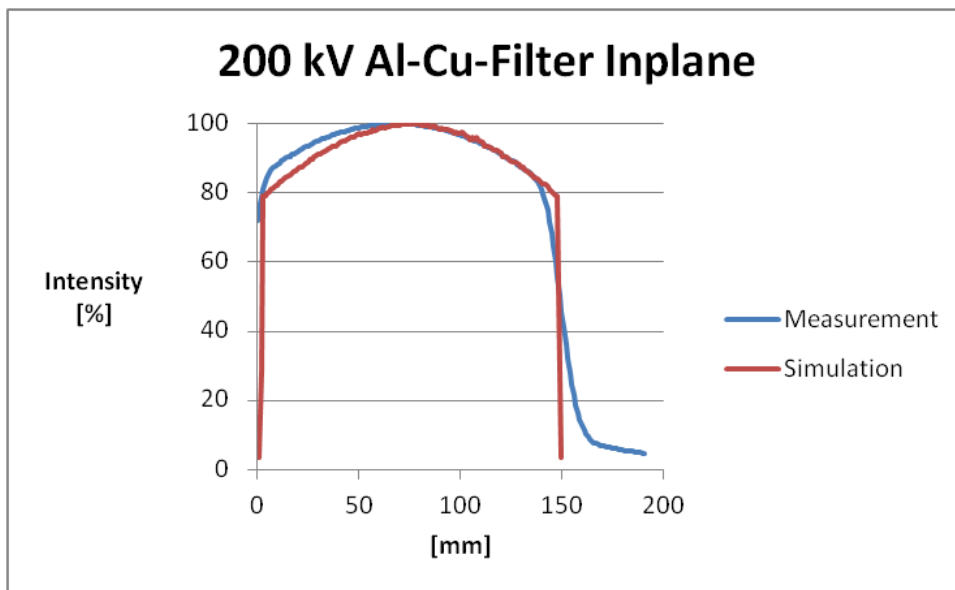


Figure 7.24: Comparison between measured and simulated inplane profile at 200 kV. Applied filtration was 3 mm Al and 0.5 mm Cu.

The steep intensity changes in the simulation data are a result of the used kill actor in GATE. This cylindrical object was placed in the tube exit window to cut off the edges of the rectangular shaped X-ray beam initially produced by the simulation framework. The cylinder diameter was set such that the experimentally determined field size was reproduced as good as possible. Therefore, the deviations listed in tables 7.17 and 7.18 are virtually the same. Note that for 50 kV the setup simulating filtration with Al and Cu in GATE yielded no proper results, due to too low doses stored in the actors.

The setup containing a single Al-filter, with its thickness set accordingly to table 5.2, produced larger deviations as shown in table 7.20. The reason for that are more interactions and scatter effects taking place. It has to be noted that no results for the 50 kV case could be obtained. Also the Al-Cu combination simulated in GATE with the *Air2* material produced a slightly different deviation in inplane direction at 150 kV of -3.5% (see tables 7.19 and 7.21). Since in this setup the filtration was modeled in GATE, scattering in the filtration materials as well as increased interactions with the *Air2* could be responsible for the observed deviations. It is also necessary to consider the fact, that a lot of photons are absorbed in the Al-Cu filter if it is implemented in GATE, yielding less significant statistics for the dose distribution, which also influences the beam size. The above mentioned points lead to the fact, that the software *SpekCalc* lends itself for the simulation of pre-filtered spectra, which can later be used as GATE input.

Deviations of Al-Filter in GATE to Measurements				
Directon	Crossplane		Inplane	
	[mm]	[%]	[mm]	[%]
50	0.5 (0.5)	0.3 (0.3)	-1.0 (-1.0)	-0.7 (-0.7)
100	1.0 (1.0)	0.7 (0.)	-6.0 (-6.0)	-4.1 (-4.1)
150	2.5 (2.5)	1.7 (1.7)	-4.0 (-4.0)	-2.8 (-2.8)
200	3.0 (3.0)	2.1 (2.1)	-4.5 (-4.5)	-3.1 (-3.1)

Table 7.17: Deviations of the beam spot size in cross- and inplane direction at different energies. The applied filtration was 3 mm Al. Simulations were conducted using *Air* and *Air2*, with the results for the latter shown in brackets.

Deviations of GATE with Al-Filter in <i>SpekCalc</i>				
Directon	Crossplane		Inplane	
Energy [kV]	[mm]	[%]	[mm]	[%]
50	0.5 (0.5)	0.3 (0.3)	-1.0 (-1.0)	-0.7 (-0.7)
100	1.0 (1.0)	0.7 (0.7)	-6.0 (-6.0)	-4.1 (-4.1)
150	2.5 (2.5)	1.7 (1.7)	-4.0 (-4.0)	-2.8 (-2.8)
200	3.0 (3.0)	2.1 (2.1)	-4.5 (-4.5)	-3.1 (-3.1)

Table 7.18: Deviations of the beam spot size in cross- and inplane direction at different energies. The applied filtration was 3 mm Al and already included in *SpekCalc*. Simulations were conducted using *Air* and *Air2*, with the results for the latter shown in brackets.

Deviations of Al-Cu-Filter in GATE to Measurements				
Directon	Crossplane		Inplane	
Energy [kV]	[mm]	[%]	[mm]	[%]
100	1.0 (1.0)	0.7 (0.7)	-6.0 (-6.0)	-4.1 (-4.1)
150	2.5 (2.5)	1.7 (1.7)	-4.0 (-5.0)	-2.8 (-3.5)
200	3.0 (3.0)	2.1 (2.1)	-4.5 (-4.5)	-3.1 (-3.1)

Table 7.19: Deviations of the beam spot size in cross- and inplane direction at different energies. The applied filtration was 3 mm Al and 0.5 mm Cu. Simulations were conducted using *Air* and *Air2*, with the results for the latter shown in brackets.

The presented profiles for the crossplane direction show also that the Heel effect plays only a dominant role if the X-ray beam is filtered with Al. In figures 7.9, 7.11, 7.13 and 7.15 an intensity decrease due to the Heel effect can be observed, which is not occurring in the inplane profiles. Application of Cu as additional filtration material removes this effect almost completely from the profiles (see figures 7.17, 7.19, 7.21 and 7.23).

Since the intensity on the bottom side of the beam differs about 20 %, especially at 200 kV with Al-filtering, this could also influence simulations concerning the determination of HVLs or dose distributions. Although some discrepancies

Deviations of a single Al-Filter in GATE to Measurements					
Directon	Crossplane		Inplane		
	Energy [kV]	[mm]	[%]	[mm]	[%]
	100	3.0	2.0	-5.0	-3.4
	150	5.5	3.7	-1.0	-0.7
	200	7.0	4.7	-0.5	-0.3

Table 7.20: Deviations of the beam spot size in cross- and inplane direction at different energies. The Be-Al-Cu filters were replaced by a single Al-filter with its thickness set corresponding to the data shown in table 5.2.

Deviations of GATE with Al-Cu-Filter in <i>SpekCalc</i>					
Directon	Crossplane		Inplane		
	Energy [kV]	[mm]	[%]	[mm]	[%]
	50	0.5 (0.5)	0.3 (0.3)	-1.0 (-1.0)	-0.7 (-0.7)
	100	1.0 (1.0)	0.7 (0.7)	-6.0 (-6.0)	-4.1 (-4.1)
	150	2.5 (2.5)	1.7 (1.7)	-4.0 (-4.0)	-2.8 (-2.8)
	200	3.0 (3.0)	2.1 (2.1)	-4.5 (-4.5)	-3.1 (-3.1)

Table 7.21: Deviations of the beam spot size in cross- and inplane direction at different energies. The applied filtration was 3 mm Al together with 0.5 mm Cu and already included in *SpekCalc*. Simulations were conducted using *Air* and *Air2*, with the results for the latter shown in brackets.

can be observed, the Heel effect is often neglected due to issues concerning the computational time and was hence also omitted in this study. Additionally, due to the normally small size of the irradiated objects, mostly mice and cells, compared to the X-ray beam size, the neglect of the Heel effect has virtually no effect on the resulting dose homogeneity in the simulations, as reported by Noblet et al. [15]. However, in actual biological experiments the use of additional filtration to remove the Heel effect is necessary.

7.3 Spot Size in Lead Collimator Setup

The data collected from the simulations with this setup showed a major difficulty with the Monte Carlo toolkit GATE. Despite the use of $20 \cdot 10^9$ particles, the resolution of the used actor storing the dose, could not be reduced under 0.5 mm. Only a tremendous increase of the simulated number of particles could maybe provide useful data. Therefore, the comparison to existing measurement data, which show deviations in the range of 0.1 mm, was impossible.

Concluding from that, it would be necessary for specific setups to alter the properties of the X-ray beam. Possible properties that could be adjusted are the angular distributions in both, cross- and inplane direction, leading to a more collimated beam. In the case of such a specific setup, with an exit window diameter of 3 mm in the lead collimator, all photons diverging out of the inner beam path could be neglected without influencing the results. Due to the aim of this work, which was on the one hand to model the X-ray tube in the most realistic way possible and on the other to investigate how many particles were needed to obtain proper results, these adjustments have been omitted.

7.4 Dose Distributions in Cell Irradiation Setup

Figure 7.25 shows the different depth dose curves in the cell flask type T75 for air and water obtained by simulations. Additionally, the dose decrease in PMMA (flask holder material) is illustrated. The curves for PMMA and water behave similarly, with the only difference being found in the intensity. Directly after the border the difference between PMMA and water is 11.3 % and decreases at the back of the flask to 7.7 %. For water the intensity difference between the flask's front and back is 47.4 % and for PMMA it is 43.8 %. Additionally, figure 7.25 shows not only that the corresponding dose drop for air between the front and the back of the flask is 15.6 %, but also that the intensity difference between air and the two other materials decreases with depth and is finally even higher than in PMMA.

The simulations also confirmed the assumption of a homogeneous dose distribution with water filling, which are shown in figures 6.12 - 6.14. With air as filling

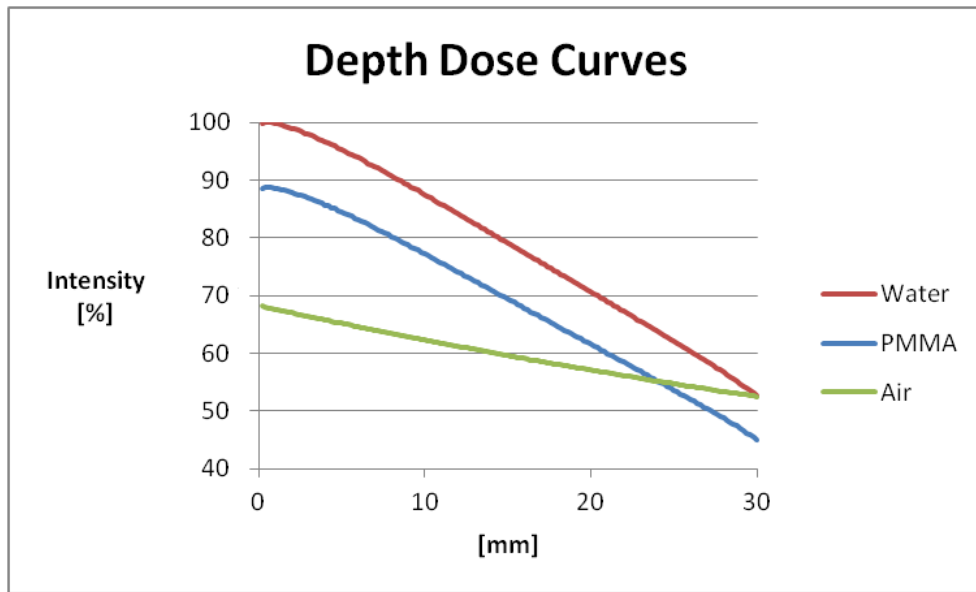


Figure 7.25: Simulated depth dose curves at 200 kV in the cell irradiation setup.

material the resulting dose distributions differ a bit more (see figures 6.7 - 6.9), but can also be assumed as homogeneous.

At the border of the flask with air filling contours of high doses can be observed, as seen in figures 6.10 and 6.11. This clearly demonstrates the different electron ranges in the various materials. This range is higher in air than in PMMA and therefore the particles entering the PMMA box from inside the flask deposit most of their dose at the border. Vice versa the electrons coming from the PMMA border are subsequently in a material where they have a higher range and distribute their dose nearly homogeneously. On the contrary, the described effect does not occur in a water filled flask, where the dose profiles for the cross- and inplane directions (see figures 6.15 and 6.16) show no overshooting at the border, because the electron ranges in PMMA and water are quite similar.

These investigations are of importance for ongoing cell experiments in particle therapy centers. In nearly all proton or heavy ion cell experiments a horizontal beam line is used (e.g. non-clinical irradiation room at MedAustron [24]). Hence, it is necessary to adopt existing cell experiments performed at ^{60}Co units or medical linear accelerators, which includes also the setup for the reference beam (e.g. YXLON Maxishot X-ray tube) [45]. In standard experiments the flask is lying

and only the floor is covered with the liquid, in contrast to the standing flasks used with horizontal beam lines. Here the whole flask must be filled with liquid to gain a homogenous cell distribution and ensure that the cells are attached to the wall. It is also important that the effects observed are not coming from different flask positions but can be correlated to effects from different beams. Therefore, dedicated knowledge of dosimetric behavior is needed with special focus on the border region.

In addition, the crossplane profiles for air and water show an intensity decrease on the upper side of the investigated area. Due to scattering effects in the PMMA mounting platform, the higher doses in the bottom region of the flask holder are observed. The scattering can also be seen in the dose distributions 6.8 - 6.14.

A different kind of problem when simulating this setup is the high amount of particles needed to achieve acceptable results. Though in this study up to $20 \cdot 10^9$ particles were used, it can be seen for example in figure 6.10, that the computed doses remain quite noisy. Improving the quality of the simulation can be done by using either a higher amount of particles or implement voxelized sources for modeling the geometrical setup. The use of these voxelized objects allows the application of a so called *seTLEDoseActor* increasing the resulting dose by a factor 10 – 15 [42]. If the desired resolution of the actor shall be increased simultaneously only higher computational time offers a solution.

8 Conclusion and Outlook

This work proved that simulation of low kV dosimetry is in principle possible using the Monte Carlo based framework GATE. What remains challenging is the correct description and modeling of the X-ray source and its output spectrum. Furthermore, the creation of a realistic beam shape needs some technical tricks and can not be achieved in a desirable and easy way at present. Although for the GATE simulations no proper physics lists were available, which could describe the occurring interactions especially in the low kV energy range as studied in the scope of this thesis, most results obtained were in good accordance with the collected experimental data. This proves that the *emlivermore* physics list includes mathematical models which are sufficient for the higher energy range.

A different issue is the high number of particles (10^9) needed to compute useful results in comparison to 10^6 in typical particle therapy simulations or 10^3 in imaging simulations [20, 46].

It could also be evaluated, that the commercially available software *SpekCalc* provides a suitable solution to compute X-ray spectra generated by a tungsten target. Together with the possibility to add different types of filtrations and providing the user with information concerning the HVLs in Al and Cu, the program proved itself rather useful for generating the GATE input files for the X-ray source. Using the filtration options in *SpekCalc* simplifies on the one hand the simulation setups and on the other hand reduces the computational time needed. However, the inclusion of the Heel effect is not possible and also the use of a fixed minimum energy leaves uncertainties.

Several points of improvement exist where the accuracy of the dosimetric calculations could be increased. At first, an exact model of the X-ray tube included in the YXLON Maxishot could be modeled with the GATE framework. This would lead to the computation of spectra including the Heel effect, which had been ne-

glected in the present work. It is also possible that the resulting spectra reproduce the beam in a better way. Problems arising following this approach are the implemented physics processes themselves. If they do not describe the interactions accurately enough, additional uncertainties are produced. Additionally, the computational time needed would rise tremendously together with the space needed to store the produced data. The available *PhaseSpace* actors need several gigabytes of disk space to store the calculated X-ray spectrum and for each energy such a *PhaseSpace* file would be needed. If one overcomes all these challenges, the interactions and absorptions taking place inside the filter materials still remain an issue, since these effects increase computational time and simultaneously deteriorate the accuracy of the simulations.

Additionally to the challenges concerning the output spectrum, the implemented solution to form the conical shape of the X-ray beam, as done in the present work, comes up with disadvantages. One major problem by using a so called *KillActor* is, again, the loss of particles, yielding unnecessarily wasted computation time on following unwanted particle tracks. A more elegant solution, for example the implementation of a specific source type in the GATE framework, could resolve this issue.

A different approach would be the use of especially designed physics lists or processes for the low kV energy range. At the present time, GEANT4 comes with the possibility to use the so called *DNA* physics list for low energy simulations in the radiobiological field [47]. The implementation of this physics list in the GATE framework has recently been reported [48].

As another point of improvement, a detailed model of the used detectors could lead to better matching simulation results concerning the HVLs, due to a more realistic behavior especially in the low energy range and when using it together with special mountings possibly altering the measurement results. However, the use of accurately implemented physics processes remains a limiting factor.

Eventually, CT images of certain experimental setups could be taken, resulting in a more realistic geometrical setup for the simulations. It also enables the use of voxelized volumes, allowing the application of the provided *seTLEDoseActors* in the GATE simulations, which decrease the computation time by a factor 10 – 15 compared to the *TLEDoseActor* [42].

The implementation of the above mentioned points would lead to a more realistic model of the YXLON Maxishot and the provided X-ray spectrum. Hence, the simulation could provide better matching beam properties and dose distributions, yielding an increased dosimetric accuracy of the model. This would be necessary to use the simulation for reliable dose estimations regarding actual radiobiological experiments with various setups.

Bibliography

- [1] S. Jan, G. Santin, D. Strul, S. Staelens, K. Assié, D. Autret, S. Avner, R. Barbier, M. Bardiés, P.M. Bloomfield, D. Brasse, V. Breton, P. Bruyndonckx, I. Buvat, A.F. Chatziioannou, Y. Choi, Y.H. Chung, C. Comtat, D. Donnarieix, L. Ferrer, S.J. Glick, C.J. Groiselle, D. Guez, P.-F. Honore, S. Kerhoas-Cavata, A.S. Kirov, V. Kohli, M. Koole, M. Krieguer, D.J. van der Laan, F. Lamare, G. LARGERON, C. Lartizien, D. Lazaro, M. C. Maas, L. Maigne, F. Mayet, F. Melot, C. Merheb, E. Pennacchio, J. Perez, U. Pietrzyk, F. R. Rannou, M. Rey, D.R. Schaart, C.R. Schmidtlein, L. Simon, T.Y. Song, J.-M. Vieira, D. Visvikis, R. Van de Walle, E. Wieërs, and C. Morel. „GATE: a simulation toolkit for PET and SPECT“. In: *Physics in Medicine and Biology* 49 (2004), pp. 4543–4561.
- [2] H. Krieger. *Grundlagen der Strahlungsphysik und des Strahlenschutzes*. 3rd ed. Wiesbaden: Vieweg+Teubner, 2009.
- [3] H. Krieger. *Strahlungsmessung und Dosimetrie*. 2nd ed. Wiesbaden: Springer Spektrum, 2013.
- [4] H. Krieger. *Strahlungsquellen für Technik und Medizin*. 2nd ed. Wiesbaden: Springer Spektrum, 2013.
- [5] D.R. Dance, S. Christofides, A.D.A. Maidment, I.D. McLean, and K.H. Ng, eds. *Diagnostic Radiology Physics. A Handbook for Teachers and Students*. Wien: IAEA, 2014.
- [6] W. Demtröder. *Experimentalphysik 4. Kern-, Teilchen- und Astrophysik*. 3rd ed. Berlin Heidelberg: Springer-Verlag, 2010.

- [7] C.-M. Ma, C.W. Coffey, L.A. DeWerd, C. Liu, R. Nath, S.M. Seltzer, and J.P. Seuntjens. „AAPM protocol for 40–300 kV x-ray beam dosimetry in radiotherapy and radiobiology“. In: *The International Journal of Medical Physics Research and Practice* 28 (2001), pp. 868–893.
- [8] R.L. Harrison. „Introduction to Monte Carlo Simulation“. In: *American Institute of Physics Conference Proceedings* 1204 (2010), pp. 17–21.
- [9] D P. Landau and K. Binder. *A Guide to Monte Carlo Simulation in Statistical Physics*. Cambridge, UK: Cambridge University Press, 2003.
- [10] A.F. Bielajew. *Fundamentals of the Monte Carlo method for neutral and charged particle transport*. Ann Arbor, Michigan, U.S.A.: University of Michigan, 2001.
- [11] H. Fuchs. „Development and Validation of Helium Ion Beam Dose Calculation“. PhD thesis. Vienna: Medical University of Vienna, Dec. 2014.
- [12] M. Daniel. *Adaptive Radiotherapie des Verziäkarzinoms. Dosimetrischer Einfluss von Organbewegungen*. Vienna, May 2015.
- [13] D. Sarrut, M. Bardiés, N. Bousson, N. Freud, S. Jan, J.-M. Létang, G. Loudos, L. Maigne, S. Marcatili, T. Mauxion, P. Papadimitroulas, Y. Perrot, U. Pietrzyk, C. Robert, D. R. Schaart, D. Visvikis, and I. Buva. „A review of the use and potential of the GATE Monte Carlo simulation code for radiation therapy and dosimetry applications“. In: *Medical Physics* 41 (2014).
- [14] M. Belley, C. Wang, G. Nguyen, R. Gunasingha, N.J. Chao, B.J. Chen, M.W. Dewhirst, and T.T. Yoshizumi. „Toward an organ based dose prescription method for the improved accuracy of murine dose in orthovoltage x-ray irradiators“. In: *Medical Physics* 41 (2014).
- [15] C. Noblet, S. Chiavassa, F. Paris, A. Lisbona, and G. Delpon. „Underestimation of dose delivery in preclinical irradiation due to scattering conditions“. In: *Physica Medica* 30 (2013), pp. 63–68.
- [16] H. Fuchs, M. Alber, T. Schreiner, and D. Georg. „Implementation of spot scanning dose optimization and dose calculation for helium ions in Hyperion“. In: *Medical Physics* 42 (2015), pp. 5157–5166.

- [17] B. Knäusl, H. Fuchs, K. Dieckmann, and D. Georg. „Can particle beam therapy be improved using helium ions? A planning study focusing on paediatric patients“. In: *Acta Oncologica in Press* (2015).
- [18] B.C. Millar, B.D. Prendergast, A. Alavi, and J.E. Moore. „18FDG-positron emission tomography (PET) has a role to play in the diagnosis and therapy of infective endocarditis and cardiac device infection“. In: *International Journal of Cardiology* 167 (2013), pp. 1724–1736.
- [19] T.T. Böhlen, F. Cerutti, M.P.W. Chin, A. Fassò, A. Ferrari, P.G. Ortega, A. Mairani, P.R. Sala, G. Smirnov, and V. Vlachoudis. „The FLUKA Code: Developments and Challenges for High Energy and Medical Applications“. In: *Nuclear Data Sheets* 120 (2014), pp. 211–214.
- [20] C. Robert, G. Dedes, G. Battistoni, T.T. Böhlen, I. Buvat, F. Cerutti, M.P.W. Chin, A. Ferrari, P. Gueth, C. Kurz, L. Lestand, A. Mairani, G. Montarou, R. Nicolini, P.G. Ortega, K. Parodi, Y. Prezado, P.R. Sala, and E. Testa. „Distributions of secondary particles in proton and carbon-ion therapy: a comparison between GATE/Geant4 and FLUKA Monte Carlo codes“. In: *Physics in Medicine and Biology* 58 (2013), pp. 2879–2899.
- [21] S. Gruber, D. Hamedinger, E. Bozsaky, M. Schmidt, K. Wolfram, J. Haagen, B. Habelt, M. Puttrich, and W. Dörr. „Local hypoxia in oral mucosa (mouse) during daily fractionated irradiation - Effect of pentoxifylline“. In: *Radiotherapy and Oncology* 116 (2015), pp. 404–408.
- [22] S. Gruber, M. Schmidt, E. Bozsaky, K. Wolfram, J. Haagen, B. Habelt, M. Puttrich, and W. Dörr. „Local hypoxia in oral mucosa (mouse) during daily fractionated irradiation - Preclinical studies“. In: *Strahlentherapie und Onkologie* 191 (2015), pp. 242–247.
- [23] W. Dörr and K. R. Trott. „Do we need “biology-based” models to describe cell survival curves after exposure to ionizing radiation?“ In: *Zeitschrift für Medizinische Physik* 25 (2015), pp. 99–101.
- [24] D. Georg and T. Schreiner. *Research Opportunities for Medical Radiation Physics and Radiation Biology. White Book*. Wr. Neustadt, Austria: PEG MedAustron Gesellschaft m.b.H., 2010.

- [25] F. Aumayr, G. Badurek, M. Benedikt, M. Hajek, E. Jericha, P. Kienle, M. Krammer, H. Leeb, J. Marton, E. Widmann, and H. Weber. *Physics Opportunities at MedAustron. White Book*. Wr. Neustadt, Austria: PEG MedAustron Gesellschaft m.b.H.
- [26] *Betriebsanleitung Y.Maxishot*. YXLON International GmbH. Hamburg, 2014.
- [27] L. Lin, C.G. Ainsley, T. Mertens, O. De Wilde, P.T. Talla, and J.E. McDonough. „A novel technique for measuring the low-dose envelope of pencil-beam scanning spot profiles“. In: *Physics in Medicine and Biology* 58 (2013), N171–N180.
- [28] *User Manual Lynx*. Société FIMEL. Fontenay Aux Roses, 2014.
- [29] *Assembly Instructions and User Manual MP3-P Therapy Beam Analyzer L981403*. Physikalisch-Technische Werkstätten. Freiburg, 2014.
- [30] *User Manual Ionization Chambers Type 31010, 31011, 31012, Type 31013 from serial number 1000 (Semi-flexible Chambers)*. Physikalisch-Technische Werkstätten. Freiburg, 2013.
- [31] G. Wieners, M. Pech, A. Beck, B. König, U. Erdmenger, U. Stöckle, P. Wust, R. Felix, and R.-J. Schröder. „Vergleich von Strahlenexposition und Bildqualität eines Siremobil-IsoC3D mit einem 16-Zeilen-Spiral-CT bei Diagnostik und Intervention am humanen Becken“. In: *RöFo - Fortschritte auf dem Gebiet der Röntgenstrahlen und der bildgebenden Verfahren* 177 (2005), pp. 258–264.
- [32] D. Gosch, S. Jendraß, M. Scholz, and T. Kahn. „Strahlenexposition bei der digitalen Vollfeldmammographie mit einem Selen-Flachdetektor“. In: *RöFo - Fortschritte auf dem Gebiet der Röntgenstrahlen und der bildgebenden Verfahren* 178 (2006), pp. 693–697.
- [33] *Gebrauchsanweisung NOMEX Multimeter T1 1049 und NOMEX Software S030008*. Physikalisch-Technische Werkstätten. Freiburg, 2014.
- [34] G. Poludniowski, G. Landry, F. De Blois, P.M. Evans, and F. Verhaegen. „SpekCalc. a program to calculate photon spectra from tungsten anode x-ray tubes“. In: *Physics in Medicine and Biology* 54 (2009), pp. 433–438.

- [35] G. Poludniowski and P.M. Evans. „Calculation of x-ray spectra emerging from an x-ray tube. Part I. Electron penetration characteristics in x-ray targets“. In: *Medical Physics* 34 (2007), pp. 2167–2174.
- [36] G. Poludniowski. „Calculation of x-ray spectra emerging from an x-ray tube. Part II. X-ray production and filtration in x-ray targets“. In: *Medical Physics* 34 (2007), pp. 2175–2186.
- [37] S. Agostinelli et al. „GEANT4 - a simulation toolkit“. In: *Nuclear Instruments and Methods in Physics Research* 506 (2003), pp. 250–303.
- [38] V. Ivanchenko, J. Apostolakis, A. Bagulya, H.B. Abdelouahed, R. Black, A. Bogdanov, H. Burkhard, S. Chauvie, P. Cirrone, G. Cuttone, G. Depaola, F. Di Rosa, S. Elles, Z. Francis, V. Grichine, P. Gumplinger, P. Gueye, S. Incerti, A. Ivanchenko, J. Jacquemier, A. Lechner, F. Longo, O. Kadri, N. Karakatsanis, M. Karamitros, R. Kokoulin, H. Kurashige, M. Maire, A. Mantero, B. Mascialino, J. Moscicki, L. Pandola, J. Perl, I. Petrovic, A. Ristic-Fira, F. Romano, G. Russo, G. Santin, A. Schaelicke, T. Toshito, H. Tran, L. Urban, T. Yamashita, and C. Zacharatou. „Recent Improvements in Geant4 Electromagnetic Physics Models and Interfaces“. In: *Progress in Nuclear Science and Technology* 2 (2011), pp. 989–903.
- [39] V.N. Ivanchenko, S. Incerti, Z. Francis, H.N. Tran, M. Karamitros, M.A. Bernal, C. Champion, and P. Guèye. „Combination of electromagnetic physics processes for microdosimetry in liquid water with the Geant4 Monte Carlo simulation toolkit“. In: *Nuclear Instruments and Methods in Physics Research B* 273 (2012), pp. 95–97.
- [40] R. Brun and F. Rademakers. „ROOT - An Object Oriented Data Analysis Framework“. In: *Nuclear Instruments and Methods in Physics Research Section A: Accelerators, Spectrometers, Detectors and Associated Equipment* 389 (1997), pp. 81–86.
- [41] *User Manual TRUFIX Precision Attachment System*. PTW Freiburg. Freiburg, 2013.

- [42] F. Smekens, J. M. Lètang, C. Noblet, S. Chiavassa, G. Delpon, N. Freud, S. Rit, and D. Sarrut. „Split exponential track length estimator for Monte-Carlo simulations of small-animal radiation“. In: *Physics in Medicine and Biology* 59 (2014), pp. 7703–7715.
- [43] S.C. Chen, W. Loong Jon, and A.Z. Harun. „Evaluation of X-Ray Beam Quality Based on Measurements and Estimations Using SpekCalc and Ipem78 Models“. In: *Malaysian Journal of Medical Physics* 19 (2012), pp. 22–28.
- [44] P. Kuess, E. Bozsaky, J. Hopfgartner, G. Seifritz, W. Dörr, and D. Georg. „Dosimetric challenges of small animal irradiation with a commercial X-ray unit“. In: *Zeitschrift für Medizinische Physik* 24 (2014), pp. 363–372.
- [45] A.J. Cole, C.K. McCarry, K.T. Butterworth, K.M. Prise, J.M. O’Sullivan, and A.R. Hounsell. „Development of a novel experimental model to investigate radiobiological implications of respiratory motion in advanced radiotherapy“. In: *Physics in Medicine and Biology* 57 (2012), pp. 411–420.
- [46] M. Čato. *Modeling of the Siemens Biograph 64 TruePoint Positron Emission Tomography*. Vienna, 2015.
- [47] S. Incerti, A. Ivanchenko, M. Karamitros, A. Mantero, P. Moretto, H.N. Tran, B. Mascialino, C. Champion, V.N. Ivanchenko, M.A. Bernal, Z. Francis, C. Villagrasa, G. Baldacchino, P. Guèye, R. Capra, P. Nieminen, and C. Zacharatou. „Comparison of Geant4 very low energy cross section models with experimental data in water“. In: *Medical Physics* 37 (2010), pp. 4692–4708.
- [48] L. Maigne, A. Anne, M. Bony, E. Delage, D. Donnarieix, A. Dufaure, M. Gautier, S.B. Lee, P. Micheau, G. Montarou, Y. Perrot, J.I. Shin, and S. Incerti. „Coupling of Geant4-DNA physics models into the GATE Monte Carlo platform: Evaluation of radiation-induced damage for clinical and preclinical radiation therapy beams“. In: *Nuclear Instruments and Methods in Physics Research B* 353 (2015), pp. 46–55.

List of Figures

2.1	Coherent scattering on bounded electron (from [2], p185).	6
2.2	Photoelectric effect (from [2], p160).	7
2.3	Energy dependance of the mass-photoabsorption coefficient τ/ρ for lead with the absorption edges L_1 - L_3 and K (from [2], p162).	8
2.4	Compton effect (from [2], p165).	9
2.5	Left: Pair production in atomic Coulomb field. Right: Triplet production in electronic Coulomb field (from [2], p182).	11
2.6	Photonuclear interaction: A photon excites the nucleus resulting in emission of a nucleon (from [2], p186).	12
2.7	X-ray tube: electrons are emitted from the cathode K and interact in the anode A (from [4], p89).	13
2.8	Left: Rectangular distribution from electrons with kinetic energy E_g . Right: Characteristic of N_γ (from [4], p94).	17
2.9	Left: Concept of varying slice thickness. Right: Typical triangular spectrum (from [4], p96).	18
2.10	Left: Unfiltered molybdenum spectrum (from [4], p105).	19
2.11	a) Photons from the anode side (a2) undergo more ineractions inside the anode than the ones from the cathode side (a1). b) Intensity drop on the anode side resulting from the increased absorption. This is called Heel effect (from [5], p97).	19
2.12	Linear mass attenuation coefficient for molybdenum (from [4], p107).	20
2.13	Cut off resulting from the K-edge of molybdenum (from [4], p107).	20
2.14	Mass attenuation coefficient of Al (from [4], p109).	21
2.15	Principle of an ionization chamber (from [3], p28).	23
3.1	YXLON Maxishot at MedAustron	28

3.2	The LYNX device	29
3.3	Perspex tank and orientation of the axes	30
3.4	The semi-flexible chamber type 31010	31
3.5	The NOMEX Multimeter system (from [33], p1).	32
3.6	<i>SpekCalc</i> graphical user interface showing all input parameters . . .	33
3.7	Layered architecture of GATE (from [1], p4).	34
4.1	Definition of cross- and inplane and measurement ranges in beam's eye view.	38
4.2	Al box filled with PMMA plates	39
4.3	Architecture of the GATE simulation	42
4.4	GATE model of the Al box (blue) containing the PMMA box (green cube), with the actor (yellow) placed inside.	45
4.5	GATE model of the Perspex tank (white), with the actor <i>phantom- PDD</i> (yellow) and the actor <i>phantomCrossAndInplane</i> (green). . . .	46
4.6	GATE model of the cell irradiation setup. The flask (blue) is in- serted into the holder (white).	48
4.7	GATE model of the Perspex tank (white) with the lead collimator (grey). The PMMA plate (yellow square) was placed between the collimator and the actor (green square).	49
5.1	Measured profiles inside the Perspex tank at 50 kV with different filtrations.	54
5.2	Measured profiles inside the Perspex tank at 100 kV with different filtrations.	54
5.3	Measured profiles inside the Perspex tank at 150 kV with different filtrations.	55
5.4	Measured profiles inside the Perspex tank at 200 kV with different filtrations.	55
5.5	Beam isodoses at 200 kV for an unfiltered and a Al-Cu-filtered beam. 56	
5.6	Cross- and Inplane profiles with no additional filtration determined using the LYNX system. Saturation of the CCD causes the cut off in the high dose region. On the left side of the crossplane profile the intensity decrease caused by the Heel effect can be observed. . .	57

5.7	Cross- and Inplane profiles with 3 mm Al and 0.5 mm Cu filtration determined using the LYNX system. Saturation of the CCD causes the cut off in the high dose region.	57
6.1	Spectra at 50 kV with different filtrations.	60
6.2	Spectra at 100 kV with different filtrations.	61
6.3	Spectra at 150 kV with different filtrations.	62
6.4	Spectra at 200 kV with different filtrations.	63
6.5	Simulation results for cross- and inplane profiles at 200 kV with additional 3 mm Al filtering.	68
6.6	Example of the X-ray spot simulated with Al-Cu-filtration in <i>SpekCalc</i> at 200 kV tube voltage behind 1 mm PMMA.	74
6.7	Dose distribution in the PMMA border of the flask simulated with air filling at 200 kV. Filtration was 3 mm Al and 0.5 mm Cu. The black lines indicate the positions of the cross- and inplane profiles shown in figures 6.10 and 6.11, and the grey contours outline the actual position of the flask.	76
6.8	Dose distribution in air directly after the PMMA border of the flask simulated at 200 kV tube voltage. The applied filtration was 3 mm Al and 0.5 mm Cu. The black lines indicate the positions of the cross- and inplane profiles shown in figures 6.10 and 6.11.	77
6.9	Dose distribution in 25 mm air inside the flask simulated at 200 kV tube voltage. The applied filtration was 3 mm Al and 0.5 mm Cu. The black lines indicate the positions of the cross- and inplane profiles shown in figures 6.10 and 6.11.	77
6.10	Crossplane dose profiles in the PMMA border, in air directly after the border and at 25 mm depth.	78
6.11	Inplane dose profiles in the PMMA border, in air directly after the border and at 25 mm depth.	78

6.12	Dose distribution in the PMMA border of the flask simulated with water filling at 200 kV. Filtration was 3 mm Al and 0.5 mm Cu. The black lines indicate the positions of the cross- and inplane profiles shown in figures 6.15 and 6.16, and the grey contours outline the actual position of the flask.	79
6.13	Dose distribution in water directly after the PMMA border of the flask simulated at 200 kV tube voltage. The applied filtration was 3 mm Al and 0.5 mm Cu. The black lines indicate the positions of the cross- and inplane profiles shown in figures 6.15 and 6.16.	79
6.14	Dose distribution in 25 mm water inside the flask simulated at 200 kV tube voltage. The applied filtration was 3 mm Al and 0.5 mm Cu. The black lines indicate the positions of the cross- and inplane profiles shown in figures 6.15 and 6.16.	80
6.15	Crossplane dose profiles in the PMMA border, in water directly after the border and at 25 mm depth.	80
6.16	Inplane dose profiles in the PMMA border, in water directly after the border and at 25 mm depth.	81
7.1	HVLs in Al at four energies with Al beam filtration. Two different filter thicknesses have been simulated in GATE. One simulation was done where the 3 mm Al filter was applied in <i>SpekCalc</i>	84
7.2	HVLs in Al at four energies with Al-Cu beam filtration. Several different filter thicknesses have been simulated in GATE. One simulation was done where the 3 mm Al and 0.5 mm Cu filtration was applied in <i>SpekCalc</i>	87
7.3	50 % intensity drops for different energies measured inside the Perspex tank compared to simulation data. The applied filtration was 3 mm Al. Simulations were done with realistic filter thicknesses in GATE and <i>SpekCalc</i> and two different material models of air were investigated.	91

7.4	75 % intensity drops for different energies measured inside the Perspex tank compared to simulation data. The applied filtration was 3 mm Al. Simulations were done with realistic filter thicknesses in GATE and <i>SpekCalc</i> and two different material models of air were investigated.	92
7.5	50 % intensity drops for different energies measured inside the Perspex tank compared to simulation data. The applied filtration was 3 mm Al and 0.5 mm Cu. Simulations were done with realistic filter thicknesses in GATE and <i>SpekCalc</i> . Also two different material models of air were used.	94
7.6	75 % intensity drops for different energies measured inside the Perspex tank compared to simulation data. The applied filtration was 3 mm Al and 0.5 mm Cu. Simulations were done with realistic filter thicknesses in GATE and <i>SpekCalc</i> . Also two different material models of air were used.	95
7.7	Measured HVLs in PMMA for different energies compared to simulation data. The applied filtration was 3 mm Al. Simulations were done with realistic filter thicknesses modeled in GATE and with the filtration already included <i>SpekCalc</i>	97
7.8	Measured HVLs in PMMA for different energies compared to simulation data. The applied filtration was 3 mm Al and 0.5 mm Cu. Simulations were done with realistic filter thicknesses modeled in GATE and with the filtration already included in <i>SpekCalc</i>	99
7.9	Comparison between measured and simulated crossplane profile at 50 kV. Applied filtration was 3 mm Al.	102
7.10	Comparison between measured and simulated inplane profile at 50 kV. Applied filtration was 3 mm Al.	102
7.11	Comparison between measured and simulated crossplane profile at 100 kV. Applied filtration was 3 mm Al.	103
7.12	Comparison between measured and simulated inplane profile at 100 kV. Applied filtration was 3 mm Al.	103
7.13	Comparison between measured and simulated crossplane profile at 150 kV. Applied filtration was 3 mm Al.	104

7.14	Comparison between measured and simulated inplane profile at 150 kV. Applied filtration was 3 mm Al.	104
7.15	Comparison between measured and simulated crossplane profile at 200 kV. Applied filtration was 3 mm Al.	105
7.16	Comparison between measured and simulated inplane profile at 200 kV. Applied filtration was 3 mm Al.	105
7.17	Comparison between measured and simulated crossplane profile at 50 kV. Applied filtration was 3 mm Al and 0.5 mm Cu.	106
7.18	Comparison between measured and simulated inplane profile at 50 kV. Applied filtration was 3 mm Al and 0.5 mm Cu. Scattering effects are the reason for the measured dose increase after around 150 mm.	106
7.19	Comparison between measured and simulated crossplane profile at 100 kV. Applied filtration was 3 mm Al and 0.5 mm Cu.	107
7.20	Comparison between measured and simulated inplane profile at 100 kV. Applied filtration was 3 mm Al and 0.5 mm Cu.	107
7.21	Comparison between measured and simulated crossplane profile at 150 kV. Applied filtration was 3 mm Al and 0.5 mm Cu.	108
7.22	Comparison between measured and simulated inplane profile at 150 kV. Applied filtration was 3 mm Al and 0.5 mm Cu.	108
7.23	Comparison between measured and simulated crossplane profile at 200 kV. Applied filtration was 3 mm Al and 0.5 mm Cu.	109
7.24	Comparison between measured and simulated inplane profile at 200 kV. Applied filtration was 3 mm Al and 0.5 mm Cu.	109
7.25	Simulated depth dose curves at 200 kV in the cell irradiation setup.	114

List of Tables

4.1	Initial parameters to generate the input X-ray spectrum using <i>SpekCalc</i>	41
4.2	Limits for the angular distribution of the X-ray source	43
4.3	Energies and filter thicknesses used to simulate <i>alu_block.mac</i> with an applied Al-filter of varying thickness.	44
4.4	Energies and filter thicknesses used to simulate <i>alu_block.mac</i> with an applied Al-Cu-filter of varying thickness.	44
5.1	HVLs and HFs measured inside the Perspex tank.	51
5.2	HVLs and total filtration in mm Al measured with the NOMEX Multimeter system at different energies and filter combinations. Deviations for the HVLs are ± 0.25 mm and for the total Filtration in mm Al ± 0.5 mm.	52
5.3	Results from the crossplane dosimetric measurements.	53
5.4	Results from the inplane dosimetric measurements.	53
5.5	1. and 2. HVLs and HFs in PMMA for different beam energies and filter combinations. Values with a * are interpolated using equation 2.11, since they were not measurable for the Al-Cu filter combination.	58
6.1	HVLs and HFs calculated with <i>SpekCalc</i> . Filtration parameters were 3 mm Be and 3 mm Al and additional 0.5 mm Cu for Al-Cu-filtering.	59
6.2	GATE simulations of HVLs in Al with with different filter thicknesses at four energies. The applied physics lists were <i>emlivermore</i> and <i>QGSP_BERT_EMZ</i> . Results for the latter are shown in brackets.	64
6.3	GATE simulations of HVLs at four energies with different Al-Cu-filter thicknesses. The applied physics lists were <i>emlivermore</i> and <i>QGSP_BERT_EMZ</i> . Results for the latter are shown in brackets. .	65

6.4	Single Al-Filter at different energies and filtrations using two different physics lists, <i>emlivermore</i> and <i>QGSP_BERT_EMZ</i> . Results for the latter are shown in brackets. The Al-filter thickness was set according to table 5.2.	66
6.5	HVLs simulated in GATE with Al- and Al-Cu-filtration done in <i>SpekCalc</i> . The filter thicknesses set were 3 mm Be, 3 mm Al and 0.5 mm Cu. As physics list <i>emlivermore</i> and <i>QGSP_BERT_EMZ</i> were used, with the results of the latter shown in brackets.	67
6.6	HVLs and HFs simulated for Al-filtration with two different air models. The results for <i>Air2</i> are given in brackets.	68
6.7	Cross- and inplane distances at different energies using Al-filtration simulated with GATE. Two different materials, <i>Air</i> and <i>Air2</i> , were used to model the air. Results for the latter are shown in brackets.	68
6.8	HVLs and HFs simulated for Al-Cu-filtration in GATE with two different air models, <i>Air</i> and <i>Air2</i> . Results for <i>Air2</i> are shown in brackets.	69
6.9	Cross- and inplane distances at different energies using Al-Cu-filtration simulated with GATE. Two different materials, <i>Air</i> and <i>Air2</i> , were used to model the air. Results for the latter are shown in brackets.	69
6.10	HVLs and HFs calculated for a single Al-filter in GATE replacing Be-Al-Cu. The thickness of the Al-filter was set accordingly to table 5.2. As material <i>Air</i> was used.	70
6.11	Cross- and inplane distances at different energies using a single Al-filter in GATE replacing the Be-Al-Cu combination simulated with GATE. Its thickness was set accordingly to the results from table 5.2. Here only the GATE material <i>Air</i> was used to model the air.	70
6.12	HVLs and HFs calculated for Al-filtration using <i>Air</i> and <i>Air2</i> as materials. Results for the latter are shown in brackets.	71
6.13	HVLs and HFs calculated for Al-Cu-filtration applied in <i>SpekCalc</i> using <i>Air</i> and <i>Air2</i> as materials. Results for the latter are shown in brackets.	71

6.14	Cross- and inplane distances for Al- and Al-Cu-filtration in <i>SpekCalc</i> using <i>Air</i> and <i>Air2</i> as materials. Results for the latter are given in brackets.	72
6.15	Simulated HVLs and HF's for Al- and Al-Cu-filtration modeled in GATE.	73
6.16	Simulated HVLs and HF's for Al- and Al-Cu-filtration modeled in <i>SpekCalc</i> . The prefiltered spectra were used as input for GATE. . .	73
6.17	Simulated HVLs and HF's for a single Al-filter modeled in GATE. Its thickness was set accordingly to table 5.2.	73
6.18	FWHM values at different energies and PMMA thicknesses. The filtration thicknesses in GATE and in <i>SpekCalc</i> were set to 3 mm Al and 0.5 mm Cu, whereas for the single Al-Filter it was set accordingly to table 5.2.	75
7.1	Deviations of HVLs in Al computed for different filtrations with <i>SpekCalc</i>	85
7.2	Deviations of HVLs in Al for simulations with GATE using the prefiltered spectra provided by <i>SpekCalc</i> . The filtration material was 3 mm Be and 3 mm Al.	85
7.3	Deviations of HVLs in Al for simulations with GATE using different Al-filter thicknesses. The applied physics list were <i>emlivermore</i> and <i>QGSP_BERT_EMZ</i> . Results for the latter are shown using brackets. 86	86
7.4	Deviations of HVLs in Al for simulations with GATE using two physics lists, <i>emlivermore</i> and <i>QGSP_BERT_EMZ</i> , with the results for the latter being shown in brackets. The filtration of 3 mm Be, 3 mm Al and 0.5 mm Cu was already included in <i>SpekCalc</i> . . .	88
7.5	Deviations of HVLs in Al. As filtration a single Al-filter was applied in GATE with its thickness corresponding to table 5.2. Two physics lists were used, <i>emlivermore</i> and <i>QGSP_BERT_EMZ</i> . Results for the latter are shown in brackets.	89
7.6	Deviations of HVLs in AL with <i>emlivermore</i> and <i>QGSP_BERT_EMZ</i> physics list at different Al-Cu-filter thicknesses. Results for the <i>QGSP_BERT_EMZ</i> physics list are shown in brackets.	90

7.7	Intensity drop deviations for Al filtration at different energies as computed with GATE for <i>Air</i> and <i>Air2</i> . Results for <i>Air2</i> are shown in brackets. The filter thickness was 3 mm Al.	93
7.8	Computed deviations of the intensity drops at different energies with <i>Air</i> and <i>Air2</i> . Results for <i>Air2</i> are shown using brackets. The 3 mm Al filter was included in <i>SpekCalc</i>	93
7.9	Intensity drop deviations for Al-Cu-filtration at different energies as computed with GATE. The filter thicknesses were 3 mm Al and 0.5 mm Cu. Simulations were conducted with <i>Air</i> and <i>Air2</i> , with the results for the latter shown in brackets.	94
7.10	Computed deviations of the intensity drops at different energies. The 3 mm Al filter and 0.5 mm Cu were included in <i>SpekCalc</i> . Simulations were conducted using <i>Air</i> and <i>Air2</i> , with the results for the latter shown in brackets.	95
7.11	Deviations of intensity drops in air at different energies. As filtration a single Al-filter was applied in GATE with its thickness corresponding to table 5.2.	96
7.12	Deviations for the HVLs in PMMA at different energies. The 3 mm Al filtration was modeled in the GATE simulations.	98
7.13	Deviations for the HVLs in PMMA at different energies. The 3 mm Al filtration was included in <i>SpekCalc</i> and the simulations performed with the pre-filtered spectra.	98
7.14	Deviations for the HVLs in PMMA at different energies. The 3 mm Al and 0.5 mm Cu filtration were modeled in the GATE simulations.	100
7.15	Deviations for the HVLs in PMMA at different energies. The 3 mm Al and 0.5 filtration were included in <i>SpekCalc</i> and the simulations performed with the pre-filtered spectra.	100
7.16	Deviations for the HVLs in PMMA at different energies. The filtration was done with a single Al filter replacing the Be-Al-C combination. Its thickness was set following the values from table 5.2.	101

7.17	Deviations of the beam spot size in cross- and inplane direction at different energies. The applied filtration was 3 mm Al. Simulations were conducted using <i>Air</i> and <i>Air2</i> , with the results for the latter shown in brackets.	110
7.18	Deviations of the beam spot size in cross- and inplane direction at different energies. The applied filtration was 3 mm Al and already included in <i>SpekCalc</i> . Simulations were conducted using <i>Air</i> and <i>Air2</i> , with the results for the latter shown in brackets.	111
7.19	Deviations of the beam spot size in cross- and inplane direction at different energies. The applied filtration was 3 mm Al and 0.5 mm Cu. Simulations were conducted using <i>Air</i> and <i>Air2</i> , with the results for the latter shown in brackets.	111
7.20	Deviations of the beam spot size in cross- and inplane direction at different energies. The Be-Al-Cu filters were replaced by a single Al-filter with its thickness set corresponding to the data shown in table 5.2.	112
7.21	Deviations of the beam spot size in cross- and inplane direction at different energies. The applied filtration was 3 mm Al together with 0.5 mm Cu and already included in <i>SpekCalc</i> . Simulations were conducted using <i>Air</i> and <i>Air2</i> , with the results for the latter shown in brackets.	112